

AD-A176 412

2

AFGL-TR-85-0107(I)

DEVELOPMENT OF TECHNIQUES FOR THE USE OF DMSP SSIE DATA
IN THE AWS 4D IONOSPHERE MODEL

James A. Secan
Physical Dynamics, Inc.
Northwest Office
P.O. Box 3027
Bellevue, WA 98009

20 April 1985

Final Report
1 July 1984 - 20 April 1985

DTIC
S
FEB 5 1987
A

Approved for public release; distribution unlimited

Prepared for:

AIR FORCE GEOPHYSICS LABORATORY
AIR FORCE SYSTEMS COMMAND
UNITED STATES AIR FORCE
HANSCOM AFB, MASSACHUSETTS 01731

MMTC FILE COPY

87 2 5 085

UNCLASSIFIED

SECURITY CLASSIFICATION OF THIS PAGE

ADA176412

REPORT DOCUMENTATION PAGE				Form Approved OMB No 0704 0188 Exp Date Jun 30 1986	
1a REPORT SECURITY CLASSIFICATION UNCLASSIFIED			1b RESTRICTIVE MARKINGS		
2a SECURITY CLASSIFICATION AUTHORITY			3 DISTRIBUTION/AVAILABILITY OF REPORT		
2b DECLASSIFICATION/DOWNGRADING SCHEDULE			Approved for public release; distribution unlimited		
4 PERFORMING ORGANIZATION REPORT NUMBER(S) PD-NW-85-327R			5 MONITORING ORGANIZATION REPORT NUMBER(S) AFGL-TR-85-0107(1)		
6a NAME OF PERFORMING ORGANIZATION Physical Dynamics, Inc. Northwest Division		6b OFFICE SYMBOL (if applicable)	7a NAME OF MONITORING ORGANIZATION Air Force Geophysics Laboratory		
6c ADDRESS (City, State, and ZIP Code) P.O. Box 3027 Bellevue, WA 98009			7b ADDRESS (City, State, and ZIP Code) Hanscom AFB, MA 01731		
8a NAME OF FUNDING/SPONSORING ORGANIZATION		8b OFFICE SYMBOL (if applicable)	9 PROCUREMENT INSTRUMENT IDENTIFICATION NUMBER F19628-83-C-0106		
8c ADDRESS (City, State, and ZIP Code)			10 SOURCE OF FUNDING NUMBERS		
			PROGRAM ELEMENT NO 61102F	PROJECT NO 2311	TASK NO G2
			WORK UNIT ACCESSION NO FF		
11 TITLE (Include Security Classification) DEVELOPMENT OF TECHNIQUES FOR THE USE OF DMSP (over)					
12 PERSONAL AUTHOR(S) Secan, James A.					
13a TYPE OF REPORT Final Report		13b TIME COVERED FROM 84JUL01 TO 85APR20	14 DATE OF REPORT (Year, Month, Day) 85APR20		15 PAGE COUNT 98
16 SUPPLEMENTARY NOTATION					
17 COSATI CODES			18 SUBJECT TERMS (Continue on reverse if necessary and identify by block number)		
FIELD	GROUP	SUB-GROUP	Ionosphere, Ionospheric modeling, Ionospheric analysis, Topside ionosphere, Total Electron Content (TEC), Defense Meteorology Satellite Program (DMSP)		
19 ABSTRACT (Continue on reverse if necessary and identify by block number) Techniques for improved use of topside ionosphere observations within the Air Weather Service (AWS) 4D ionosphere model system are investigated. Topside observations are available at the Air Force Global Weather Central (AFGWC) from the Topside Ionospheric Plasma Monitor (SSIE) on the Block 5D DMSP satellites. The investigations cover three study areas: 1) improvements to the topside ionospheric electron density profile model used within the 4D model, 2) improvements to the ionospheric data preprocessors in the 4D model system, and 3) improvements to the 4D model. Results are presented for tasks completed during the second year of the project. A parametrization of the topside electron density profile was developed based on a two-component diffusive equilibrium representation of the ionosphere. This topside model can use the entire data set from the SSIE sensor to specify the profile or, if some data are unavailable, it will use an empirical model of the height of the O ₃ to H _o transition height to construct the profile. A method was developed for generating grids of the 800km electron density from observations along an orbit track, and a computer program was					
20 DISTRIBUTION/AVAILABILITY OF ABSTRACT <input type="checkbox"/> UNCLASSIFIED/UNLIMITED <input checked="" type="checkbox"/> SAME AS RPT <input type="checkbox"/> DTIC USERS			21 ABSTRACT SECURITY CLASSIFICATION UNCLASSIFIED		
22a. NAME OF RESPONSIBLE INDIVIDUAL Susan Bredesen			22b TELEPHONE (Include Area Code) (617) 377-2431		22c OFFICE SYMBOL AFGL/PHG

DD FORM 1473, 84 MAR

83 APR edition may be used until exhausted
All other editions are obsolete

SECURITY CLASSIFICATION OF THIS PAGE

UNCLASSIFIED

11. (continued) SSIE DATA IN THE AWS 4D IONOSPHERE MODEL

19. (continued)

written to test the method. This program was also used to investigate joint analyses of $N_e(840)$ and TEC observations.

1990
1991
1992
1993
1994
1995
1996
1997
1998
1999
2000

26W 1993

PREFACE

This report describes the work completed during the second year of a two-year study of ways to enhance the use of data from the USAF Defense Meteorology Satellite Program Topside Ionospheric Plasma Monitor (SSIE) at the Air Force Global Weather Central (AFGWC). This project is a continuation of work completed under contract to Boston College (Boston College Subcontract No. 930-1 to Air Force Geophysics Laboratory Contract F19628-82-K-0011)¹. I wish to acknowledge the assistance of Dr. Fred Rich, AFGL/PHG; Ms. Susan Bredesen, AFGL/PHG; and Mr. Bob Bussey, AFGWC/SDDE, during this project year.

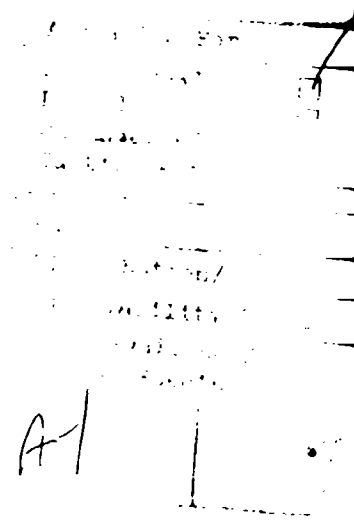


TABLE OF CONTENTS		<u>Page</u>
1.	INTRODUCTION	1
2.	PROJECT DEFINITION	3
3.	TOPSIDE PROFILE MODEL STUDY	5
3.1	Task 2: IRI79 Topside Parametrization	5
3.2	Task 6: Alternative Topside Parametrizations	5
3.2.1	Profile Model	6
3.2.1.1	Model Development and Definition	6
3.2.1.2	Fitting Profiles to Data	11
3.2.1.3	Model Limitations	20
3.2.2	Transition Height Model	30
4.	IONOSPHERIC DATA PREPROCESSORS STUDY	37
4.1	Task 4: Ne(840) Data Preprocessor Improvements	38
4.1.1	Spectral Ne(840) Model	40
4.1.2	Effective F10 Analysis	41
4.1.3	Global Analysis	44
4.1.4	Preprocessor Program (GRIDNE) Description	45
4.1.5	Preprocessor Program Tests	49
4.1.5.1	Description of Test Data and Procedures	49
4.1.5.2	Test Results	54
4.1.6	Limitations	72
4.2	Task 5: Combined TEC and Ne(840) Preprocessor	73
5.	4D MODEL IMPROVEMENTS STUDY	80
5.1	Task 1: 4D Model Global Analysis	80
5.2	Task 3: Model-based 4D Height Functions	80
6.	PROJECT SUMMARY	81
	REFERENCES	83
	APPENDIX A. Topside EDP Parametrizations	86

LIST OF FIGURES

<u>Figure</u>	<u>Caption</u>	<u>Page</u>
1.	SSIE data processing flow at AFGWC.	2
2.	Variation of TEC and $N_e(840)$ with various profile model parameters.	15
3.	Results of fitting profiles to TEC and $N_e(840)$.	19
4.	The two data sets used in the TEC fit tests.	21
5.	Variation of parameters used to adjust the profile model to fit observed TEC for the 02-06 September data set.	22
6.	Same as Figure 5 for the 15-19 August data set.	24
7.	Electron density profiles before (solid curve) and after (dashed curves) adjusting the profile to fit TEC for the 1530LT data from the 02-06 September data set.	26
8.	Same as Figure 7 for the 2030LT data from the 02-06 September data set.	27
9.	Variation of TEC and $N_e(840)$ as functions of the O^+/H^+ transition height for four values of y_t .	29
10.	Seasonal variation in the h_T model for $F_{10.7}=100$, $K_p=3$.	35
11.	$F_{10.7}$ variation in the h_T model for June solstice, $K_p=3$.	36
12.	K_p variation in the h_T model for June solstice, $F_{10.7}=100$.	36
13.	Northern geographic hemisphere fields of $N_e(840)$ from the DHR (upper panel) and Bent (lower panel) model coefficients for a sunspot number of 120.	12
14.	Program GRIDNE structure chart.	46
15.	Summary of the RMS analysis error between the initial, effective F_{10} analysis, and global analysis fields and the Bent field for the entire 24 hour analysis period.	52
16.	The 0000UT analysis grids, $N_e(840)$ grids, and Bent grids for $SSN=120$, 2 satellites.	53
17.	The RMS difference between the input f_p data and f_p calculated from Equation 22 as a function of global analysis iteration number.	55

18.	Analysis results for the first full orbit of both DMSP satellites for test case 1f.	56
19.	Summary of the $N_e(840)$ grid set comparisons for test case 1a (SSN=10, 1 satellite).	59
20.	Analysis results for the 0000UT grid for test case 1a (SSN=10, 1 satellite).	60
21.	Summary of the $N_e(840)$ grid set comparisons for test case 1b (SSN=10, 2 satellites).	61
22.	Analysis results for the 0000UT grid for test case 1b (SSN=10, 2 satellites).	62
23.	Summary of the $N_e(840)$ grid set comparisons for test case 1c (SSN=60, 1 satellite).	63
24.	Analysis results for the 0000UT grid for test case 1c (SSN=60, 1 satellite).	64
25.	Summary of the $N_e(840)$ grid set comparisons for test case 1d (SSN=60, 2 satellites).	65
26.	Analysis results for the 0000UT grid set for test case 1d (SSN=60, 2 satellites).	66
27.	Summary of the $N_e(840)$ grid set comparison for test case 1e (SSN=120, 1 satellite).	67
28.	Analysis results for the 0000UT grid for test case 1e (SSN=120, 1 satellite).	68
29.	Summary of the $N_e(840)$ grid set comparisons for test case 1f (SSN=120, 2 satellites).	69
30.	Analysis results for the 0000UT grid for test case 1f (SSN=120, 2 satellites).	70
31.	The 0000UT analysis and $N_e(840)$ grids for the Stations, Grid 1, and Grid 2 analyses, and the Bent 0000UT $N_e(840)$ grid.	76
32.	The 0000UT analysis grids and $N_e(840)$ grids for the Stations (NT) and Grid 3 (NT) analyses, and the Bent 0000UT $N_e(840)$ grid.	78

LIST OF TABLES

<u>Table</u>	<u>Caption</u>	<u>Page</u>
1.	Initial values of the normalization constants.	18
2.	Profile parameter values.	20
3.	Constants for use in Equation 21 describing the variation of h_p with solar epoch.	33
4.	Description of program GRIDNE routines.	46
5.	Test parameters.	50
6.	Results of the effective F10 analyses in Test 1.	54
7.	Summary of the results of the $N_e(840)$ grid set comparisons.	57
8.	Test 2 results summary.	71
9.	Test 3 results summary.	72
10.	TEC station penetration point locations.	74
11.	TEC tests results summary.	74
12.	Results of the SSIE effective F10 analyses.	79

1. INTRODUCTION

Defense Meteorology Satellite Program (DMSP) Block 5D satellites have included Topside Ionospheric Plasma Monitor (SSIE) sensors since mid 1977^{2,3}. Ionospheric electron density, $N_e(840)$, and plasma scale height, $H_p(840)$, from the SSIE sensors are routinely processed at the Air Force Global Weather Center (AFGWC) for specification of the state of the earth's ionosphere. Figure 1 is a simplified flow diagram of data from the SSIE sensors within AFGWC. SSIE data are stripped from the DMSP satellite telemetry stream and written to a temporary file (IEPREPFILE) by the AFGWC DMSP processing system. Program SSIE reads the raw SSIE data from this file, calculates electron densities and plasma scale heights^{2,3}, and writes out a data record for every 64 seconds containing an average $N_e(840)$ value and $H_p(840)$ value to a temporary file (IFLUXFILE). Program LDIPIE reads the data records from this file, reformats them, and writes them into the Astrogeophysical Data Base (AGDB)⁴. Program SSIELD reads SSIE $N_e(840)$ data for the most recent 24 hours from the AGDB, constructs 10° latitude by 15° longitude northern-hemisphere grids of $N_e(840)$ for each of the 24 hours, and writes them to a gridded-data file (FOURUGRIDS)⁵. These data are merged with data grids from the f_oF_2 and TEC preprocessors and written to temporary file 18 by program GRDOUT as observation data sets². The Air Weather Service (AWS) 4D Ionospheric Analysis Model^{6,7} inputs the observation data sets from temporary file 18 and produces a consistent analysis of the ionospheric electron density distribution over the entire northern hemisphere.

The primary objective of this project is to study methods for improving the use of the SSIE $N_e(840)$ and $H_p(840)$ data by the 4D model system, identified in Figure 1 by those files and programs within the dashed box. The studies have focused on possible improvements to the 4D model, particularly to its internal electron-density profile model, and to the various 4D model system preprocessors.

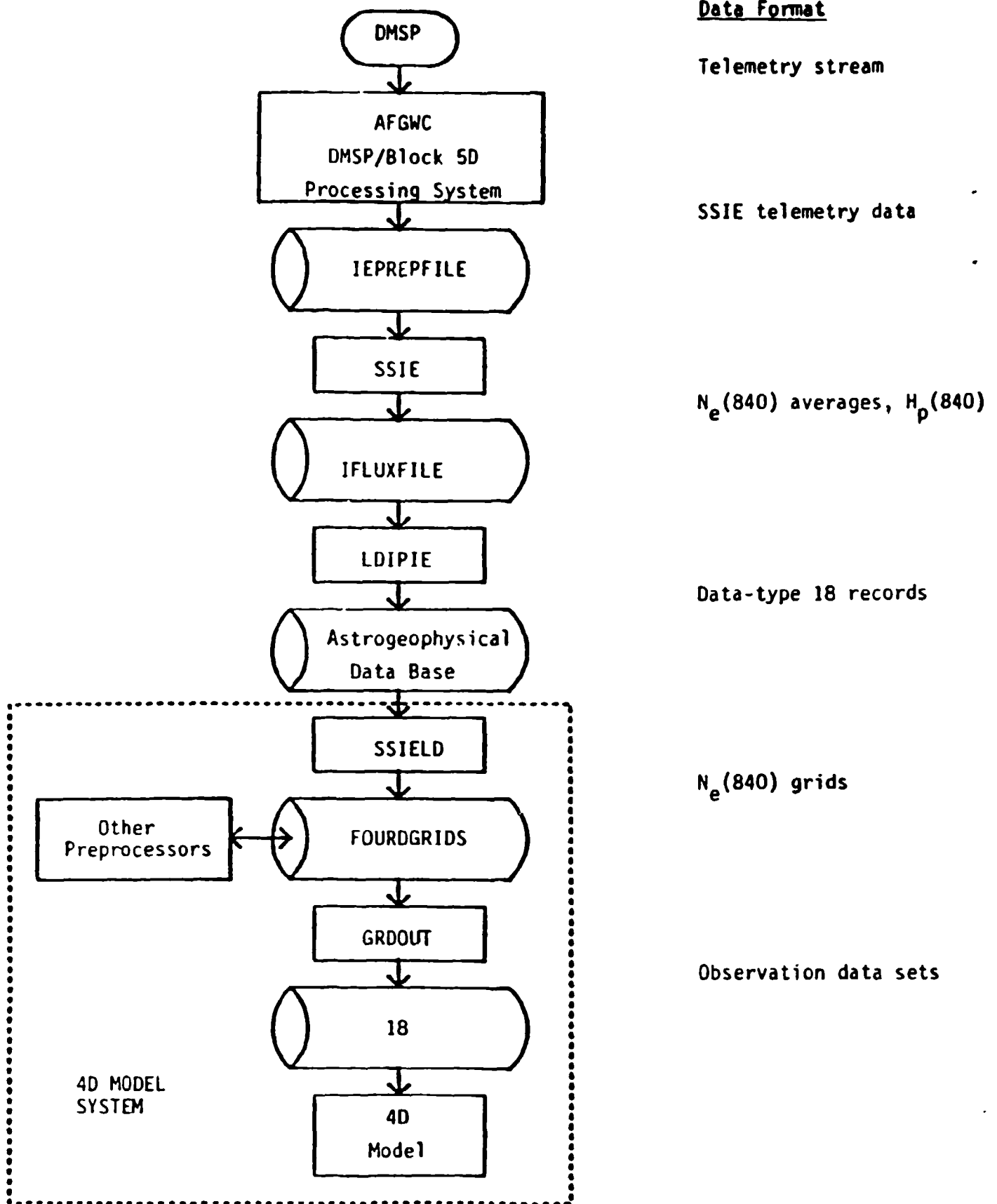


Figure 1. SSIE data processing flow at AFGWC.

2. PROJECT DEFINITION

The first step in the project was to define specific tasks to pursue within the areas of research defined in the project proposal and statement of work. This study resulted in the following list of tasks to be completed during the project:

a. Task 1: Determine the modifications required to configure the 4D ionospheric analysis model for a full global analysis.

b. Task 2: Investigate the use of the profile parametrization used in the IRI79 reference ionosphere⁸ as a replacement for the parametrization currently used in the 4D model.

c. Task 3: Derive sets of height-profile basis functions for the 4D model using plasma frequency profiles from the IRI79 reference ionosphere.

d. Task 4: Investigate techniques for improving the preparation of data grids of $N_e(840)$ from the SSIE $N_e(840)$ observations.

e. Task 5: Work with personnel from AFGL and AFGWC to develop improved techniques for combining TEC and SSIE $N_e(840)$ data into a single specification of the topside ionosphere.

f. Task 6: Investigate alternative parametrizations of the topside ionosphere which would use the full set of data available from the SSIE sensors and all other available data, including Total Electron Content (TEC) data, to specify the electron density profile above the F2-layer peak.

g. Task 7: Begin an investigation into ways to use data from the SSIE sensors, in conjunction with other observations, for modeling the ionospheric subauroral trough as part of the 4D model preprocessor system.

These tasks fall generally into three main studies: 1) Topside Profile Model Study (Tasks 2 and 6), 2) Ionospheric Data Preprocessor Improvements Study (Tasks 4, 5, and 7), and 3) 4D Model Improvements Study (Tasks 1 and 3). Tasks 1, 2, and 3 were completed during the first year of the study and the outcomes reported in Scientific Report No. 1 of this contract⁹. Task 7 was to be worked as resources allowed. As the work on improvements to the $N_e(840)$

gridding program (Task 4) grew in scope during the course of the project, there were no resources available to put on Task 7. The work completed in Tasks 4, 5, and 6 will be reported here..

3. TOPSIDE PROFILE MODEL STUDY

This study includes Tasks 2 and 4 of the project. The overall objective of this study is to investigate improved parametrizations of the topside ionospheric electron density profile for use within the 4D model.

3.1 Task 2: IRI79 Topside Parametrization

The major thrust of this task was to investigate the IRI79 model to determine if 1) the IRI79 topside parametrization could be modified for use within the 4D model, and 2) the profile shape provided by the IRI79 was sufficiently better than the Damon-Hartranft-Ramsay (DHR) profile model^{10,11} currently used by the 4D model to justify replacing the DHR model with IRI79. As reported earlier⁹, the conclusion of the investigation was that the IRI79 was not a viable replacement for the DHR model, so work was terminated on this task and begun on Task 6.

3.2 Task 6: Alternative Topside Parametrizations

The purpose of this task was to investigate parametrizations of the topside electron density profile (EDP) which would represent a two-constituent (O^+ and H^+) topside ionosphere and which could be easily adjusted to fit observed conditions. The objective was to find a parametrization which could use the full complement of observations available from the SSIE (and SSIES) sensor, which includes the O^+ and H^+ densities, $N(O^+)$ and $N(H^+)$, and the electron and ion temperatures, T_e and T_i , in conjunction with ground-based observations of f_oF2 , h_mF2 , and TEC. It was decided during the first year of the project to base the parametrization on a model of the O^+ to H^+ transition height, h_T , defined as the height at which $N(O^+) = N(H^+)$. This task then divided into two subtasks: an investigation of EDP models based on h_T , and the development of a model for h_T .

3.2.1 Profile Model

3.2.1.1 Model Development and Definition

Several different topside electron density profile (EDP) model parametrizations were investigated as part of this task. These included modified versions of the AWS DHR model¹¹ and the Bent model¹², two models based on a parametrization of the topside scale height profile developed to analyze topside sounder data¹³, and a parametrization based on a two-component diffusive equilibrium, (DE) model. For the purpose of calculating TEC, all models used the DHR bottomside model for the EDP below the F2 peak. These models were evaluated against the following criteria:

1. The electron density variation with height, $N_e(h)$, should be continuous and smooth.
2. The scale height variation with height, $H(h)$, should be continuous and reasonably smooth (i.e., as few sharp discontinuities as possible).
3. The model should be capable of fitting a wide range of data types, including f_oF2 , h_mF2 , TEC, and the SSIE data set, but should require only h_mF2 and f_oF2 .
4. Conversely, the model should reflect the basic physical processes active in the topside ionosphere such that it will not produce physically unreasonable profiles in attempting to fit an inconsistent data set. This would be useful in data quality control and in intercomparison of data sets.
5. As implemented on a computer, the profile model and the algorithms used to fit the profile to observations should be as simple and computationally quick as possible and computationally stable.

The first four parametrizations considered, which are briefly described in Appendix B, all met the first two criteria, but ran into difficulties with one or more of the last three, particularly numbers three and four. The primary reasons for rejecting the various models were as follows:

1. Modified DHR model. Although initially attractive, this model was abandoned fairly early for a number of reasons. In order to produce a profile

with only $h_m F2$ and $f_o F2$ input, a model would be required to provide the scale height for the exponential layer above $h=h_T$, and the DHR scale height model¹¹ would need to be modified to account for the addition of the exponential layer. Both actions would require analysis of large amounts of data which were not available. Additionally, the procedures to fit the profile to observed SSIE data became very cumbersome, and could very easily produce unrealistic profiles.

2. Modified Bent model. This parametrization was developed as a solution to the limited-data-profile problem encountered with the modified DHR model. Unfortunately, the data-fitting procedures proved to be as cumbersome as with the modified DHR model, and, in some cases, the model produced $N_e(h)$ curves which increased with height.

3. Titheridge H(h) model. This model was considered in an attempt to control the physically unrealistic behavior exhibited by the first two models. As with the first two models, the data-fitting procedures were a problem. Not only were they cumbersome, but they were also computationally unstable under reasonable conditions. Although the Titheridge model was difficult to use in fitting observations, this was more a problem with the particular parametrization chosen than an inherent problem with a diffusive equilibrium (DE) distribution. This led to developing a parametrization of a DE profile more suited to the present application.

The height distribution of the ion density for a topside ionosphere in diffusive equilibrium is given by¹⁴

$$N_i = \sum_j N_o(x_j^+) \exp \left\{ - \int_{h_0}^h \left[\left(m_j - \bar{m} \frac{T_e}{T_p} \right) \frac{g}{kT_i} + \frac{1}{T_p} \frac{\partial T_p}{\partial h} \right] dh \right\} \quad (1)$$

where $N_o(x_j^+)$ is the density of ion species j at the reference height h_0 , T_p is the plasma temperature ($T_e + T_i$), m_j is the mass of species j , and \bar{m} is the mean ionic mass given by

$$\bar{m} = \left(\sum_j N(x_j^+) m_j \right) / \sum_j N(x_j^+) .$$

Collecting the terms which are species-independent, Equation 1 can be rewritten

$$N_i = e^{-\tau} \sum_j N_0(x_j^+) \exp \left(- \int_{h_0}^h \frac{m_j g}{kT_i} dh \right)$$

where

$$\tau = \int_{h_0}^h \left[\left(\frac{T_e}{T_i} \right) \left(\frac{\bar{m}g}{kT_p} \right) - \frac{1}{T_p} \frac{\partial T_p}{\partial h} \right] dh \quad (2)$$

Integrating the second term in Equation 2 then gives

$$N_i = \left[\frac{T_{p0}}{T_p} \right] e^{u} \sum_j N_0(x_j^+) \exp \left(- \int_{h_0}^h \frac{m_j g}{kT_i} dh \right)$$

where

$$u = \int_{h_0}^h \left(\frac{T_e}{T_i} \right) \frac{\bar{m}g}{kT_p} dh$$

For an ionosphere consisting of O^+ and H^+ ions in diffusive equilibrium, the mean ionic mass can be simplified to

$$\bar{m} = m_+ \left(\frac{16+R}{1+R} \right)$$

where m_+ is the mass of H^+ , and R is the ratio of $N(H^+)$ to $N(O^+)$ given by¹⁴

$$R \equiv \frac{N(H^+)}{N(O^+)} = R_0 \exp \left[\int_{h_0}^h \frac{15m_+ g}{kT_i} dh \right] \quad (3)$$

Thus, for an O^+ , H^+ ionosphere in diffusive equilibrium, the density distribution becomes

$$N_i = \left[\frac{T_{p0}}{T_p} \right] e^{u} \left[N_0(O^+) e^{-16I} + N_0(H^+) e^{-I} \right] \quad (4)$$

where

$$u = \int_{h_0}^h \left(\frac{T_e}{T_i} \right) \left(\frac{m_+ g}{kT_p} \right) \left(\frac{16+R}{1+R} \right) dh$$

$$R = R_0 e^{15I} \quad (5)$$

$$I = \int_{h_0}^h \frac{m+g}{kT_i} dh, \text{ and}$$

$$g = 9.8 \left(\frac{6371}{6371+h} \right)^2 \text{ m/sec}^2.$$

This provides a topside model which requires a model for $T_e(h)$ and $T_i(h)$, some method for determining $N_0(0^+)$ and $N_0(H^+)$, and a way to couple the profile to the F2 peak at $h_m F2$.

A recent empirical model based on data from the AE-C satellite¹⁵ was chosen to describe the height variation of T_e and T_i . In this model, both parameters are represented by equations of the form

$$T_j = \sum_{h=0}^3 a_{nj} \left(\frac{100}{h} \right)^n \quad (6)$$

where the coefficients, a_{nj} , are functions of geomagnetic latitude and local time. In the original model, summer solstice values for $T_j(h)$ were given for northern magnetic latitudes and winter solstice values were given for southern magnetic latitudes. This was modified to provide a seasonal variation at all latitudes by multiplying the non-symmetric (in latitude) terms in the expression describing the a_{nj} coefficients by $\cos [(2\pi/365)(D + 192)]$ where D is the day of the year.

It was decided to use the Bent topside parabolic layer to describe the profile from $h_m F2$ to the base of the DE model for three reasons. First, a parabolic layer approximates the shape of the EDP near the F2 peak fairly well; second, it is a mathematically simple representation, with the density and scale height given by

$$N_e = N_m F2 \left[1 - \left(\frac{h-h_m F2}{y_t} \right)^2 \right] \quad (7)$$

and

$$H = \frac{1}{2} \left[\frac{y_t^2 - (h-h_m F2)^2}{h-h_m F2} \right] \quad (8)$$

where y_t is the semi-thickness; and third, the Bent model values for y_t can be used in conjunction with a model for the O^+ to H^+ transition height, h_T , to specify $N_o(O^+)$ and $N_o(H^+)$, thereby requiring only f_oF2 and h_mF2 to specify the entire profile. This is done by determining the height, h_1 , at which the scale height given by Equation 8 is equal to that calculated from

$$H_{DE} = \left[\frac{1}{N_e} \frac{\partial N_e}{\partial h} \right]^{-1} \quad (9)$$

where $N_e(h)$ is given by Equation 4 (assuming $N_e(h) = N_i(h)$), and using the density at that height from Equation 7 to determine $N_o(O^+)$ and $N_o(H^+)$.

It is possible to do this because the scale height defined by Equations 9 and 4 is not a function of $N(O^+)$ or $N(H^+)$, but rather of their ratio, R . For an O^+/H^+ ionosphere, Equation 1 can be rewritten

$$N_i = N(O^+) + N(H^+) \quad (10)$$

where

$$N(x_j^+) = N_o(x_j^+) \exp \left[- \int_{h_o}^h f(x_j^+) dh \right]$$

and

$$f(x_j^+) = \left(m_j - \bar{m} \frac{T_e}{T_p} \right) \frac{g}{kT_i} + \frac{1}{T_p} \frac{\partial T_p}{\partial h} \quad (11)$$

Combining Equations 9 and 10,

$$H_{DE} = \frac{N(O^+) + N(H^+)}{N(O^+)f(O^+) + N(H^+)f(H^+)}$$

or, from Equation 3,

$$H_{DE} = \frac{1 + R}{f(O^+) + Rf(H^+)}$$

Using the expression for $f(x_j^+)$ from Equation 11, this becomes

$$H_{DE} = \frac{1}{\left(1 - \frac{T_e}{T_p}\right) \frac{\bar{m}g}{kT_i} + \frac{1}{T_p} \frac{\partial T_p}{\partial h}} \quad (12)$$

Since \bar{m} is only a function of R , H_{DE} is not a function of the densities, $N_O(O^+)$ and $N_O(H^+)$, but rather their ratio, R_O .

Given values for $h_m F2$, $f_o F2$, and h_T , this fact can be used to fit the parabolic and DE profiles together as follows:

1. Set h_o to h_T . Since h_T is defined as the height where $N(O^+) = N(H^+)$, then $R_O = 1.0$.

2. Using Equations 8 and 12 with the temperature model (Equation 6), iteratively locate the height, h_1 , at which the scale heights from Equations 8 and 12 are the same.

3. Calculate the total ion (electron) density at this height, $N_e(h_1)$, from Equation 7. The densities for O^+ and H^+ at h_1 can then be calculated from

$$N_1(O^+) = \frac{N_e(h_1)}{1 + R(h_1)}, \text{ and}$$

$$N_1(H^+) = R(h_1)N_1(O^+).$$

4. Set h_o to h_1 , R_O to $R(h_1)$, $N_O(O^+)$ to $N_1(O^+)$, and $N_O(H^+)$ to $N_1(H^+)$.

All profile parameters are now calculated.

3.2.1.2 Fitting Profiles to Data

The various types of inospheric observations available are used to adjust the profile model as follows:

a. The ion densities, $N_s(O^+)$ and $N_s(H^+)$, the ion temperature, T_{is} , and the electron temperature, T_{es} , at the satellite altitude are used to calculate the O^+/H^+ transition height, h_T .

b. The temperatures, T_{is} and T_{es} , can be used to adjust the AE-C temperature model.

c. The electron density at the satellite ($N_e(840)$), f_oF2 , h_mF2 , and TEC are used to adjust various model parameters so that the resulting profile matches the observations.

As stated earlier, the only data required in order to build a profile are f_oF2 and h_mF2 . All other observations are used as available.

The transition height is calculated from Equation 3 for the height variation of the ratio of $N(H^+)$ to $N(O^+)$. Assuming that g is constant, this equation becomes

$$R_o \exp \left[G \int_{h_o}^{h_T} \frac{dh}{T_i} \right] = 1.0$$

at the transition height, and

$$R_o \exp \left[G \int_{h_o}^{840} \frac{dh}{T_i} \right] = R_s \left[\frac{N_s(H^+)}{N_s(O^+)} \right]$$

at the satellite altitude, where $G = 15m_+g/k$. Combing these yields

$$\int_{h_T}^{840} \frac{dh}{T_i} = \frac{1}{G} \ln R_s$$

If T_i is assumed to vary linearly with height between h_T and 840km, the integral becomes

$$\int_{h_T}^{840} \frac{dh}{T_{is} + \frac{\Delta T_i}{\Delta h} (h-840)} = \frac{1}{\Delta T_i} \ln \left| 1 + (h_T-840) \frac{\Delta T_i}{T_{is}} \right|$$

so that

$$h_T = 840 + \frac{T_{is}}{\Delta T_i} (R_s^Y - 1) \quad (13)$$

where $Y = \Delta T_i k / 15m + g$. In order to reduce errors introduced by assuming constant values for g and ΔT_i , the transition height is calculated iteratively as follows:

1. Set g to its value at 840km, calculate ΔT_i at 840km from the AE-C model, and calculate an initial estimate for h_T from Equation 13.
2. Calculate a new estimate for h_T using values for g and ΔT_i at a height midway between the last estimate for h_T and 840km.
3. Iterate on step 2 until the change in h_T from one iteration to the next is below some threshold.

Values for h_T calculated in this fashion can be used either in lieu of the h_T model described in section 3.2.2 or to update and modify this model.

Modifying the profile model to fit observed f_oF2 and h_mF2 with either $N_e(840)$ or TEC, or both $N_e(840)$ and TEC, is also an iterative process. Three profile adjustment parameters were added to the equations describing the profile to facilitate the fitting process. The basic change is to Equation 4, which becomes

$$N_i = \left[\frac{T_{po}}{T_p} \right] e^{\beta h} \left[N_o(0^+) e^{-16\alpha I} + N_o(H^+) e^{-I} \right],$$

$$\alpha = \alpha_0 + \alpha_1 (h-400),$$

where β , α_0 , and α_1 are the adjustment parameters. This change requires modification of Equations 5 and 12 to

$$R = R_o e^{(16\alpha-1)I}$$

and

$$H_{DE} = \frac{1}{\left(\bar{m}^* - \bar{m} = \frac{T_e}{T_p}\right) \frac{g}{kT_i} + \frac{1}{T_p} \frac{\partial T}{\partial h}}$$

where

$$\bar{m}^* = \left(\frac{16\alpha + R}{1 + R}\right) m_+$$

This provides a total of four model parameters which can be adjusted in order to fit a profile to observations - α_1 , α_0 , δ , and y_t .

The variation of $N_e(840)$ and TEC as functions of these parameters is illustrated in Figure 2. All calculations were for mid-latitude at local noon with $f_oF2 = 7$ MHz and $h_mF2 = 350$ km, and the four curves in each plot are for four values of h_T : 650 km, 1000 km, 1500 km, 2000 km. In all plots, the top curve is for $h_T = 650$ km and the bottom is for $h_T = 2000$ km. Also included in this figure are plots showing the variation of $N_e(840)$ and TEC as functions of f_oF2 and $T_p(400)$, the plasma temperature at 400 km, for comparison.

The procedure developed for adjusting the profile parameters to fit observed TEC and $N_e(840)$ allows for a controlled iterative adjustment to any three profile parameters until an adequate fit is achieved. This procedure involves the solution to the equations

$$\Delta x_1 \frac{\partial T}{\partial x_1} + \Delta x_2 \frac{\partial T}{\partial x_2} + \Delta x_3 \frac{\partial T}{\partial x_3} = \Delta T \quad (14)$$

$$\Delta x_1 \frac{\partial N}{\partial x_1} + \Delta x_2 \frac{\partial N}{\partial x_2} + \Delta x_3 \frac{\partial N}{\partial x_3} = \Delta N \quad (15)$$

under the constraint that a normalized change distance, ΔL^2 , given by

$$\Delta L^2 = \left(\frac{\Delta x_1}{c_1}\right)^2 + \left(\frac{\Delta x_2}{c_2}\right)^2 + \left(\frac{\Delta x_3}{c_3}\right)^2 \quad (16)$$

is minimized. In these equations, T and N designate TEC and $N_e(840)$; (x_i , $i=1,3$) are any three profile parameters; and (c_i , $i=1,3$) are three normalization factors. This system of equations is solved by reducing Equation 16 to a single Δx_i variable using Equations 14 and 15, differentiating this with

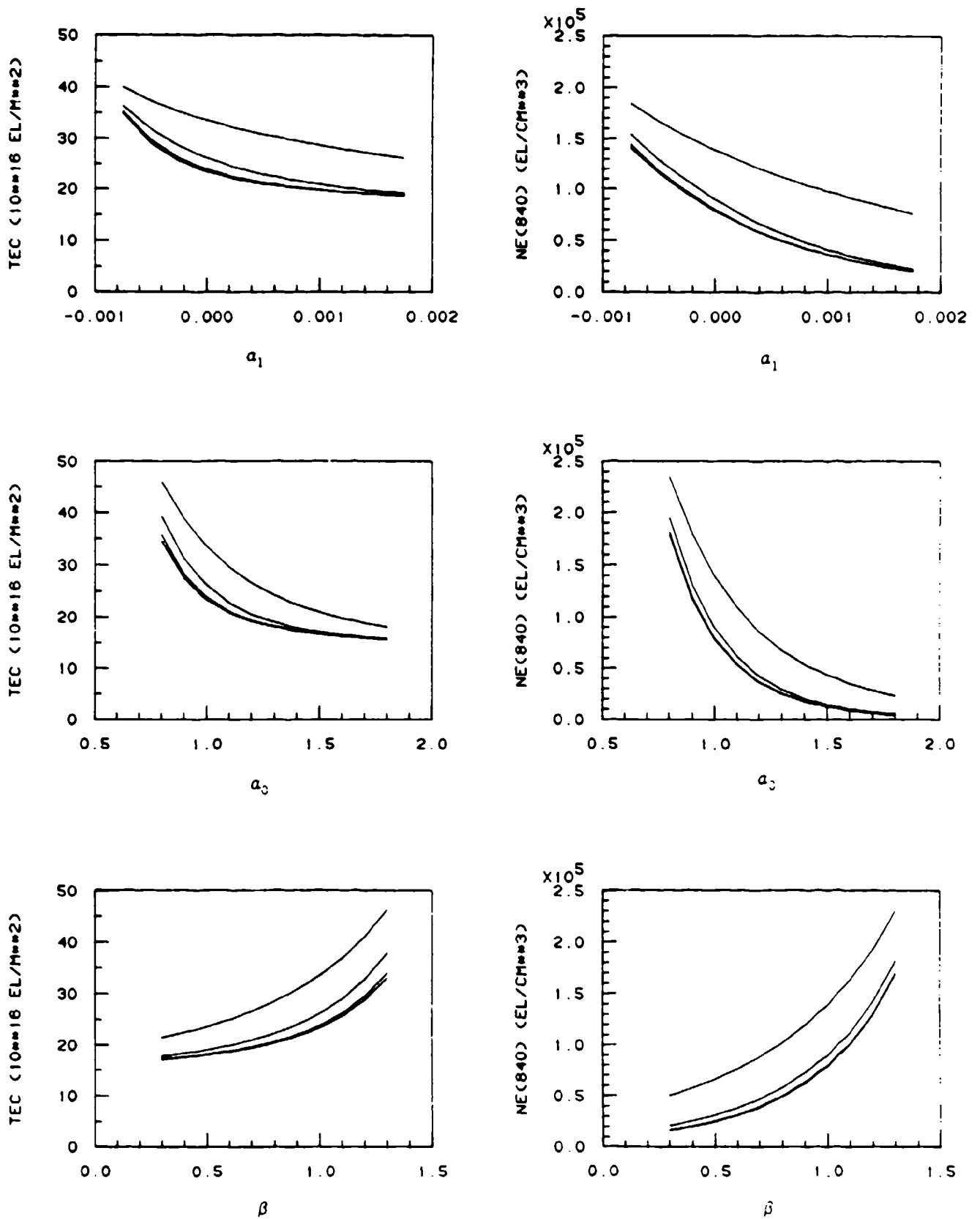


Figure 2. Variation of TEC and $N_e(840)$ with various profile model parameters. See text for details.

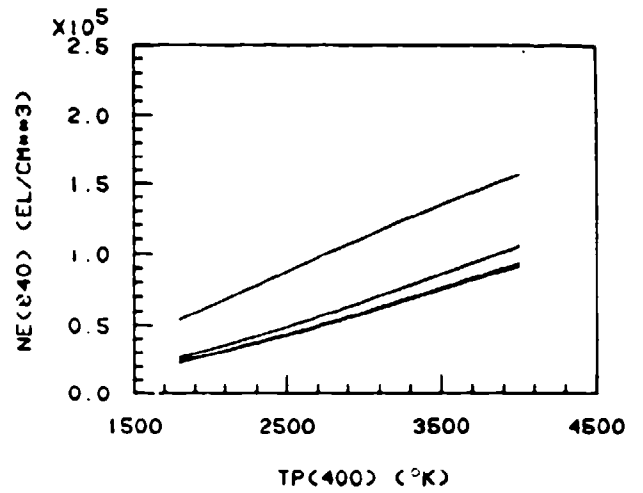
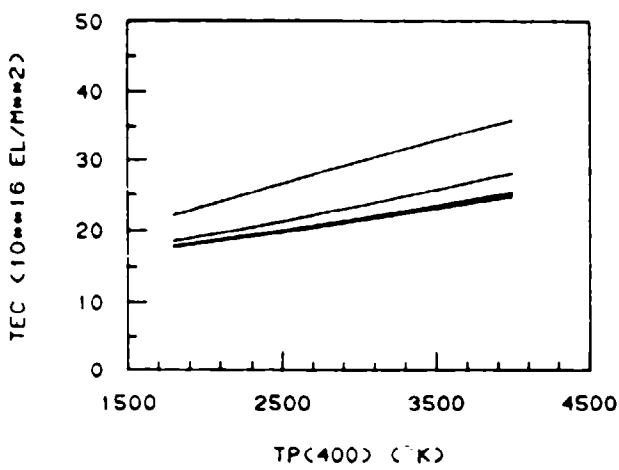
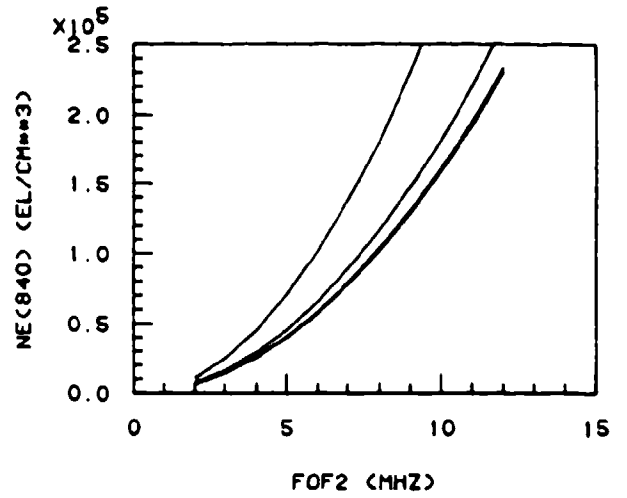
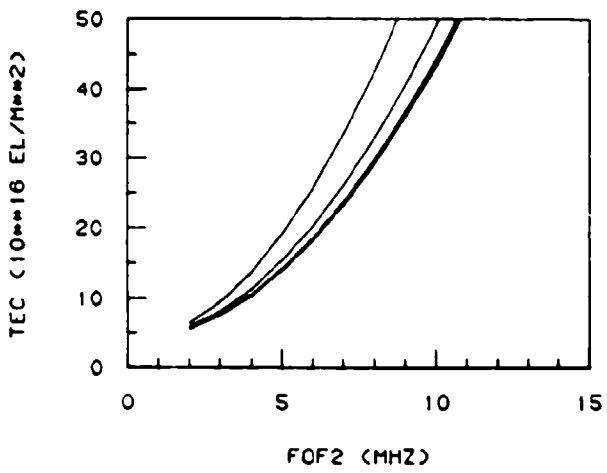
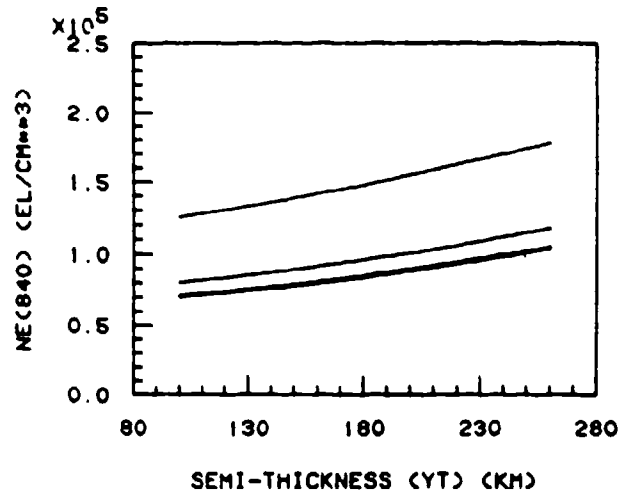
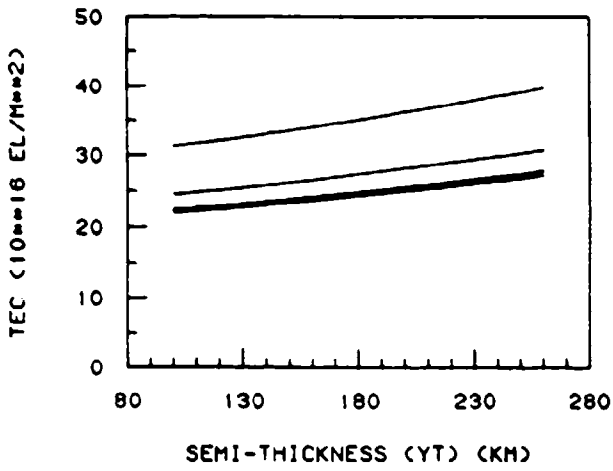


Figure 2. (continued).

respect to Δx_i , and solving for Δx_i . This yields

$$\begin{aligned}\Delta x_1 &= \frac{1}{D^2} \left[\frac{NT_{13}}{c_2^2} \Delta_3 + \frac{NT_{12}}{c_3^2} \Delta_2 \right] \\ \Delta x_2 &= \frac{1}{D^2} \left[\frac{NT_{23}}{c_1^2} \Delta_3 - \frac{NT_{12}}{c_3^2} \Delta_1 \right] \\ \Delta x_3 &= \frac{1}{D^2} \left[-\frac{NT_{23}}{c_1^2} \Delta_2 - \frac{NT_{13}}{c_2^2} \Delta_1 \right]\end{aligned}\tag{17}$$

where

$$\begin{aligned}\Delta_i &= \Delta NT_i - \Delta TN_i, \\ D^2 &= \left(\frac{NT_{23}}{c_1} \right)^2 + \left(\frac{NT_{13}}{c_2} \right)^2 + \left(\frac{NT_{12}}{c_3} \right)^2,\end{aligned}$$

$$NT_{ij} = N_i T_j - T_i N_j,$$

and

$$T_i = \frac{\partial T}{\partial x_i}, \quad N_i = \frac{\partial N}{\partial x_i}.$$

If only one of TEC or N_e (840) is available, a similar set of equations can be used to adjust any two parameters for the fit. For TEC, these are

$$\begin{aligned}\Delta x_1 &= \frac{1}{d^2} \frac{T_i}{c_2} \Delta T, \\ \Delta x_2 &= \frac{1}{d^2} \frac{T_2}{c_1} \Delta T,\end{aligned}\tag{18}$$

where

$$d^2 = \frac{T_2}{c_1}^2 + \frac{T_1}{c_2}^2 .$$

Initially, the normalization constants were included to account for the different ranges of the various parameters and were set to the values shown in Table 1. It was found, however, that the amount, x_i , by which a parameter would be varied could be controlled by adjusting its c_i value with respect to the c_i values of the other parameters being modified.

Table 1. Initial values of the normalization constants.

<u>Parameter</u>	<u>c_i value</u>
β_1	0.0004
β_0	0.07
β	0.07
y_t	20.0
f_oF2	1.0
$T_p(400)$	200.0
h_mF2	20.0
h_T	100.0

As there were no reliable sets of $N_e(840)$ observations available, only a few limited tests were run of the procedures developed for fitting profiles to both TEC and $N_e(840)$ data. Figure 3 illustrates the results of one of these tests. The solid curve is a profile calculated for an f_oF2 of 8.4 and h_mF2 of 314km for a location of 20°N, 203°W (Palehua Observatory in Hawaii) at 1930 local time. This profile has a TEC of $21.8 \times 10^{16} \text{ e1/m}^2$ and an $N_e(840)$ of $4.28 \times 10^4 \text{ e1/cm}^3$. The fitting procedure using Equations 17 was then used to fit to the same $N_e(840)$ for different values of TEC by adjusting parameters y_t , β , and β_0 . The upper and lower dashed curves in Figure 3 are the profiles produced for TEC values of $28.0 \times 10^{16} \text{ e1/m}^2$ and $20.0 \times 10^{16} \text{ e1/m}^2$, respectively. Table 2 lists the values of the three adjusted parameters for each profile. All tests showed this to be a very flexible and robust technique. Further testing and evaluation of this technique must await the availability of reliable *in situ* data from the SSIES sensor.

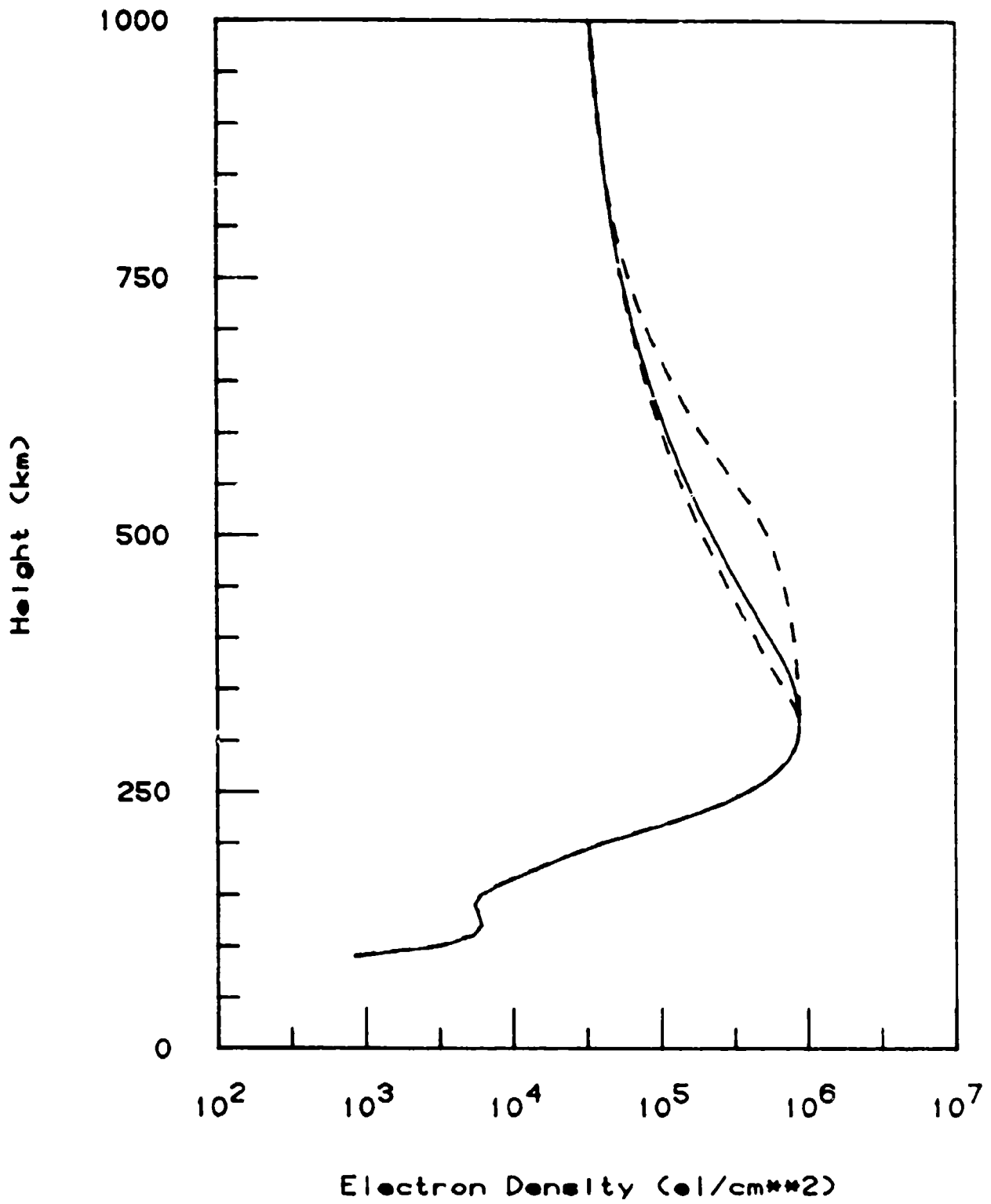


Figure 3. Results of fitting profiles to TEC and $N_e(840)$.

Table 2. Profile parameter values.

<u>TEC</u>	<u>y_t</u>	<u>β</u>	<u>α_0</u>
20.0	69.0	0.985	0.938
21.8	136.0	1.000	1.000
28.0	296.0	0.942	1.318
($\times 10^{16}$ e1/m ²)	(km)		

A more extensive series of tests was carried out on the procedure for fitting profiles to f_oF2 , h_mF2 , and TEC data. A set of near-coincident observations of TEC from the AWS Palehua Observatory and observations of f_oF2 and h_mF2 (calculated from the M3000 factor) from an ionosonde on Maui taken during August and September 1983 were used to investigate the fitting procedure using Equations 18. Two twenty-four hour, five-day mean, data sets were constructed for two geomagnetically quiet periods - one centered on 17 August, the other centered on 4 September. Figure 4 shows the f_oF2 , h_mF2 , and TEC variations for these two data sets. The dashed curve in the two TEC plots is the TEC calculated from the DE profile model using only the f_oF2 and h_mF2 data. Figures 5 and 6 show the adjustments required to fit the observed TEC (within 1/2%) for four pairs of adjustment parameters - α_1 and α_0 , β and α_0 , y_t and α_0 , and β and y_t . Also shown are two cases in which f_oF2 was allowed to vary only by small increments by setting c_i for f_oF2 to 0.3. In all cases, the TEC fit was achieved in less than 5 iterations, with 2-3 iterations being typical. To illustrate the effects of the various modifications on the entire profile, Figures 7 and 8 show the profiles for 1530 LT and 2030 LT from the 02-05 September data set which represent the maximum negative and positive TEC corrections required, respectively. The solid curve shows the initial profile, and the dashed curves show profiles which match the observed TEC through adjustment of the indicated parameters.

3.2.1.3 Model Limitations

Many of the potential limitations of this profile model derive from the assumptions made in developing Equation 4. The most basic of these, that the entire profile is in diffusive equilibrium, is not too bad an assumption a

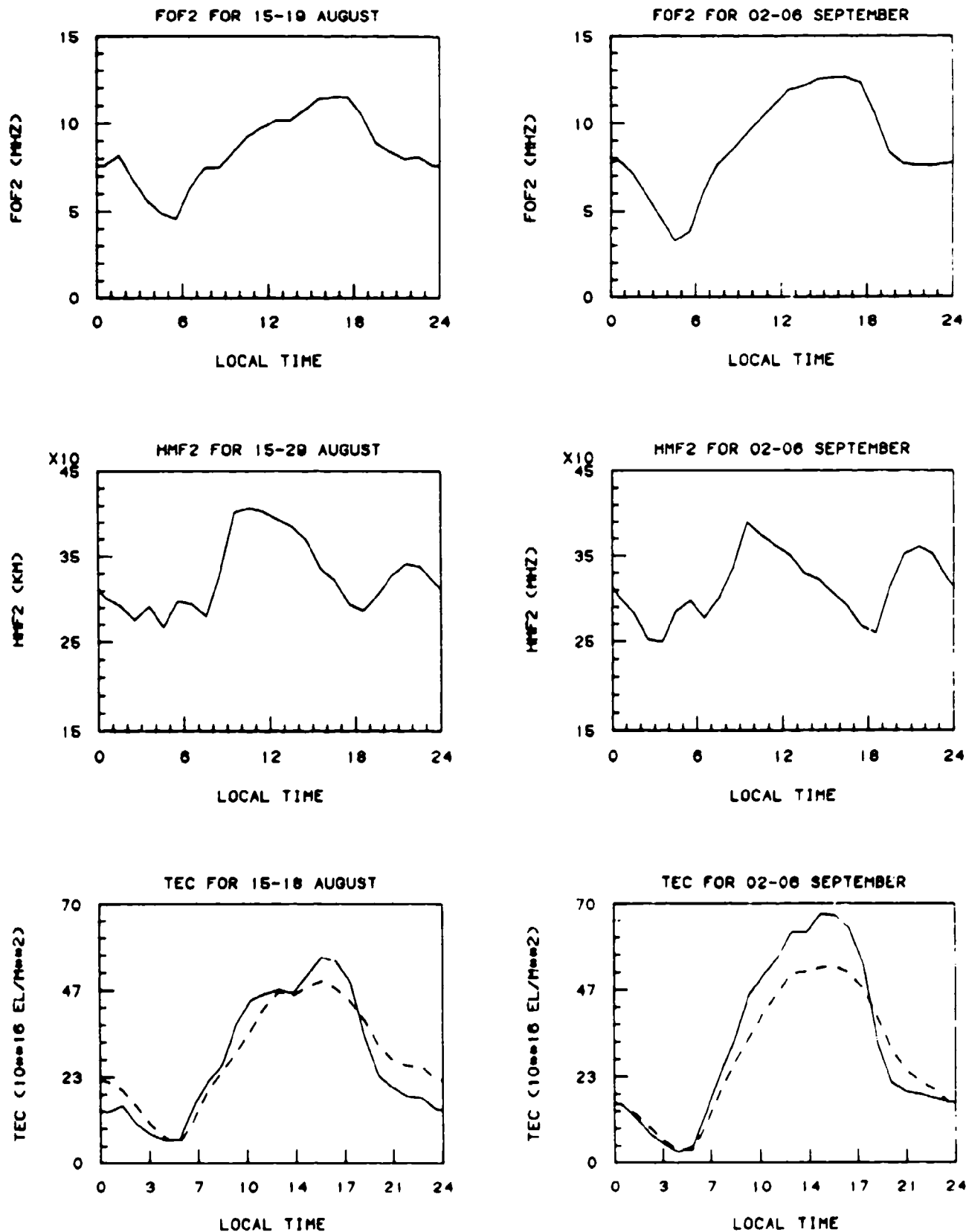


Figure 4. The two data sets used in the TEC fit tests. The dashed curves in the TEC plots are the TEC values calculated prior to attempting to fit to the observed TEC.

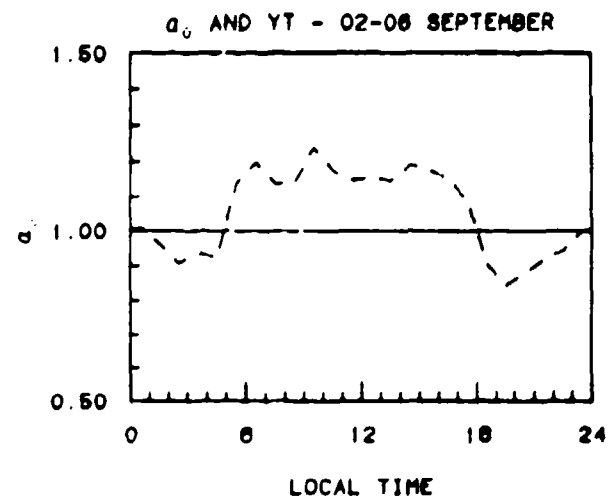
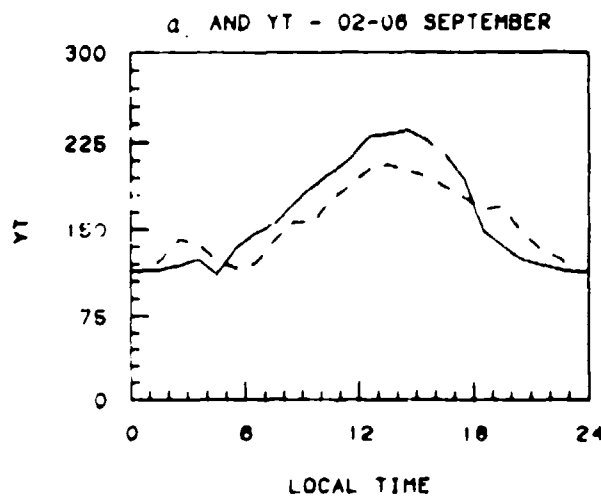
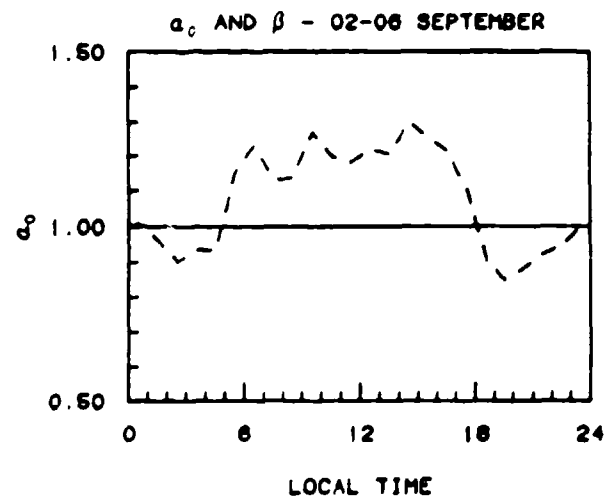
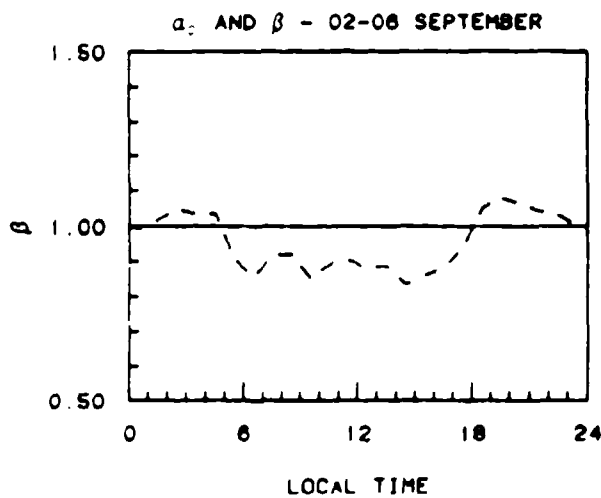
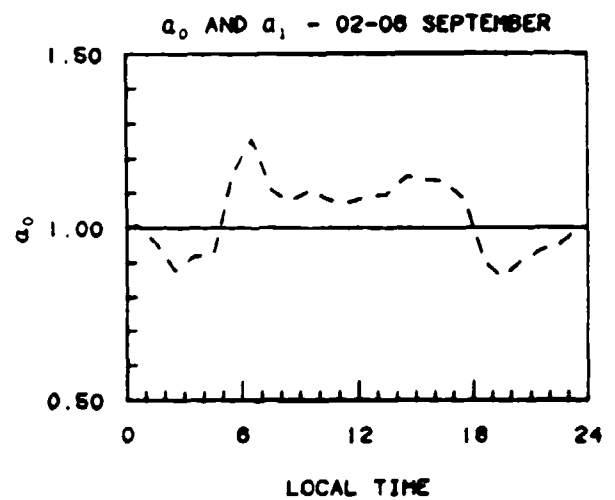
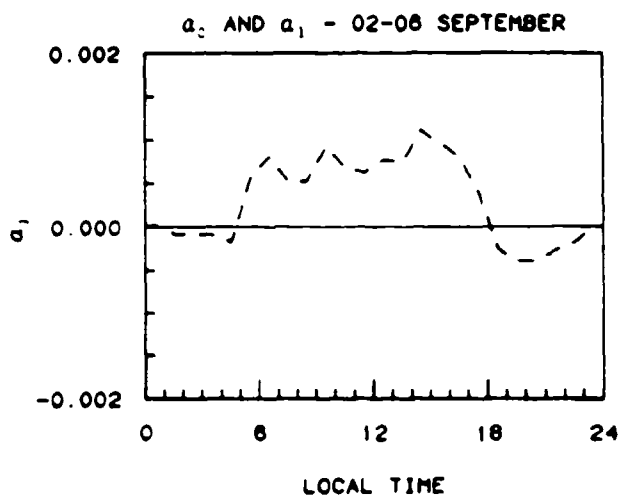


Figure 5. Variation of parameters used to adjust the profile model to fit observed TEC for the 02-06 September data set. Solid curves show the variation prior to the fit, dashed curves show the variation after the fit.

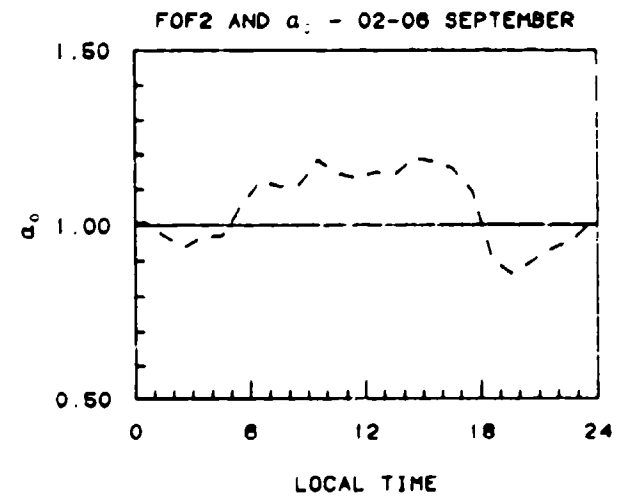
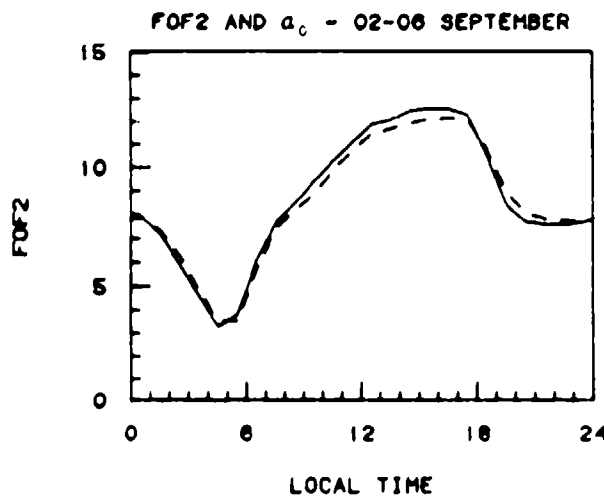
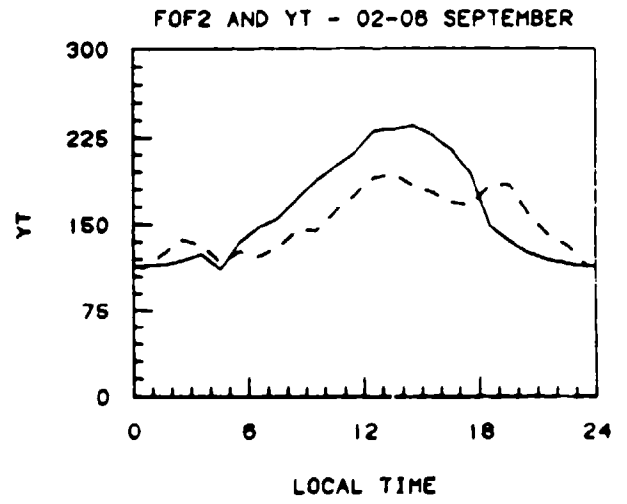
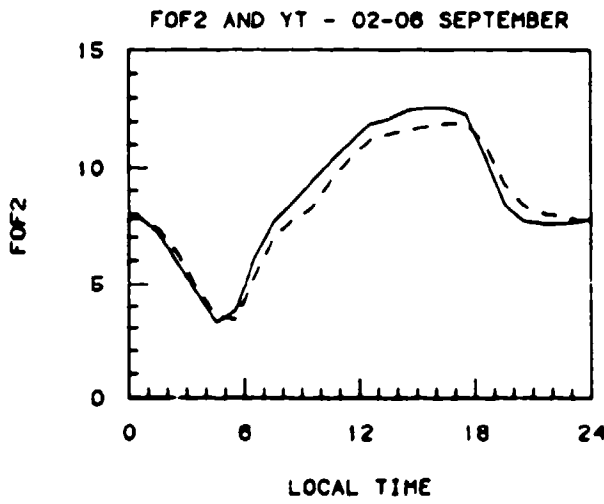
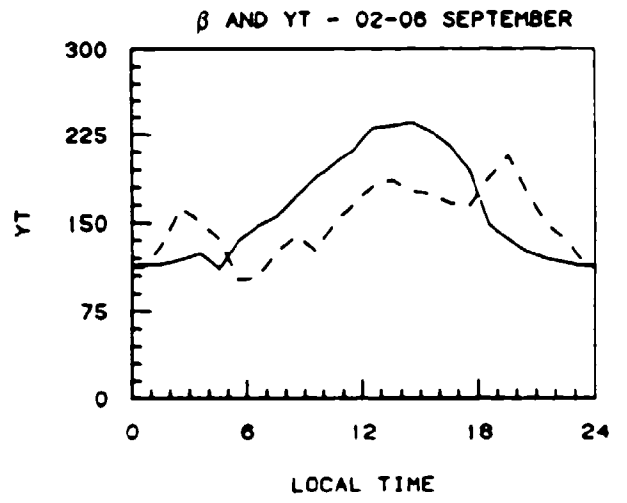
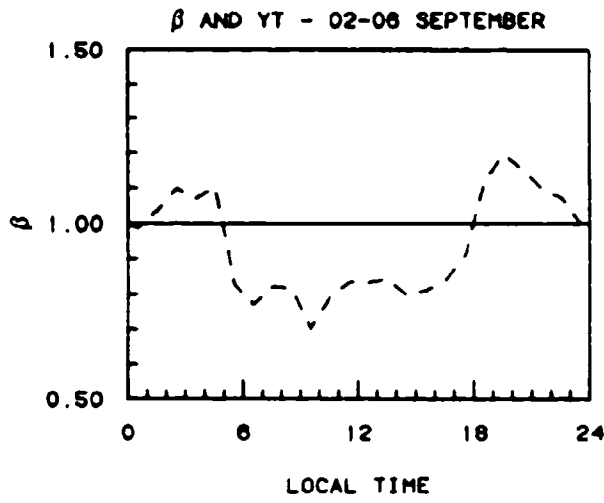


Figure 5. (continued).

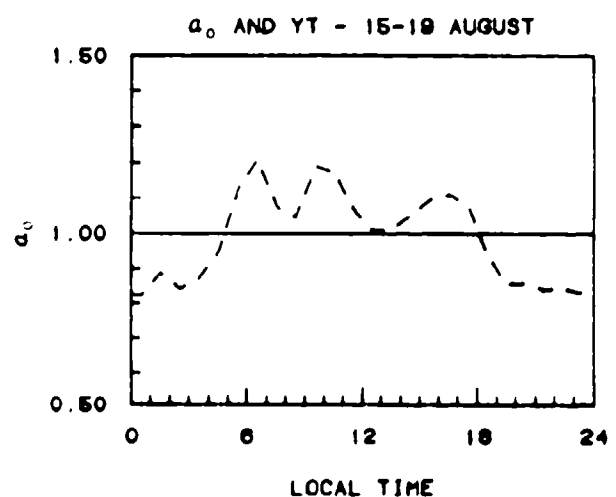
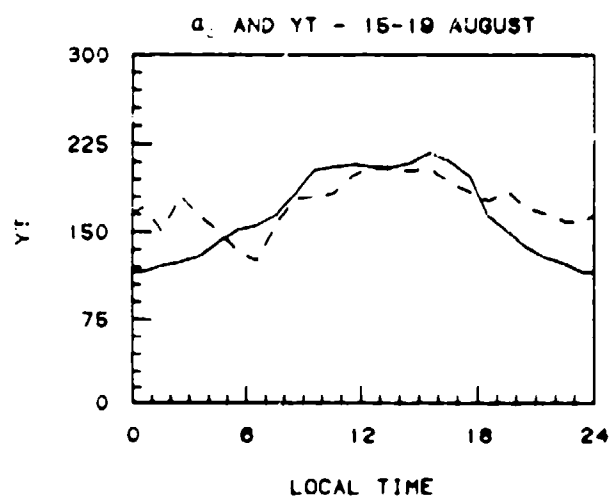
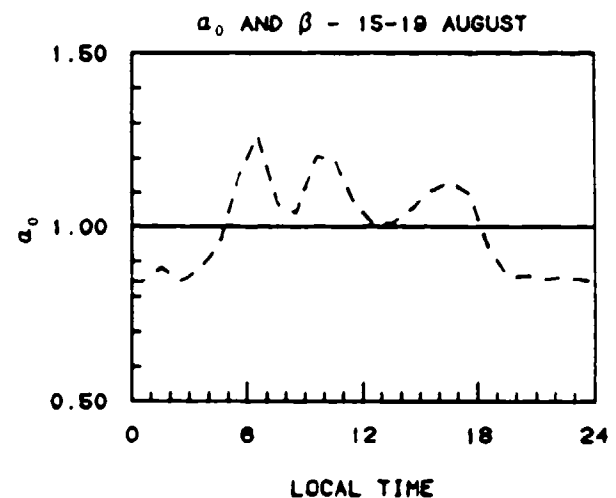
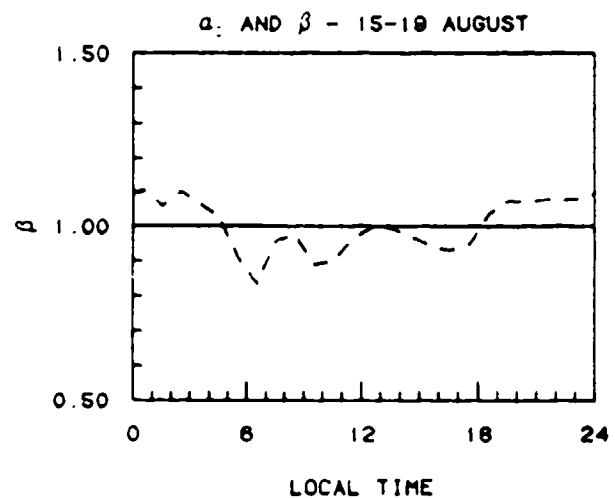
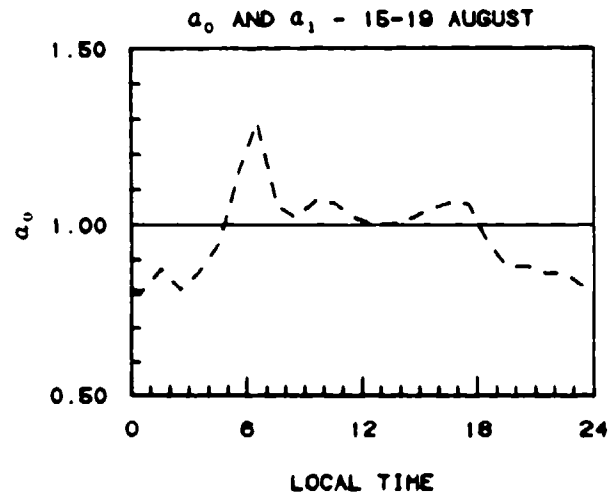
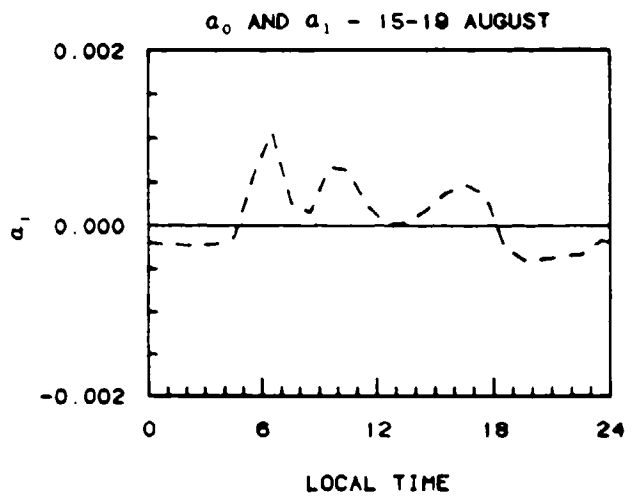


Figure 6. Same as Figure 5 for the 15-19 August data set.

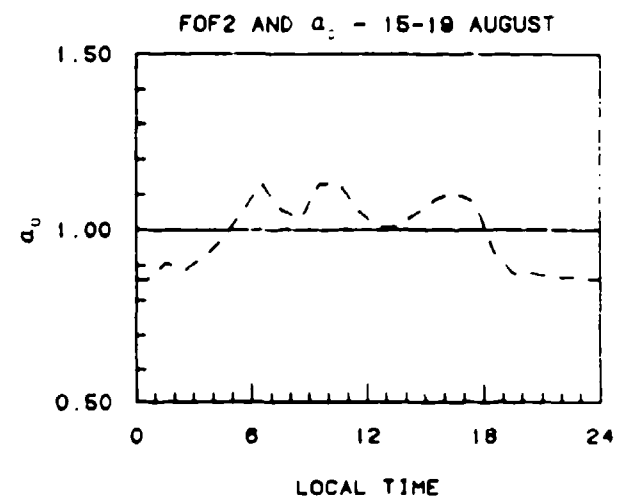
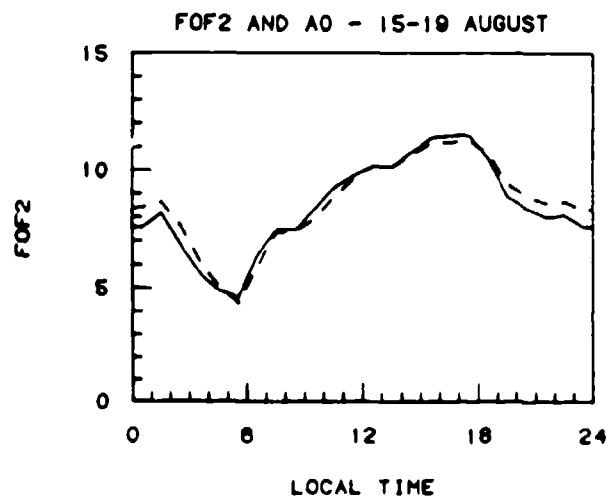
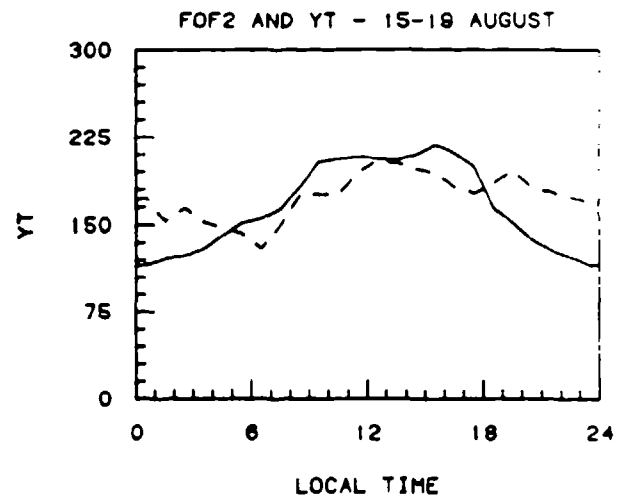
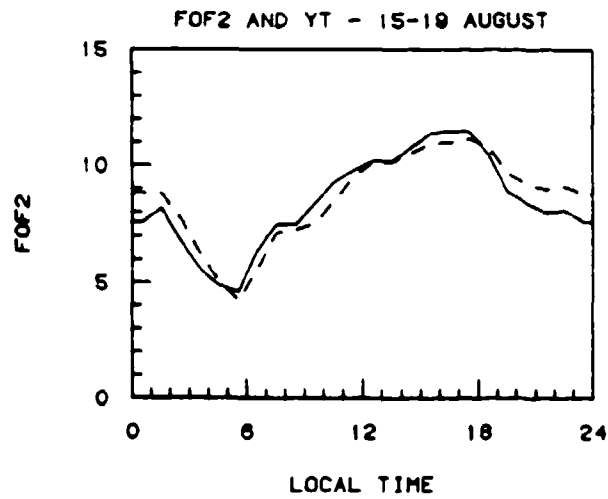
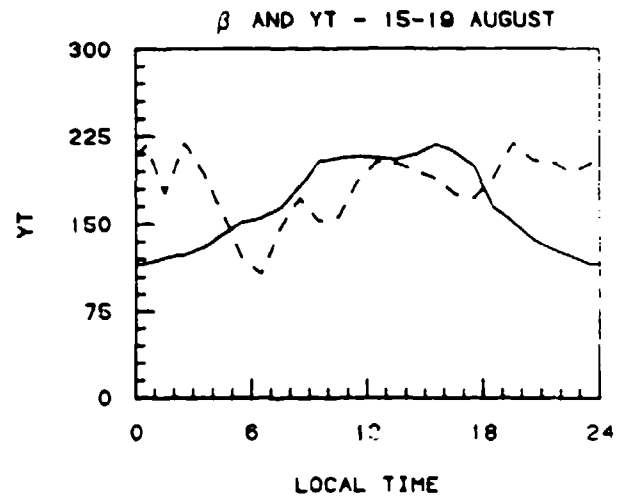
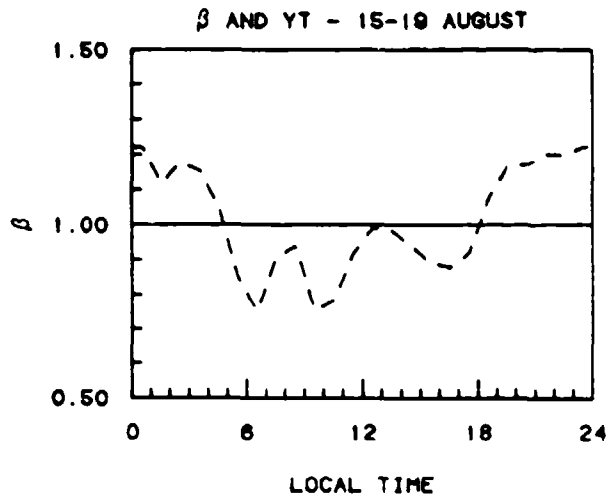


Figure 6. (continued).

1530LT - 02-06 SEPTEMBER

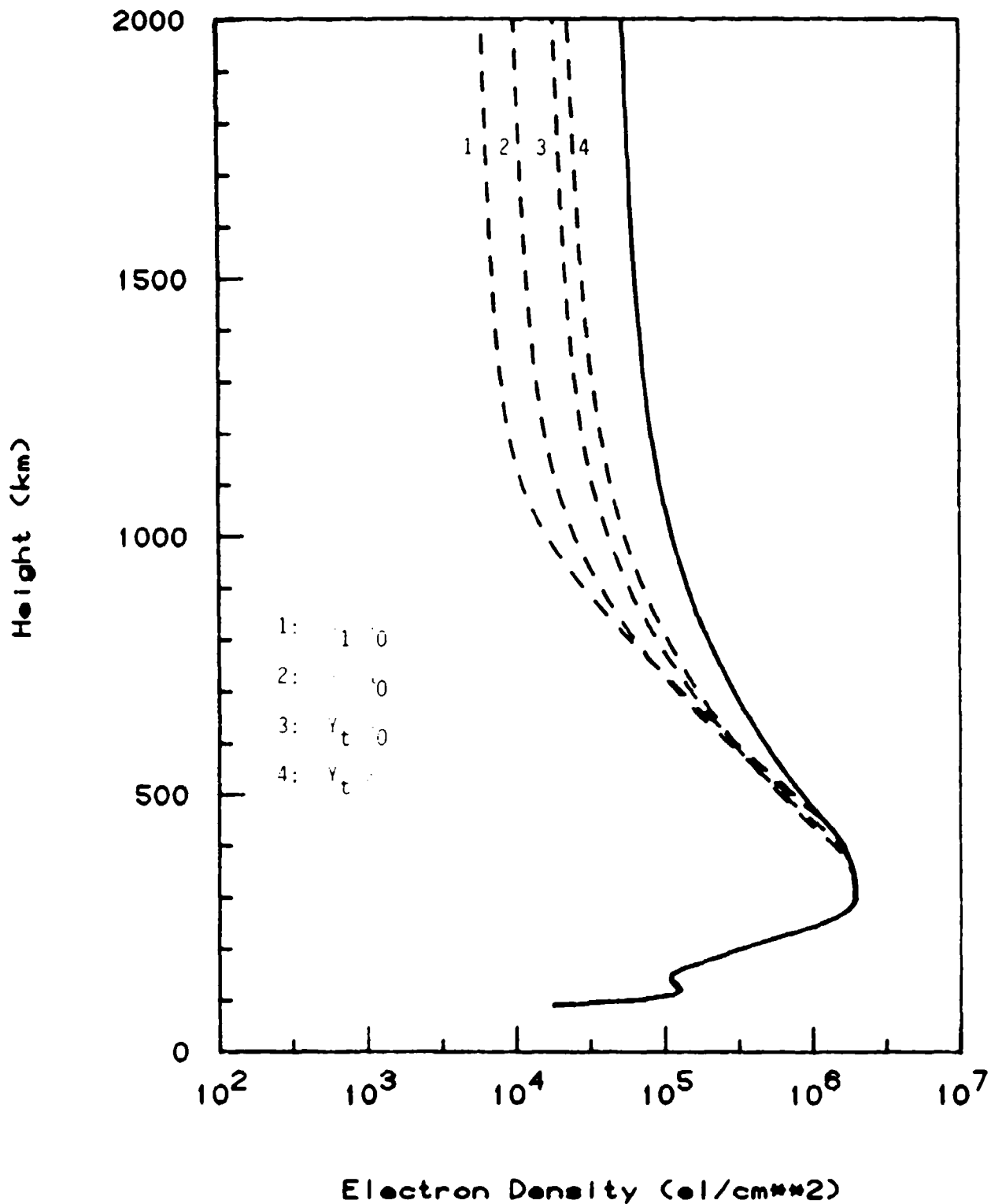


Figure 7. Electron density profiles before (solid curve) and after (dashed curves) adjusting the profile to fit TEC for the 1530LT data from the 02-06 September data set. The dashed curves are labeled with the parameter pairs adjusted to fit the TEC.

2030LT - 02-06 SEPTEMBER

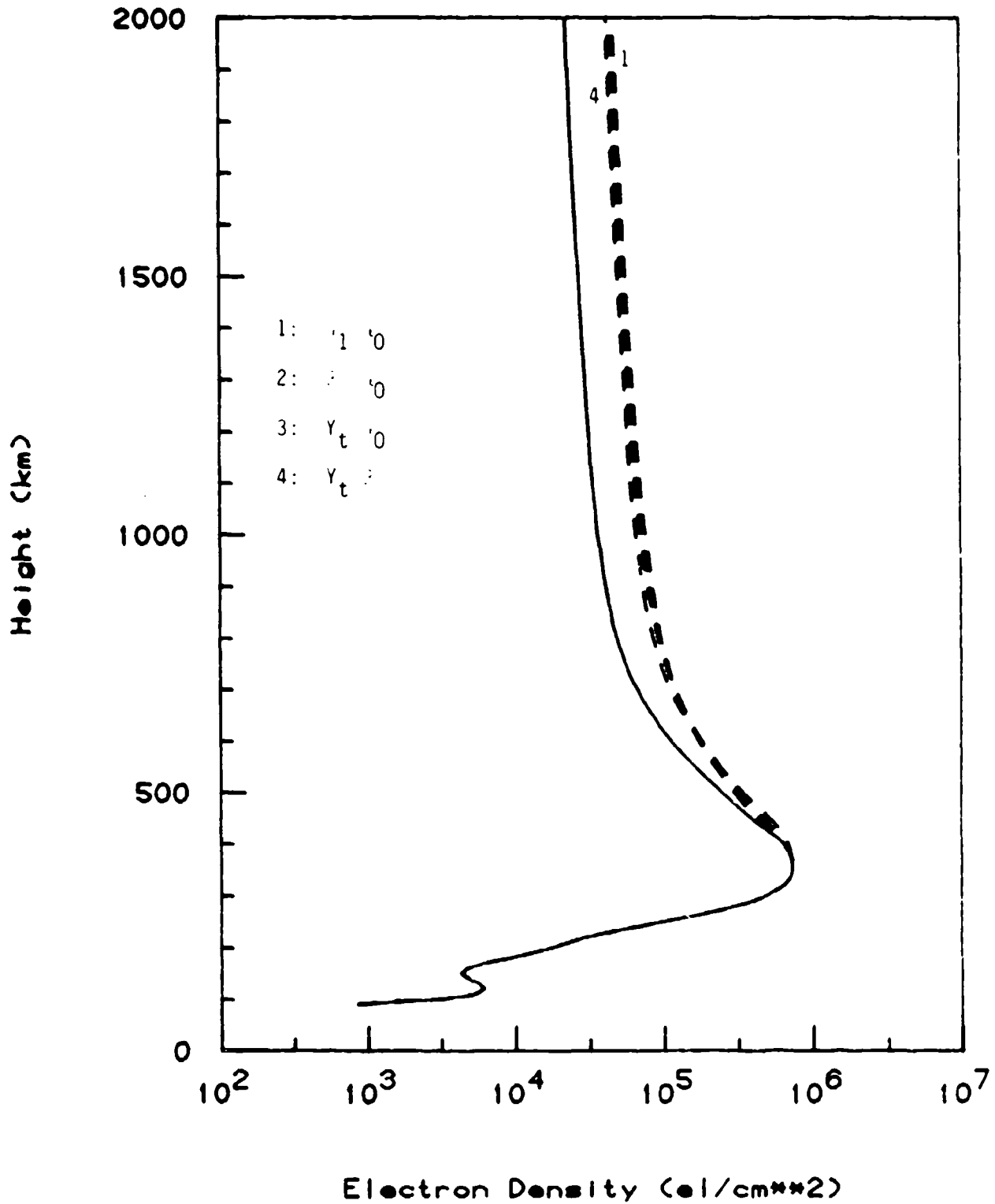


Figure 8. Same as Figure 7 for the 2030LT data from the 02-06 September data set. The dashed curves are labeled 1 through 4 from right to left.

good part of the time. In a study of departures from diffusive equilibrium in the topside ionosphere, Lockwood and Titheridge¹⁶ found that roughly 37% of the more than 10,000 topside soundings they analyzed showed appreciable departures from diffusive equilibrium. The most serious of these were in the equatorial regions (c.f. their Figure 8) where large O^+ fluxes can occur which can seriously effect the shape of the profile just above the F2 peak and can cause appreciable errors in TEC calculated by the model. Additionally, large vertical fluxes of O^+ and H^+ can be found poleward of the plasmapause location which can also seriously deform the vertical density profile. Although neither effect is included in the current model, a systematic study of the adjustments required to fit profiles to data could lead to empirical models for the adjustment parameters, β , α_0 , and α_1 , which would improve the model's ability to produce realistic profiles with only f_oF2 and h_mF2 .

Another possible problem area is the assumption that only O^+ and H^+ are present in the ionosphere. While this may have only a small effect on TEC or $N_e(840)$ calculated from the model, it could have a serious effect on the procedure for calculating h_T from the SSIES data set. The procedure assumes that the light ion density calculated from the ion RPA analysis is H^+ , an assumption that may not always be valid. If the density were actually that for He^+ , the estimate for h_T would be too low. Figure 9 illustrates the variation of TEC and $N_e(840)$ as functions of h_T for the same conditions as those used in generating Figure 5 for various values of y_t . As can be seen, the effect of an error in h_T on TEC and $N_e(840)$ is very small unless h_T is below about 1000km. If h_T is below 1000km, which occurs during the night at mid-latitudes and during the day at mid-latitudes during solar minimum winter solstice conditions (see Figure 9), an error of ± 100 km in h_T will result in roughly a $\pm 7\%$ error in TEC and $\pm 12\%$ error in $N_e(840)$. Note, however, that if the data are available to calculate h_T , then a value for $N_e(840)$ is also available. By adjusting the profile to fit $N_e(840)$, the error in TEC introduced by an error in h_T should be reduced to a few percent or less.

A third assumption made in developing the DE model is that the magnetic field lines are nearly vertical, an assumption which is reasonably valid to

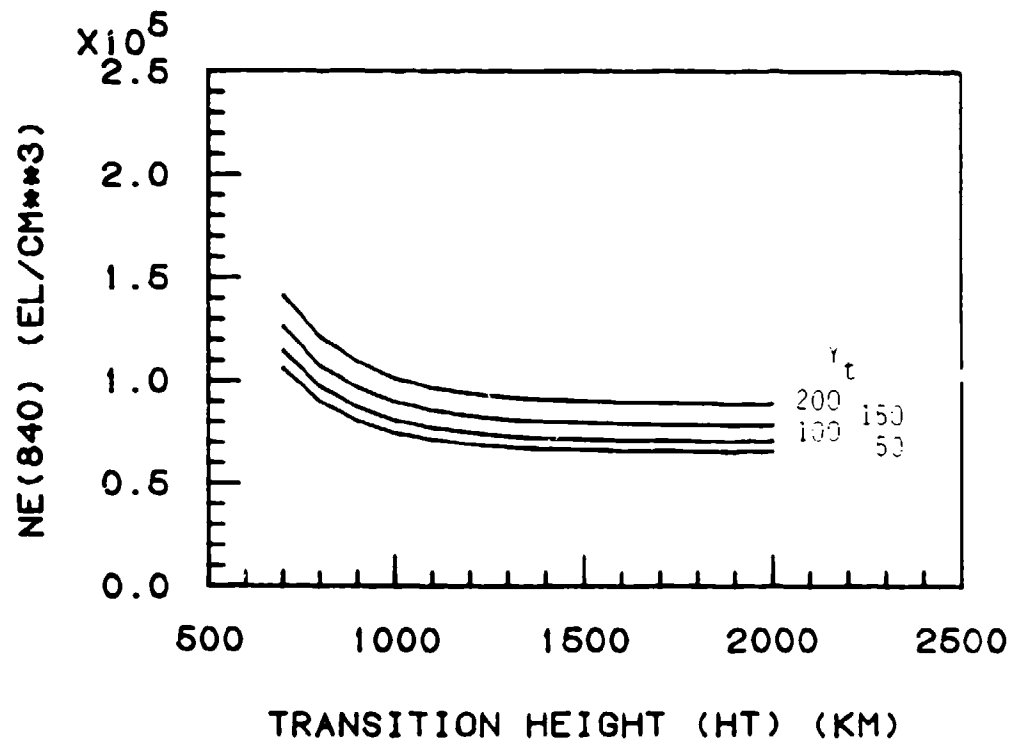
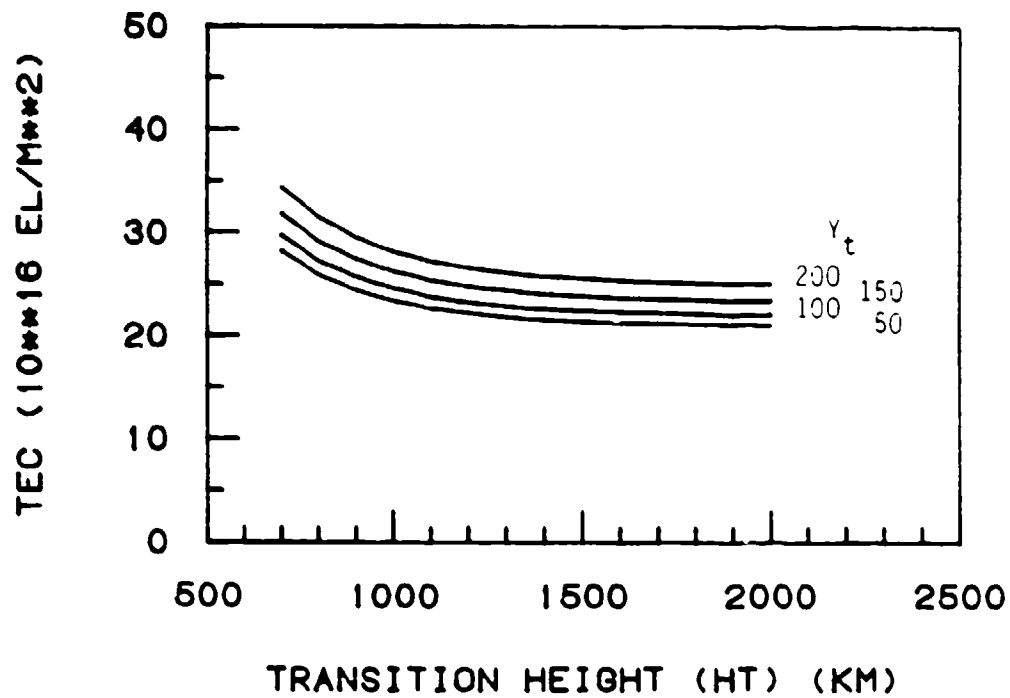


Figure 9. Variation of TEC and $N_e(840)$ as functions of the O^+H^+ transition height for four values of γ_t .

within roughly $\pm 30^\circ$ of the dip equator. This is implied in writing Equation 1 as integral in height rather than in distance along the magnetic field. In the equatorial region, the breakdown in this assumption will have two effects on the profile generated by this model. First, the profile shape produced by the model will not include distortions caused by the non-vertical field lines, an effect which may be somewhat alleviated by the use of an empirical model for the O^+/H^+ transition height. Second, the f_oF2 and h_mF2 used in constructing the profile should not necessarily be values vertically below a given point in the profile, but rather values more representative of conditions in the F2 region at the base of the field line passing through the point. While not conceptually a problem, constructing large numbers of vertical profiles based on latitudinal variations in the F2 region could be computationally burdensome.

Finally, although the data-fitting techniques described in Section 3.2.1.2 appeared to be fairly robust during the limited testing conducted, a full series of tests to determine which parameters to adjust under which conditions should be run when reliable data become available from the SSIES sensor.

3.2.2 Transition Height Model

A global model of the O^+ to H^+ transition height was developed from published analyses of topside sounder data and *in situ* retarding potential analyzer (RPA) data. Titheridge¹³ analyzed topside sounding data from the Alouette I satellite to determine the transition height variation during solar minimum (1964-1965) and a limited amount of data from the ISIS 1 and ISIS 2 satellites near solar maximum (1969 and 1971). Kutiev et al^{17,18} analyzed RPA data from the OGO-6 satellite to determine the (nighttime) variation of h_T during solar maximum (1969-1970). (It should be noted that Kutiev et al¹⁸ have proposed the use of the transition height as an improvement to the IRI79 model.) The latitudinal, seasonal, local time, and solar epoch variations in the h_T model were derived from these references. The location of the plasmapause and its variation with local time and magnetic activity were derived from a further analysis of the Alouette h_T data by Titheridge¹⁹ and work by Spiro reported in Moffett and Quegan²⁰.

The functional form of the model is as follows:

$$h_T = h_m + (h_e - h_m) \exp \left[- \left(\frac{\lambda}{W_e} \right)^2 \right] + \frac{(h_p - h_m)}{2} \left[1 + \operatorname{erf} \left(\frac{\lambda - \lambda_0}{W_p} \right) \right] \quad (19)$$

where h_e , h_m , and h_p are the equatorial ($\lambda=0^\circ$), mid-latitude, and polar values of h_T which are functions of local time, season, and solar epoch; λ is the magnetic (F-layer apex) latitude; and W_e and W_p are feature widths. The second and third terms in the left-hand side of Equation 19 model a nighttime equatorial peak in the latitudinal variation of h_T and the transition into the polar cap ionosphere, respectively.

The local time (LT) variation of h_e , h_m , and h_p is modeled using the epstein step function used to model local time variations in the IRI79 model. The form of this variation is

$$f(LT) = f_N + (f_D - f_N) \left\{ \frac{1}{1 + \exp[-(LT - LT_{SR})]} - \frac{1}{1 + \exp[-(LT - LT_{SS})]} \right\} \quad (20)$$

where f_N and f_D are the night and day values of the function, and LT_{SR} and LT_{SS} are the local times of sunrise and sunset.

The seasonal variation of h_e , h_m , and h_p is modeled by a simple cosine variation of the form

$$f(\text{day}) = (f_w + f_s) \pm (f_w - f_s) \cos \left[\frac{2\pi}{365} (D - 10) \right]$$

where f_w and f_s are the winter and summer values of the function, and D is the day of the year. The plus (minus) sign in this equation is used for the northern (southern) hemisphere.

The solar epoch variation of h_e , h_m , and h_p is modeled as a linear variation with the 10.7 cm solar radio flux ($F_{10.7}$) of the form

$$h_i = h_{i0} + a_i \left(\frac{S - 75}{85} \right) \quad (21)$$

where $S = 75$ if $F10.7 < 75$, $S = F10.7$ if $75 < F10.7 < 180$, and $S = 180$ if $F10.7 > 180$. Table 3 shows the values of h_{i0} and a_i for the three latitudinal regimes (equatorial, mid, and polar) for day and night, summer and winter. There are no day values for the equatorial regime, as the equatorial peak is present only at night.

The nighttime equatorial peak term in Equation 19 is included to model a peak present in the Alouette data (c.f. Figure 7 in Titheridge¹³) and to fit the variations presented in Kutiev et al¹⁸. It is modeled as a gaussian in latitude centered on the magnetic (dip) equator with a half-width of 10° .

The transition through the plasmapause, the third term in Equation 19, is modeled through variations in two latitude boundaries: the equatorward boundary of the plasmapause transition region, λ_1 , and the center of the light-ion trough, λ_3 . The transition is modeled as an error function centered on $\lambda_2 = (\lambda_3 - \lambda_1)/2$ with a transition width, $W_a = \lambda_2/2$. The λ_1 boundary varies only with local time using Equation 20 with $f_D = 30^\circ$, $f_N = 50^\circ$, $LT_{SR} = 9$, $LT_{SS} = 20$. This variation was chosen to fit the variation shown in Figure 5 of Titheridge¹⁹. The λ_3 boundary varies with local time and magnetic activity (K_p) as

$$\lambda_3 = (63.0 - 1.4K_p) + (3.0 + 0.1K_p) \cos\left(\frac{2\pi}{24} t\right)$$

where

$$\begin{aligned} t &= 0 && \text{for } 0^h < LT < 6^h \\ &= 2(LT-6) && \text{for } 6^h < LT < 12^h \\ &= LT && \text{for } 12^h < LT < 24^h. \end{aligned}$$

This equation reflects variations with K_p as reported by Titheridge¹⁹, and local time variation as described by Moffett and Quegan²⁰ and shown in their Figure 10.

A listing of the Fortran function that implements this model is given in Appendix B.

Table 3. Constants for use in Equation 21 describing the variation of h_T with solar epoch.

a. h_{i0}

<u>Regime</u>	Day		Night	
	<u>Summer</u>	<u>Winter</u>	<u>Summer</u>	<u>Winter</u>
Polar	1200	1200	1100	900
Mid	900	600	600	450
Equatorial	-	-	800	800

b. a_i

<u>Regime</u>	Day		Night	
	<u>Summer</u>	<u>Winter</u>	<u>Summer</u>	<u>Winter</u>
Polar	450	450	550	750
Mid	600	700	300	200
Equatorial	-	-	300	300

Figures 10-12 illustrate the seasonal, solar epoch, and magnetic variations in h_T produced by this model. In Figure 10, the latitudinal variation of h_T at noon and midnight are shown for the June and December solstices and for an equinox for $F_{10.7} = 100$ janskys and $K_p = 3^{\circ}$. In Figure 11, the variation with $F_{10.7}$ is shown for noon and midnight at the June solstice, $K_p = 3^{\circ}$. The variation with K_p is shown in Figure 12 for noon and midnight at the June solstice, $F_{10.7} = 100$ janskys.

The primary weaknesses in this model are in the solar epoch variability and at high latitudes. Only a small amount of data was available at solar maximum, and most of it was nighttime data. It may be possible to refine this variation when data from the SSIES RPA sensor becomes available. At high latitudes, the model provides, at best, only a rough estimate of the location of the sharp transition from mid-latitude to polar transition heights, and detailed structures such as the effect of the dayside cusp (c.f. Figure 7 in Titheridge¹³) are not included in the model due to a lack of data. Again, this section of the model could be refined using SSIES RPA data.

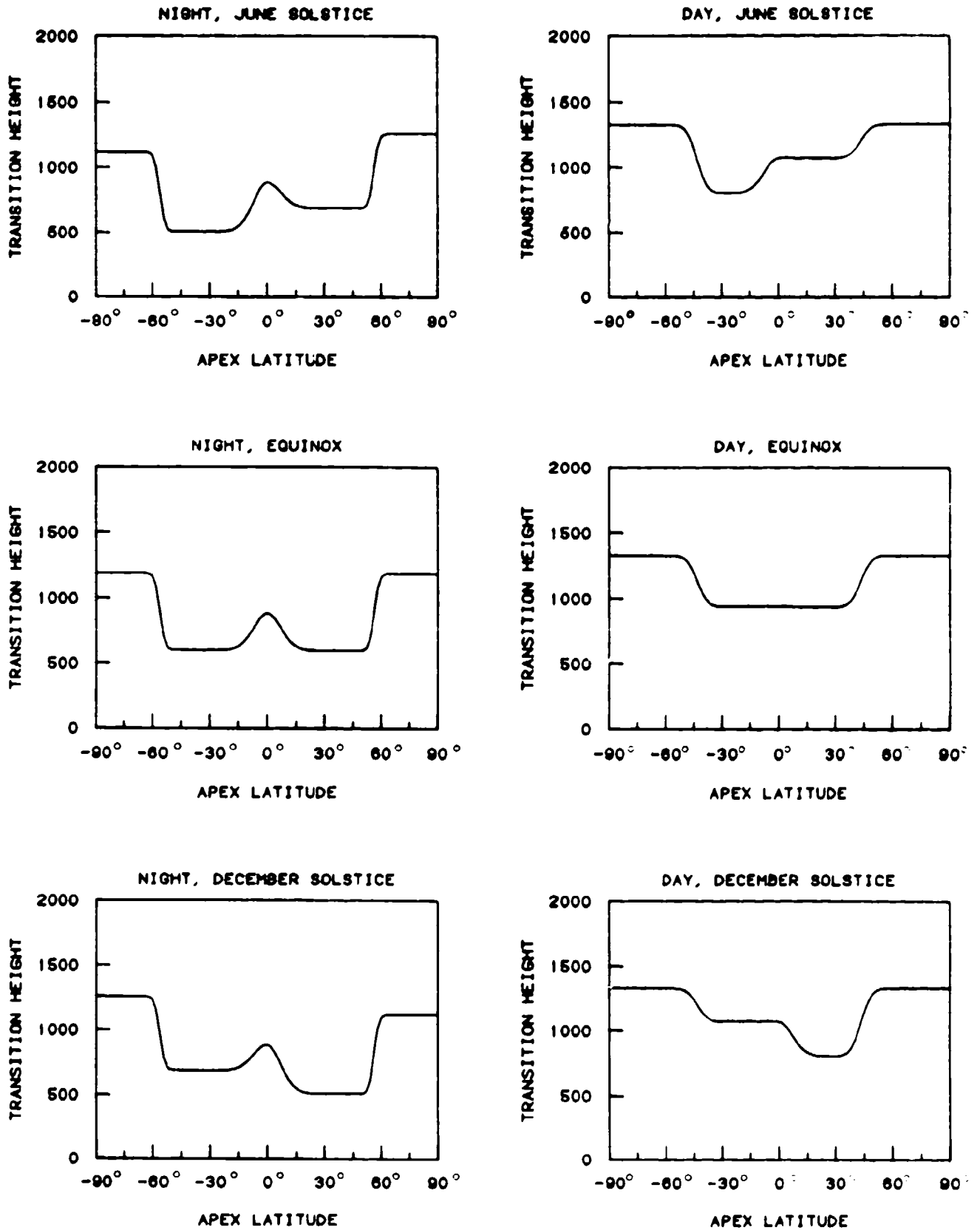


Figure 10. Seasonal variation in the h_T model for $F_{10.7}=100$, $K_p=3^+$.

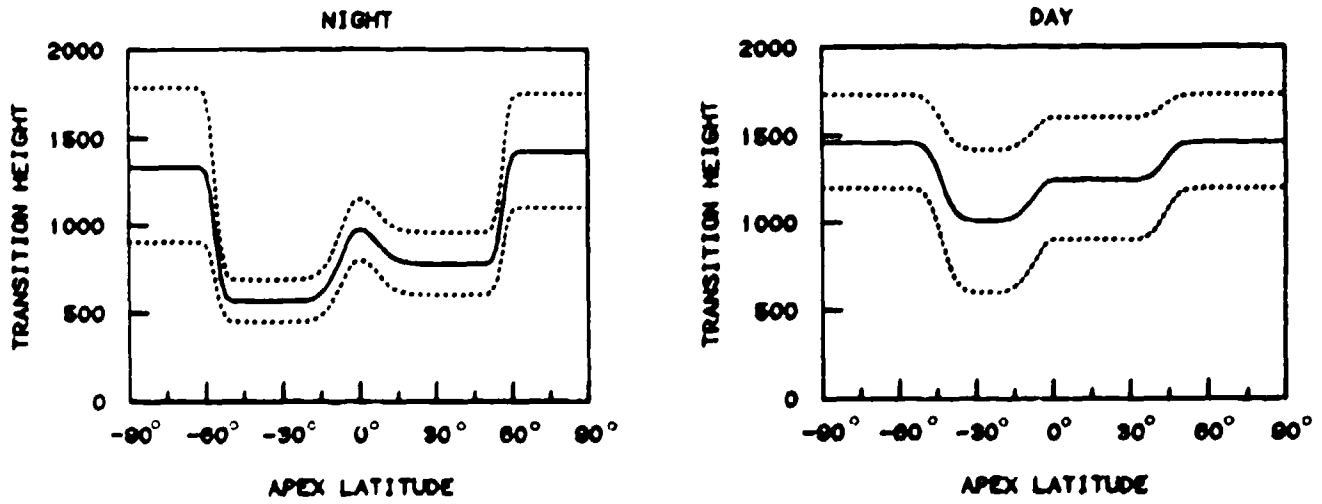


Figure 11. F10.7 variation in the h_T model for June solstice, $K_p=3_0$. The solid curves are for F10.7=125, the upper dashed curves are for F10.7=175, and the lower dashed curves are for F10.7=75.

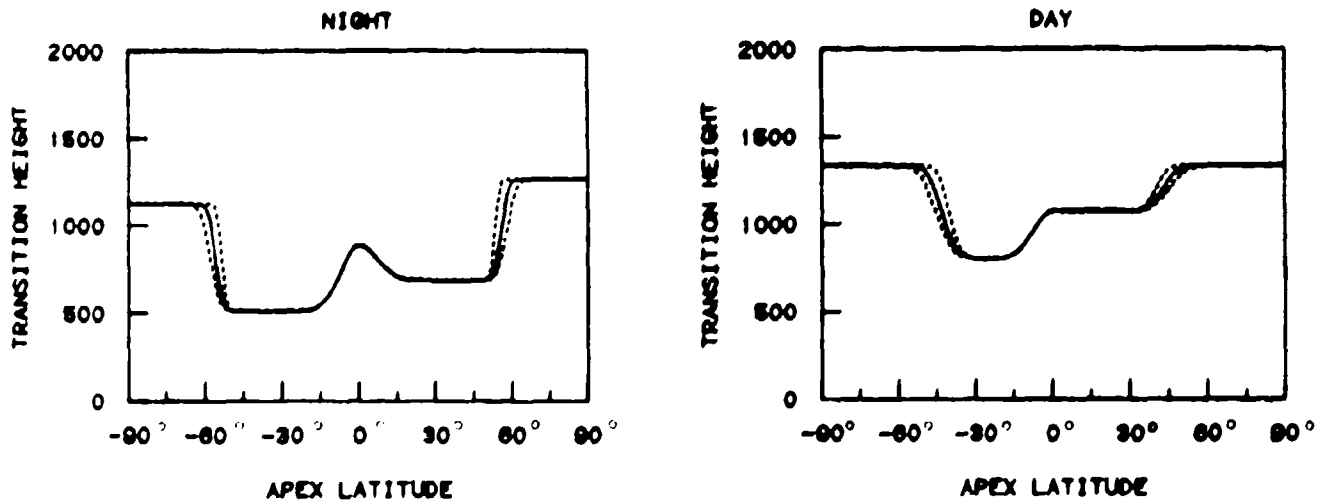


Figure 12. K_p variation in the h_T model for June solstice, F10.7=100. The solid curves are for $K_p=3_+$, the upper dashed curves are for $K_p=7_0$, and the lower dashed curves are for $K_p=1_0$.

4. IONOSPHERIC DATA PREPROCESSORS STUDY

Limited investigations into analysis stability problems with the 4D model led to the development of front-end data preprocessors for f_oF_2 and TEC data by AFGWC/TSIS²¹. These preprocessors use simple curve-fitting techniques to generate equally spaced grids of f_oF_2 and TEC values from data available in the Astrogeophysical Data Base (AGDB)²². In the contract prior to the current one, a 4D model preprocessor system²¹ was designed around these two preprocessors, programs FORIER (f_oF_2 data) and POLY1 (TEC data), and a third preprocessor for SSIE $N_e(840)$ data, program SSIELD⁵, provided by another contractor.

This system, tested and installed at AFGWC, was to be the starting point for the tasks under this study area. Unfortunately, as of the start of this phase of the project, the SSIELD program was still not operational at AFGWC, and was neither sufficiently tested nor adequately documented to be of any use. Thus, this study area was begun by assisting AFGL/PHG with an assessment of the SSIELD program.

The assessment, documented in Scientific Report No. 1⁹, showed that the SSIELD program was not working correctly and, as currently designed, would be inadequate for the task even if the problems in the program were corrected. The assessment results were discussed with Dr. Frederick Rich (AFGL/PHG) and Mr. Bob Bussey (AWS/SDDE), and it was decided to redirect the efforts in this study area to identifying and investigating alternative analysis techniques for producing gridded fields of SSIE $N_e(840)$ data.

Toward this end, informal discussions were held with Dr. Rich and Mr. Bussey to determine the requirements to be met by the SSIELD program. A distillation of these discussions provided the following list of requirements and desired attributes:

1. The program must be documented and tested in accordance with DoD Standard 7935, dated 15 Feb 1983²³, and with the AFGWC software standards²⁴.
2. The program must be coded in ANSI Standard X3.9-1978, as implemented in the UNIVAC ASCII FORTRAN.

3. Any internal model of $N_e(840)$ used should be a continuous function of latitude, longitude, time, season (day-of-year), and sunspot number (solar epoch).

4. Ideally, any internal $N_e(840)$ model should be based on satellite observations. Provisions for updating this model should be included.

5. Data from the SSIE sensor should be fetched from a user-defined section of the Astrogeophysical Data Base (AGDB).

6. Provisions for future incorporation of TEC data, from either the AGDB or from a TEC data preprocessor, should be included.

7. The analysis algorithm should use all data available and be able to process data from both northern and southern hemispheres.

8. If no data are available for a particular program run, the analysis should default to the internal model.

9. The analysis should incorporate a "memory" capability; i.e., the analysis field from a previous run could be used as the starting point for the current run.

10. The final analysis field should not contain distinct features (bull's-eyes or ridges) at points where data are available.

11. The locations of the grid points for the output grids should be defined such that they may be easily changed.

Although this is not an officially approved statement of requirements, it provides a starting point for an investigation of alternative analysis methods for an SSIE $N_e(840)$ data preprocessor.

4.1 Task 4: $N_e(840)$ Data Preprocessor Improvements

The starting point for this study was a general review of various analysis methods developed for use in other ionospheric applications, in particular, those developed in constructing the ITS78 model ionosphere^{25,26}, those used in AFGWC program UKFILE for updating the ITS78 coefficients¹¹, and the global analysis method used in the 4D model⁷. From this review, and the requirements listed earlier, the following general design was developed for

an improved SSIELD program:

1. The core of the program would be a spectral model of $N_e(840)$ which would include continuous variability with location, time, season, and solar epoch. The format of this model would be similar to the ITS78 f_oF_2 and M3000 spectral models²⁵.

2. Input SSIE $N_e(840)$ data would be used to modify the coefficients of this model in two stages:

a. All mid-latitude data would be used to adjust the model through derivation of an effective 10.7 cm solar flux (F10) defined as the F10 value which, when used by the $N_e(840)$ model, minimizes the mean difference between the model and the observations. A similar method for adjusting the ITS78 f_oF_2 coefficients has been used at AFGWC for several years²⁷.

b. All data would be used to modify the coefficients resulting from the effective F10 analysis, or from a previous analysis, using a spectral data assimilation method developed by Flattery²⁸ and used in the global analysis section of the 4D model⁷.

3. The required UT grids would be generated from either the base $N_e(840)$ model, the results of the effective F10 analysis, the results of the global analysis, or from the results of some previous analysis, at the discretion of the user.

Investigation of this design would be accomplished in four phases:

1. Define the form of the spectral $N_e(840)$ model. This would include selection of coordinate system, functions to be used in the spectral expansion, truncation limits on the spectral expansion, and selection of an initial model of $N_e(840)$ on which to base the spectral model. The final step of this phase would be the generation of coefficients for the spectral $N_e(840)$ model.

2. Develop the effective F10 analysis technique. The starting point for this phase would be the AFGWC UKFILE program¹¹.

3. Develop the global assimilation technique. The starting point for this phase would be the global analysis section of the 4D model⁷.

4. Test the full analysis program on both model and "real-world" inputs.

4.1.1 Spectral $N_e(840)$ Model

As described in Scientific Report No. 1, the functional form of the spectral $N_e(840)$ model is

$$f_p(\lambda, \phi, t, F, D; 840) = \sum_{\ell=1}^L \sum_{m=1}^M \sum_{n=\frac{m}{2}}^N Y_{\ell}^{mn}(F, D) T_{\ell}(t) T_m(\phi) P_n^{m/2}(\sin \lambda) \quad (22)$$

$$Y_{\ell}^{mn}(F, D) = \sum_{r=0}^R a_{r\ell}^{i mn}(d) F^r \quad (23)$$

$$a_{r\ell}^{i mn}(D) = \sum_{i=0}^I a_{ri}^{i mn} T_i(D) \quad (24)$$

where f_p is the plasma frequency at 840 km in MHz; λ and ϕ are the F-layer apex latitude and longitude; t is Greenwich Mean Time (UT); F is the 10.7 cm solar radio flux; D is the day of the year; $P_n^{m/2}(\sin \lambda)$ are the associated Legendre functions of degree n and order $\frac{m}{2}$; $a_{ri}^{i mn}$ are the model coefficients; and $T_{\ell}(t)$, $T_m(\phi)$, and $T_i(D)$ are orthonormal trigonometric functions given by

$$T_0(x) = \frac{1}{\sqrt{2\pi}},$$

$$T_{2j-1}(x) = \frac{1}{\sqrt{\pi}} \cos jx,$$

$$T_{2j}(x) = \frac{1}{\sqrt{\pi}} \sin jx.$$

The truncation limits for the series in Equations 22, 23, and 24 are $L=13$, $M=21$, $N=20-\frac{m}{2}$, $R=2$, and $I=8$. The plasma frequency from Equation 22 is converted to $N_e(840)$ by

$$N_e(840) = 1.24 \times 10^4 f_p^2 \text{ e1/cm}^3. \quad (25)$$

Two complete sets of model coefficients, a_{ri}^{cnn} , have been generated - one using the DHR profile model and one using the Bent profile model. Both were generated using the same $f_0 F_2$ and M3000 values from the ITS78 model using the procedures described in Section 4.2.1 of Scientific Report No. 1, with one modification. It was discovered that values of f_p near the pole showed a drop similar to that found in the SSIELD model, even with data values at $\pm 80^\circ$ latitude. This was corrected by changing the latitudinal spacing from every 10° to a spacing defined by $\sin \lambda_{gi} = x_i$, $i=1,24$, where the x_i are the gaussian quadrature points on the interval -1 to +1. The DHR model coefficients are used in the analysis program; the Bent model coefficients were generated for use in constructing data sets for testing the analysis program. The differences between these two models is illustrated in Figure 13, which shows the northern geographic hemisphere fields of $N_e(840)$ for a sunspot number of 120 ($F_{10.7}=164$ janskys), Day 199 (18 July), as generated from Equations 22-24 from the DHR (upper) and Bent (lower) coefficients. The Bent coefficient set was generated when it was discovered that test data constructed using the DHR coefficients were fit exactly in the effective F10 analysis, leaving no residual error to be fit in the global assimilation.

4.1.2. Effective F10 Analysis

The objective of the effective F10 analysis is to find the F10 value which, when used in Equation 22, provides an analysis field which has a zero mean error with respect to the input data, i.e., $\overline{\Delta f_p} = 0$. This value for F10 is denoted the effective F10, or EF10, for the analysis. The method used is an iterative one, the secant method, in which subsequent estimates of EF10 are calculated from

$$EF10 = EF10^o - \overline{\Delta f_p^o} \left(\frac{EF10^o - EF10^-}{\overline{\Delta f_p^o} - \overline{\Delta f_p^-}} \right) \quad (26)$$

where the superscripts o and - denote the values from the previous two iterations and $\overline{\Delta f_p}$ is the mean error between the input data and the field as specified using the EF10 for that iteration. Once started, this method converges very rapidly; however, it requires an initial and one subsequent estimate for EF10 to start.

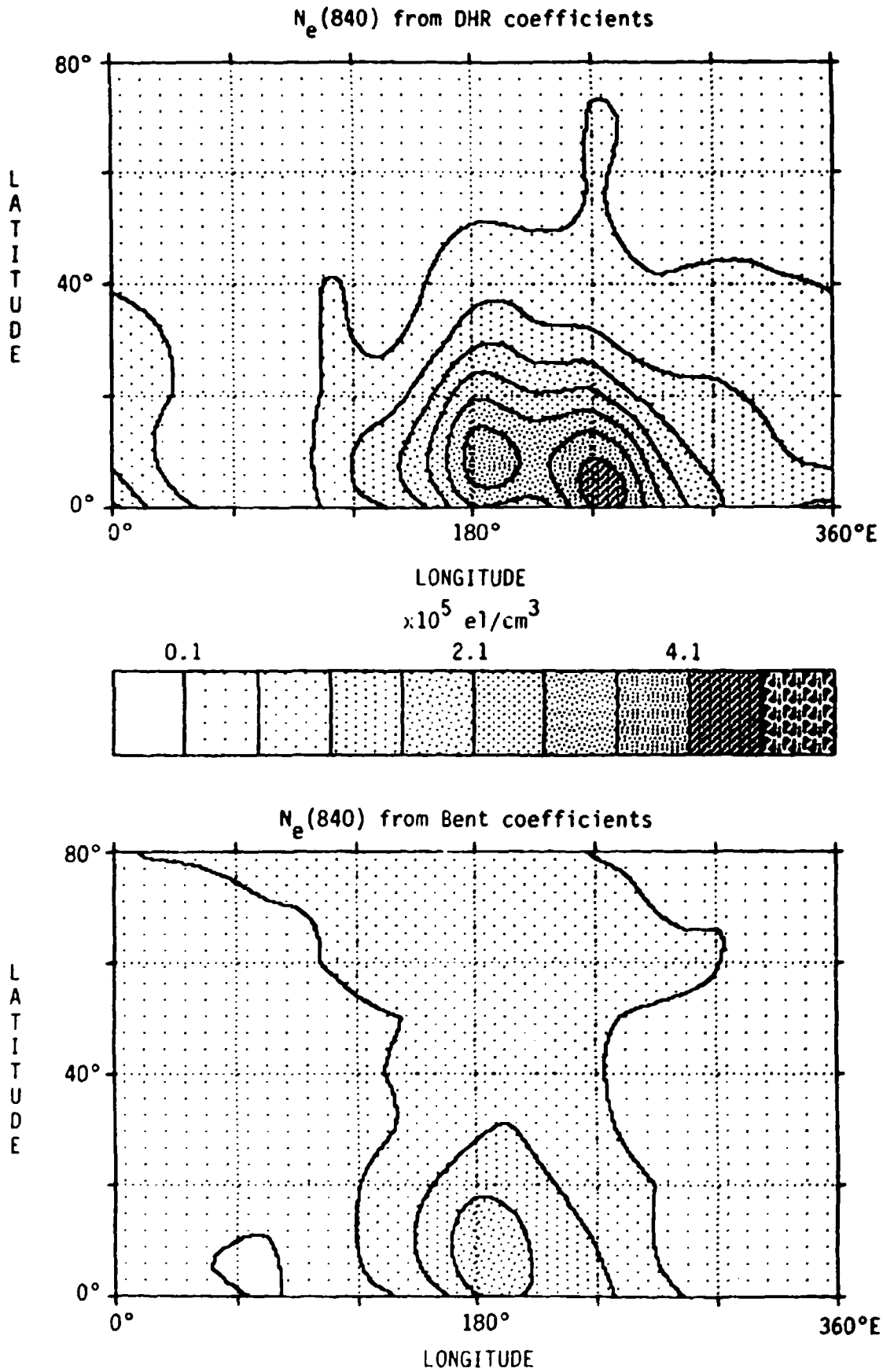


Figure 13. Northern geographic hemisphere fields of $N_e(840)$ from the DHR (upper panel) and Bent (lower panel) model coefficients for a sunspot number of 120.

The initial estimate for EF10 is calculated by taking advantage of the form of the model for $f_p(840)$ given in Equation 22. The mean value for f_p , averaged over all λ , δ , and t , is given by

$$f_p = \frac{\gamma_1^{11}}{2\pi\sqrt{2}} \quad (27)$$

Assuming that the input data are evenly distributed in t , δ , and λ , the mean of the input data, \bar{f}_p , can be used to estimate γ_1^{11} by

$$\gamma_e = 2\pi\sqrt{2}\bar{f}_p$$

From Equation 23, γ_1^{11} varies with F10 as

$$\gamma_1^{11} = \beta_0 + \beta_1 F10 + \beta_2 F10^2 \quad (28)$$

where the superscripts have been dropped on β . The first estimate for EF10 is then defined as the value of F10 which produces $\gamma_1^{11} = \gamma_e$ using Equation 28. This leads to the solution

$$EF10 = - \left(\frac{\beta_1}{2\beta_2} \right) + \sqrt{\left(\frac{\beta_1}{2\beta_2} \right)^2 + \left(\frac{\gamma_e - \beta_0}{\beta_2} \right)} \quad (29)$$

As the input data are not, as a rule, evenly spaced, the EF10 value calculated from Equation 29 does not necessarily produce the desired result of $\bar{f}_p = 0$. Therefore, further estimates are required.

The second estimate for EF10 is made using the Newton form of Equation 26. In this method, the second estimate is given by

$$EF10^+ = EF10^o - \frac{\bar{\Delta f}_p^o}{\left(\frac{\partial \bar{\Delta f}_p}{\partial F10} \right)} \quad (30)$$

in which the derivative of $\bar{\Delta f}_p$ with respect to F10 is required. Since the input f_p values do not vary with F10, an estimate for this derivative can be obtained from Equations 27 and 28 yielding

$$\frac{\partial \bar{\Delta f}_p}{\partial F10} \approx \frac{\partial f_p}{\partial F10} = \frac{\sqrt{2}}{4\pi} (\beta_1 + 2F10 \beta_2)$$

so Equation 30 becomes

$$EF10^{\dagger} = EF10^{\circ} - \frac{2\sqrt{2} \overline{\Delta f_p^{\circ}}}{\left(\beta_1 + 2 EF10^{\circ} \beta_2 \right)} \quad (31)$$

As with Equation 29, this will provide only a next-best estimate for EF10, as it also uses the assumption that the data are uniformly distributed in space and time, and further iteration using Equation 26 may be required. In actual testing (see Section 4.1.5), the second estimate was within the stop criterion of $\overline{\Delta f_p} < 0.005\text{MHz}$ in 9 of 12 cases, and only one further iteration was required in the remaining 3 cases.

The effective F10 analysis may also be run using a set of γ_{ℓ}^{mn} coefficients produced by a previous analysis. Equation 24 can be rewritten

$$S_0^{mn} = \gamma_{\ell}^{mn} - \left(\beta_1^{mn} F10 + \beta_2^{mn} F10^2 \right)$$

By using the γ_{ℓ}^{mn} and EF10 values from a previous analysis in this equation, the S_0^{mn} coefficients are reset, and the effective F10 analysis can then be done using the updated set of β_r^{mn} coefficients.

4.1.3. Global Analysis

The global analysis technique is identical to that employed by the AWS 4D ionospheric analysis model⁶. This technique, developed initially for meteorological applications²⁸, modifies the coefficients of a spectral representation of a field such that the new coefficients produce a field that fits input data where data are available and merges smoothly into the original field away from the data points. In this analysis, the γ_{ℓ}^{mn} coefficients of Equation 22 are iteratively updated using

$$\gamma_{\ell}^{mn'} = \gamma_{\ell}^{mn} + W \sum_{j=1}^J A_{\ell}^{mn}(\lambda_j, \lambda_j, t_j) \Delta f_p(\lambda_j, \lambda_j, t_j) \cos \lambda_j \quad (32)$$

$$A_{\ell}^{mn}(\lambda_j, \lambda_j, t_j) = T_{\ell}(t_j) T_m(\lambda_j) P_n^{m/2}(\sin \lambda_j)$$

where J is the number of data points, $\Delta f_p(\lambda_j, \phi_j, t_j)$ is the difference between the input f_p and f_p calculated using the γ_p^{mn} coefficients in Equation 22 at the j th data point, and W is a weight factor given by

$$W = w_c \Delta\lambda \Delta\phi \Delta t$$

where w_c is a convergence control parameter and $\Delta\lambda$, $\Delta\phi$, Δt define the latitude, longitude, and time spacing of the fictitious grid over which the analysis is defined⁶. The iteration continues, until a desired RMS difference between the data and the analysis RMS difference and begins to diverge.

In order to control the introduction of spurious small-scale features into the analysis, the analysis is designed to begin the iterative update on the lower-order coefficients only. This is done by using values for L and M in Equation 22 lower than the maximum used in the model (currently 13 and 21), and increasing these values with each iteration until the maximum truncation limits are reached. By starting the analysis without the higher-order terms in the expansion, the difference between the data and the initial field will be reduced first through modification of the larger scale features of the field, and only the residual differences will go into smaller-scale features. Initially, it was planned to reduce only the longitude (M) and time (L) truncation limits, and this is what was used in the developmental testing described in Section 4.1.4. However, during the study of using $N_e(840)$ values derived from TEC data, described in Section 4.2, it was decided to allow the latitude (N) truncation limit such that the value of N at $m=1$ was $N=M-1$, thus preserving the modified triangular truncation scheme.

4.1.4 Preprocessor Program (GRIDNE) Description

The analysis procedures described in Sections 4.1.2 and 4.1.3 were implemented in a test version of an $N_e(840)$ data preprocessor (program GRIDNE) designed and coded to meet the requirements worked out with AFGWC/SDDE and AFGL/PHG. Figure 14 is an organization chart for program GRIDNE which illustrates the internal linkages and relationships between the various routines which make up the program. A short description of the function of each of the routines listed in Figure 14 is presented in Table 4, and a complete listing of all non-AFGWC routines is included in Appendix C.

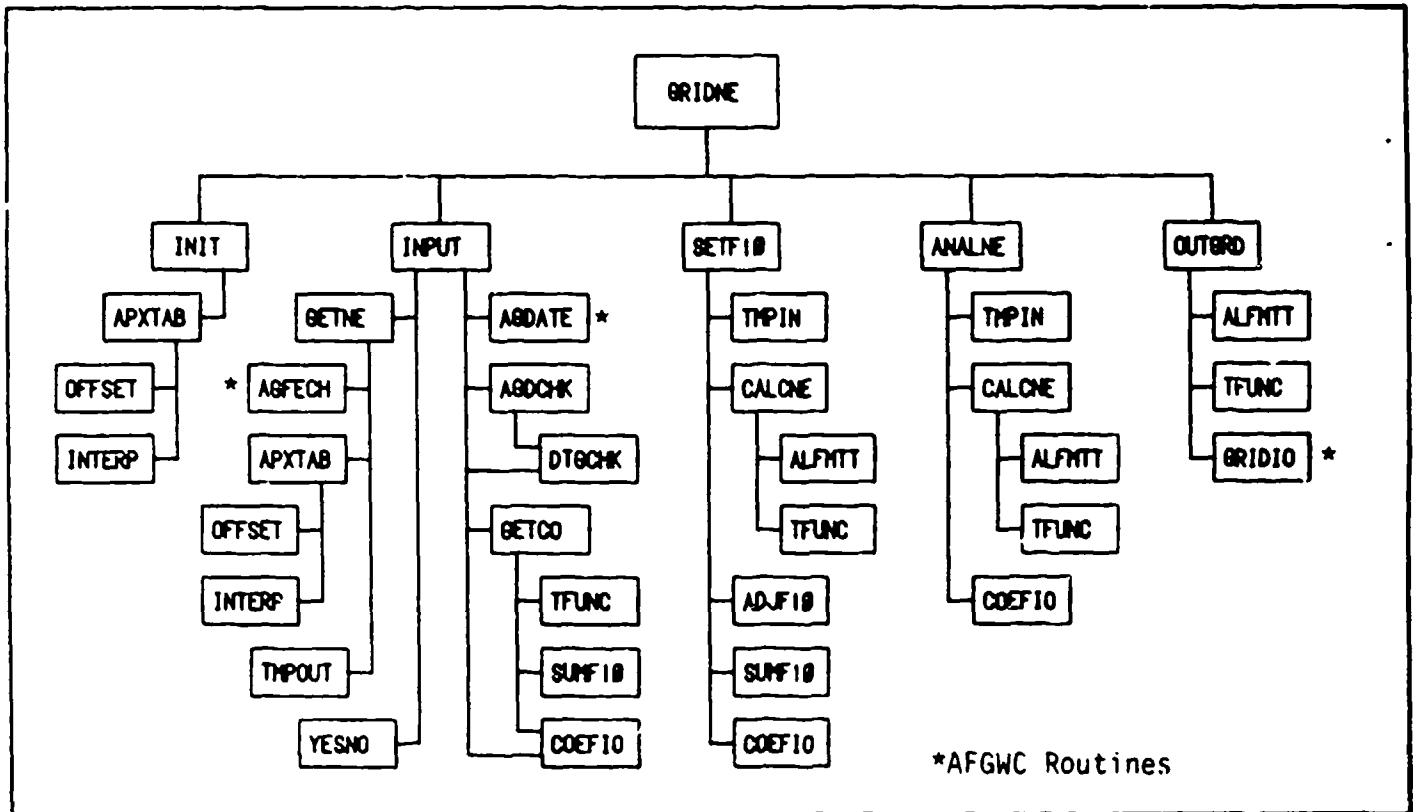


Figure 14. Program GRIDNE Structure Chart.

Table 4. Description of program GRIDNE routines.

- ADJF10 - Calculate the next estimate of the effective F10 using the secant iteration method (implements Equation 26).
- *AGFECH - Fetch SSIE data records from the AFGWC Astrogeophysical Data Base (AGDB).
- *AGDATE - Determine the active dates and julian hours on the AGDB.
- AGDCHK - Determine if an input date and time is active on the AGDB.
- ALFMTT - Calculate the associated Legendre functions for a modified triangle truncation scheme.
- ANALNE - Perform the global analysis (implements Equation 32).
- APXTAB - Calculate the F-layer apex coordinates of an input geographic latitude and longitude.

Table 4. (Continued)

- CALCNE - Calculate a value for $f_o(840)$ and $N_e(840)$ for a given time and location (implements Equation 22).
- COEF10 - Input or output a set of γ_{ξ}^{mn} coefficients for Equation 22.
- DTGCHK - Error check a user-input date and time.
- GETCO - Input the $\alpha_{r_i}^{2mn}$ coefficients for Equation 24 and sum over the date (implements Equation 24).
- GETNE - Fetch SSIE data records from the AGDB, error check the records, and store them on a temporary file.
- *GRIDIO - Write $N_e(840)$ grid sets to file FOURDGRIDS.
- GRIDNE - Main driver routine.
- INIT - Initialize all variables requiring initialization and load the array which defines the FOURDGRIDS output grid.
- INPUT - Interact with the user for all required user inputs, fetch SSIE data from the AGDB and prepare the data for analysis if necessary, and fetch the necessary coefficient sets.
- INTERP - Interpolate in the F-layer apex coordinate look-up table.
- OFFSET - Calculate the offset dipole coordinates of a geographic location.
- OUTGRD - Build and output $N_e(840)$ grids to file FOURDGRIDS.
- SETF10 - Perform the effective F10 analysis (implements Equation 29).
- SUMF10 - Sum the β_r^{0mn} coefficients over F10 (implements Equation 23).
- TFUNC - Calculate the orthonormal trigonometric series.
- TMPIN - Input SSIE $N_e(840)$ records from a temporary file.
- TMPOUT - Output SSIE $N_e(840)$ records to a temporary file.
- YESNO - Query the user for a yes/no answer.

*AFGWC Routines

In tests at AFGWC on a SPERRY 11/82 computer, the program size was determined to be roughly 55K words, and the CPU time required for an analysis run can be estimated by the algorithms

$$\text{CPU}_1 = 3.8 n_F + 12.7 n_G - 0.5 \text{ seconds}$$

for processing data from one satellite for a 24-hour period (1351 data points) and

$$\text{CPU}_2 = 7.1 n_F + 23.8 n_G - 8.0 \text{ seconds}$$

for data from two satellites, where n_F is the number of iterations required to determine the effective F10 value and n_G is the number of iterations in the global analysis. From the tests conducted, it appears that nominal values for n_F and n_G are 2 and 6, respectively, for a two-satellite CPU time of roughly 150 seconds. Worst-case values were $n_F = 3$ and $n_G = 10$ for a two-satellite CPU time of roughly 250 seconds.

Inputs from the user are as follows:

- a. Date (YYMMDD) and sunspot number for the analysis.
- b. The maximum number of iterations for the effective F10 analysis, and the value of the average Δf_p at which to stop the analysis.
- c. The maximum number of iterations for the global analysis; the value of the RMS Δf_p at which to stop the analysis; the initial truncation limits to be used for L and M in Equations 22 and 32; the spacing of the latitude, longitude, time grid over which Equation 32 is defined; and the value for the convergence control parameter, W_c .
- d. Various program control parameters specifying the source of the data to be analyzed, the coefficients to use in defining the initial analysis field, which analyses to run, and what items to output.

The program uses two disk storage files, NE840FILE and NETEMPFIL. File NE840FILE, roughly 103K-words in size, contains the F-layer apex coordinate look-up table (8190 words), the γ_{ri}^{mn} coefficients which define the $N_e(840)$ model (77,571 words), five sets of γ^{mn} coefficients from previous analyses (2873 words/set, 14,365 words total), and six 28-word file control sectors. Subroutine APXTAB reads in the apex coordinate table, subroutine GETCO reads

in the α_{ri}^{lmn} coefficients, and subroutine COEFIO reads and writes the α_{ri}^{lmn} coefficients sets. File NETEMPFIL is a temporary file used for external storage of the $N_e(840)$ data to be analyzed. Subroutine GETNE strips the $N_e(840)$ data from SSIE AGDB records and builds this file via subroutine TMPOUT. Subroutines SETF10 and ANALNE read the $N_e(840)$ data from the file via function TMPIN.

4.1.5 Preprocessor Program Tests

Tests designed to determine the capabilities and limitations of the GRIDNE program were run at AFGWC during the period 10-14 September 1984. A total of three tests were conducted:

- a. Test 1 - Test the overall capabilities and limitations of the analysis methods for a range of sunspot numbers.
- b. Test 2 - Test the effects of varying the convergence control parameter, W_c .
- c. Test 3 - Test the effects of using various initial truncation limits for M and L in Equations 22 and 32.

The input parameters used in the tests are listed in Table 5.

4.1.5.1 Description of Test Data and Procedures

All tests were run using $N_e(840)$ data generated by using the Bent α_{ri}^{lmn} coefficients in Equations 22-25. Two sets of data were generated for each test, one to be used as input to program GRIDNE and one to be used to determine how well the GRIDNE analyses performed. The first set, denoted the satellite data set, consists of simulated SSIE $N_e(840)$ data for a 24-hour period (1351 data points) for one or two DMSP satellites with ascending modes at 0600LT and 1000LT. The second set, denoted the Bent grid set, consists of 24 $N_e(840)$ grids, one grid per UT hour, covering the northern geographic hemisphere from the equator to 80°N latitude in 10° increments and 0° to 345°E longitude in 15° increments. A test-data generating program, ORBTNE, was developed which can generate either data set or both for a given date and sunspot number (SSN).

The test procedures were as follows:

- a. Run test program ORBTNE to generate the satellite and grid data sets for the data and SSN specified in Table 5.

Table 5. Test Parameters

I. Test 1 - Analysis Capabilities

Date: 840911

Initial truncation limits: $M=13$, $L=7$

Grid spacing: 10° latitude, 15° longitude, 1^h time

Convergence control: $w_c=1.0$

Case 1a - SSN=10, 0600LT satellite

Case 1b - SSN=10, 0600LT and 1000LT satellites

Case 1c - SSN=60, 0600LT satellite

Case 1d - SSN=60, 0600LT and 1000LT satellites

Case 1e - SSN=120, 0600LT satellite

Case 1f - SSN=120, 0600LT and 1000LT satellites

II. Test 2 - Convergence Control Parameter Effects

Date: 840911

Initial truncation limits: $M=13$, $L=7$

Grid spacing: 10° latitude, 15° longitude, 1^h time

Data set: SSN=60, 0600LT and 1000LT satellites

Case 2a - $w_c=1.50$

Case 2b - $w_c=1.25$

Case 2c - $w_c=1.10$

Case 2d - $w_c=0.90$

Case 2e - $w_c=0.80$

Case 2f - $w_c=0.50$

III. Test 3 - Truncation Limit Effects

Date: 840911

Grid spacing: 10° latitude, 15° longitude, 1^h time

Convergence control: 1.0

Data set: SSN=60, 0600LT and 1000LT satellites

Case 3a - $M=13$, $L=5$

Case 3b - $M=15$, $L=7$

Case 3c - $M=17$, $L=9$

Case 3d - $M=19$, $L=11$

Case 3e - $M=21$, $L=13$

b. Run program GRIDNE to process the satellite data set. Outputs include goodness-of-fit statistics from both the effective F10 and global analyses, and the γ_i^{mn} coefficients from the initial analysis field (calculated from Equations 23 and 24 using the DHR α_{ri}^{2mn} coefficients and the same date and SSN used by program ORBTNE), the effective F10 field (calculated from Equation 23 using the effective F10 value), and the global analysis field (calculated iteratively from Equation 32).

c. Generate a grid set from each of the three γ_i^{mn} sets output from program GRIDNE. Compare each of these three to the Bent grid set and generate the following comparison statistics:

(1) A grid set which contains the difference between the analysis and Bent grid sets, denoted the $\Delta N_e(840)$ grid set.

(2) The RMS $\Delta N_e(840)$ and RMS percent $\Delta N_e(840)$ for all 24 grids (5184 data points), and as functions of latitude, longitude, UT, and local time.

Figures 15 and 16 are samples of the analysis results which will be presented for the various tests. This particular test was for 18 July with a sunspot number of 120, processing data from two DMSP satellites. In Figure 15, the upper plot shows the variation of RMS $\Delta N_e(840)$ with latitude for the initial analysis field (dotted line), the effective F10 (EF10) field (dashed line), and the global analysis field (solid line). The lower plot in this figure shows the variation of $\Delta N_e(840)$ with local time for all three fields. The vertical dotted lines in this figure indicate the local times of the ascending (0600 and 1000) and descending (1800 and 2200) nodes of the DMSP orbits used in the analysis.

Figure 16 shows contour plots of the 0000UT analysis, $\Delta N_e(840)$, and Bent grids. The three pairs of plots are, from the top down, the initial analysis grid and its $\Delta N_e(840)$ grid, the EF10 analysis grid and its $\Delta N_e(840)$ grid, and the global analysis grid and its $\Delta N_e(840)$ grid. The single plot at the bottom is the Bent grid. Ideally, if the analysis program worked perfectly, the global analysis grid and the Bent grid would be identical. (Note: The decision to display the 0000UT grids as representative grids for the entire 24-hour grid set was initially arbitrary, but in reviewing the analysis results it turns out that the total RMS $\Delta N_e(840)$ for the 0000UT grid was close to the RMS $\Delta N_e(840)$ for the entire set and never represented either the best- or worst-case grid.)

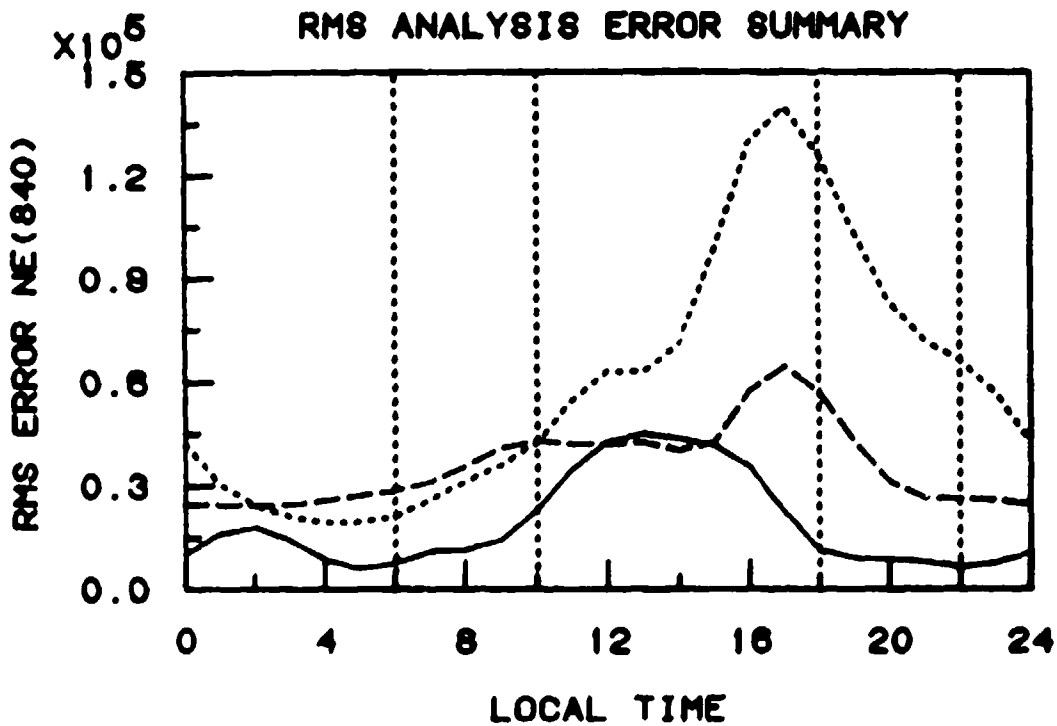
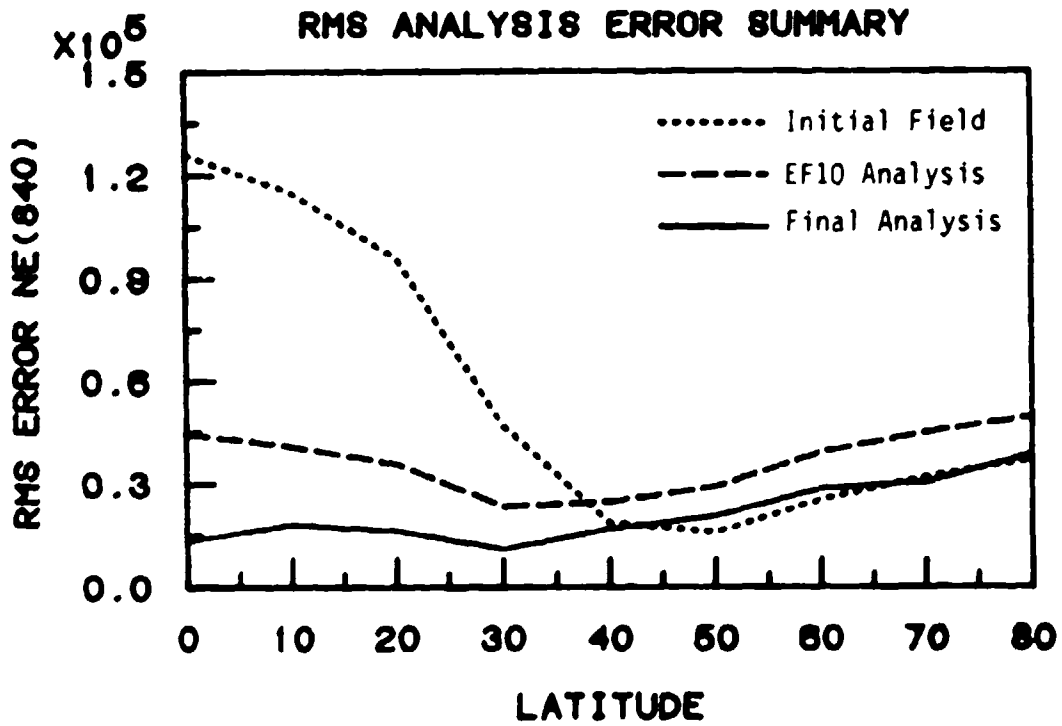


Figure 15. Summary of the RMS analysis error between the initial, effective F10 analysis, and global analysis fields and the Bent field for the entire 24 hour analysis period.

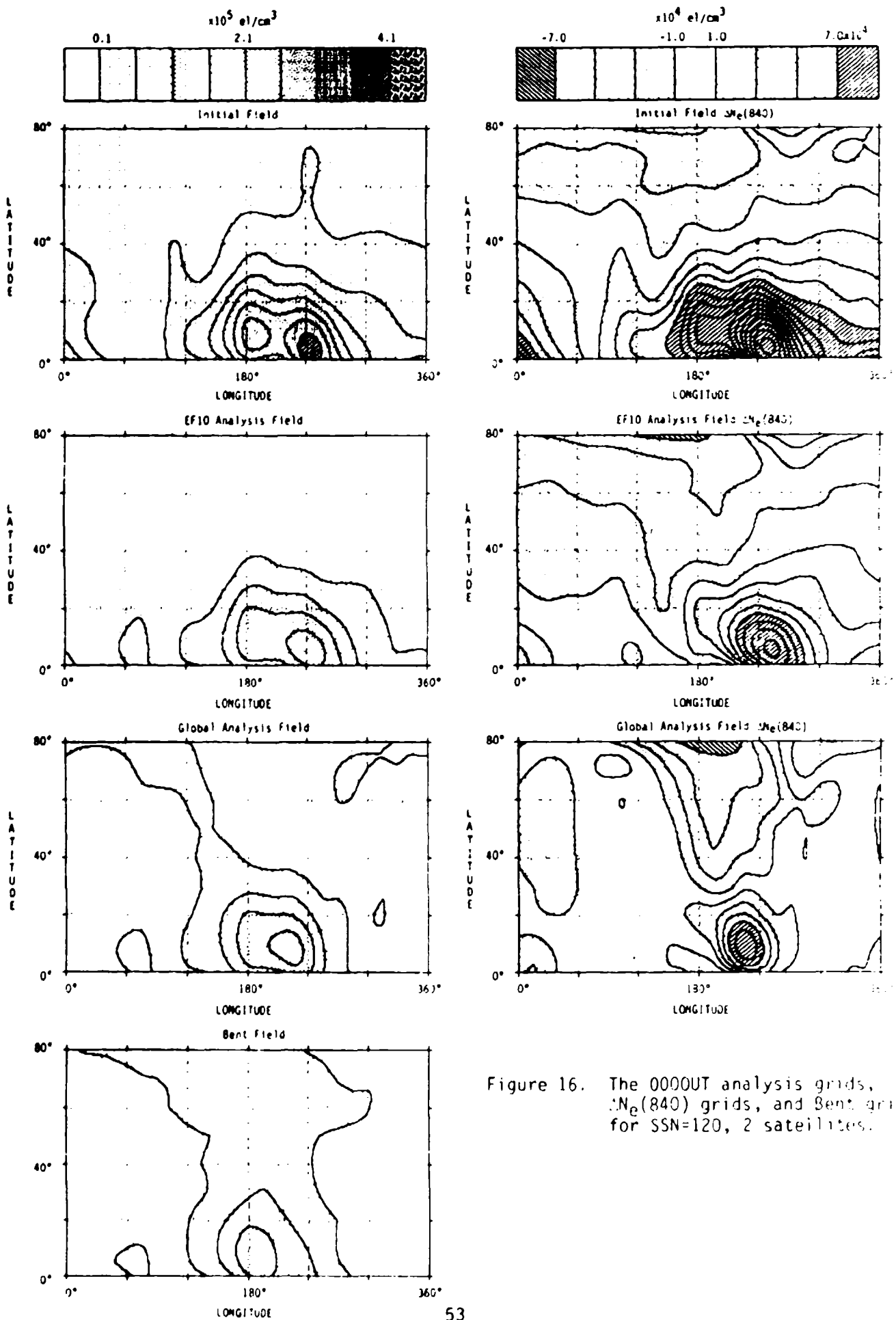


Figure 16. The 0000UT analysis grids, $N_e(840)$ grids, and Bent grid for SSN=120, 2 satellites.

4.1.5.2 Test Results

The analysis goodness-of-fit statistics from all Test 1 test cases are summarized in Table 6 (EF10 analysis) and Figure 17 (global analysis). Table 6 lists the initial EF10 estimate, calculated from Equation 29; the second EF10 estimate, calculated from Equation 31; and the EF10 estimate, calculated after one iteration of Equation 26. Included in this table is the average difference between the analysis field and the input data, $\overline{\Delta f_p}$, for each EF10. In all cases, the EF10 estimated after one iteration of Equation 26 produced a zero mean difference, as desired. As Figure 17 shows, the global analyses all converged uniformly, reaching a point of diminishing returns at roughly iteration number 6 or 7.

Table 6. Results of the effective F10 analyses in Test 1.

Test Case	Equation 29		Equation 31		First Iteration	
	EF10	$\overline{\Delta f_p}$	EF10	$\overline{\Delta f_p}$	EF10	$\overline{\Delta f_p}$
1a	69.78	0.0471	66.87	0.0043	66.58	0
1b	74.26	0.0501	71.16	-0.0010	71.22	0
1c	90.46	0.0160	89.45	0.0013	89.36	0
1d	97.46	0.0568	93.87	-0.0013	93.95	0
1e	119.31	-0.0205	120.63	0.0014	120.73	0
1f	130.09	0.0664	125.77	0.0014	125.86	0

Figure 18 illustrates how well the input data are fit. The two plots in this figure show the $f_p(840)$ data input for the first full orbit from both satellites (solid lines) from test case 1f (SSN=120, two satellites) and $f_p(840)$ calculated for the same orbit locations from the initial, EF10, and global analysis fields (dotted lines). The final RMS error for the entire analysis was 0.060 MHz in plasma frequency and 3.8×10^3 el/cm³ in electron density. This level of accuracy is reflected in the small deviations of the global analysis curves from the input curves in Figure 18. The only major deviations, occurring near orbit data point numbers 28 and 75, are near the F-layer apex poles. This is a difficult region to make changes to, as all data are weighted by the cosine of the F-layer apex latitude in the global analysis (see Equation 31), causing data near the poles to be almost completely ignored.

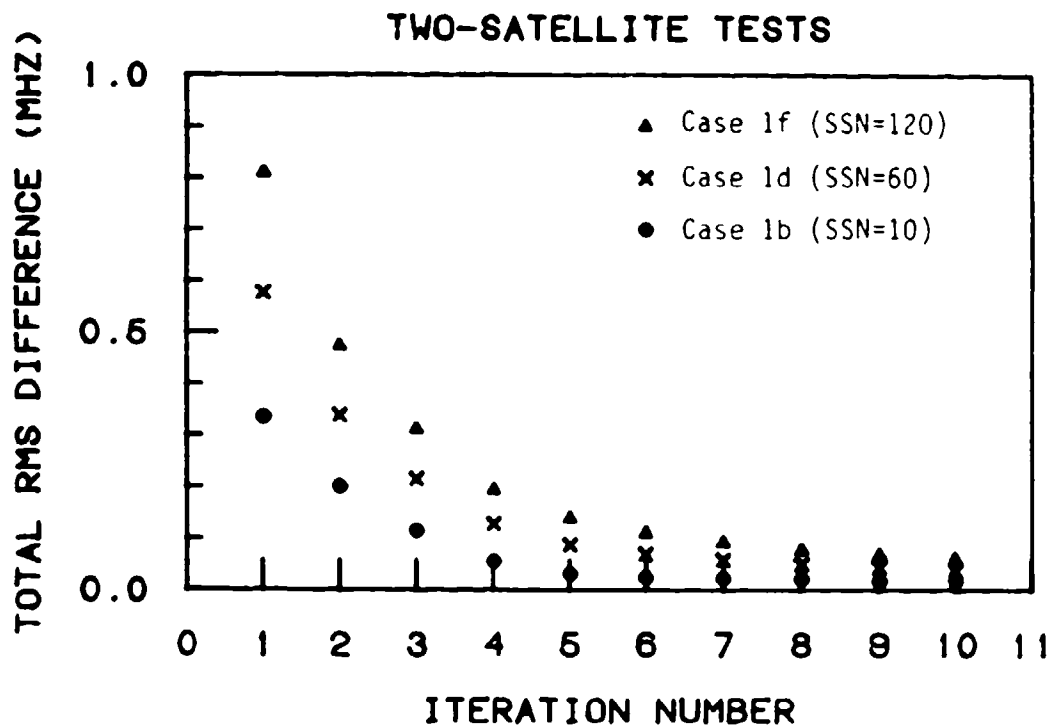
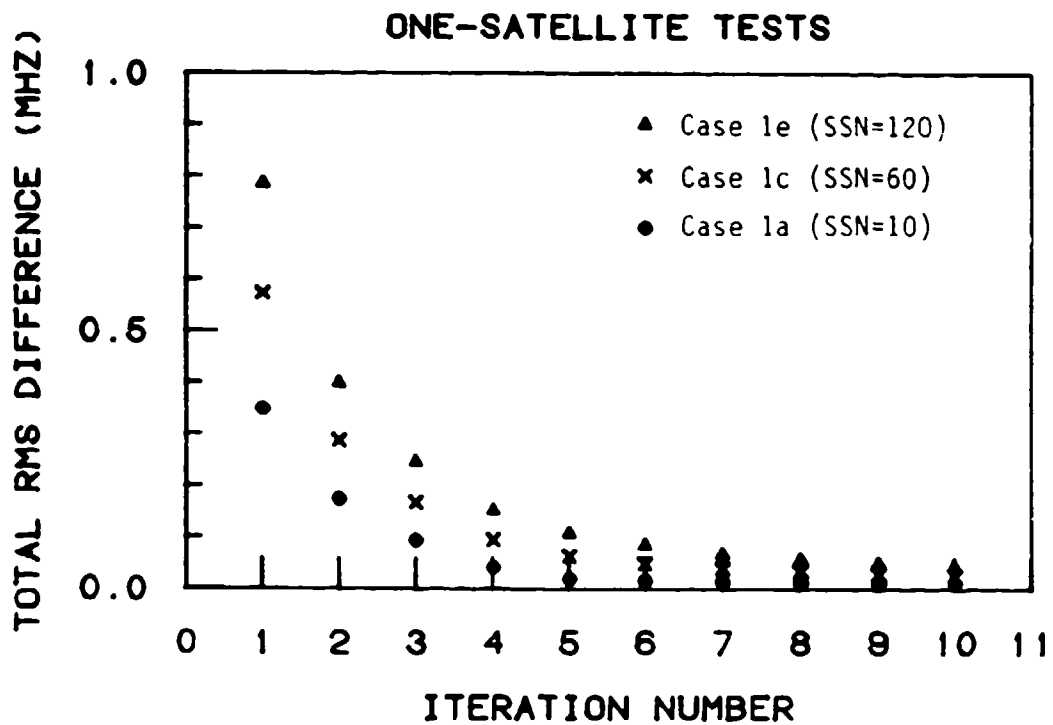


Figure 17. The RMS difference between the input f_p data and f_p calculated from Equation 22 as a function of global analysis iteration number.

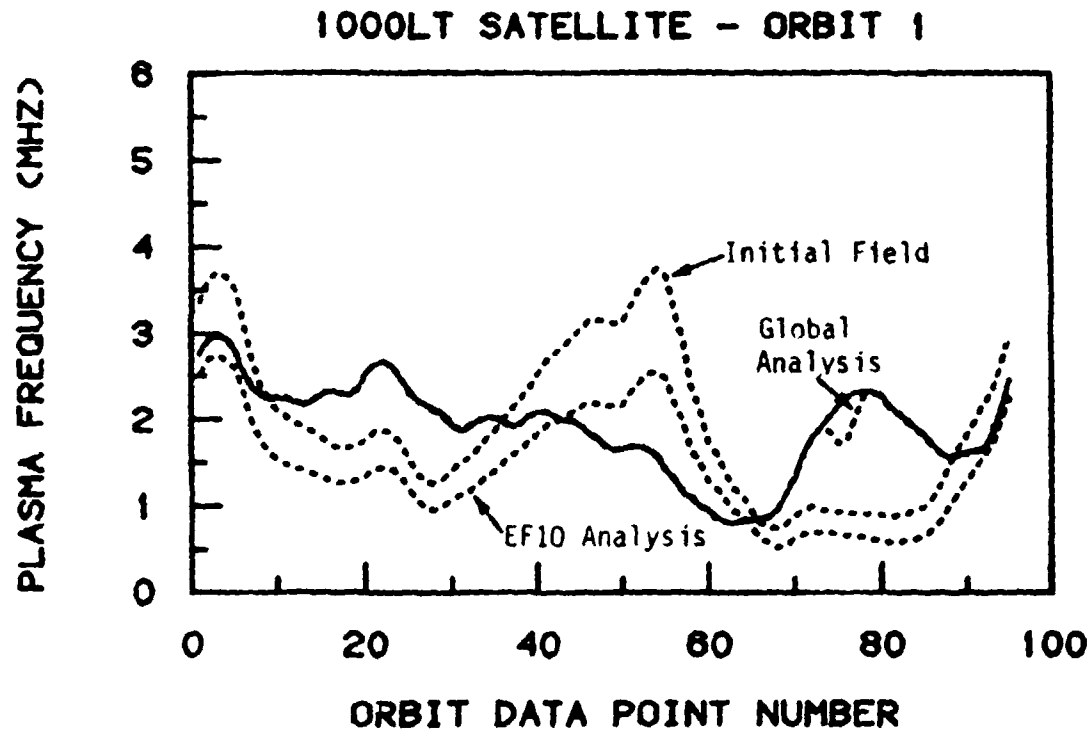
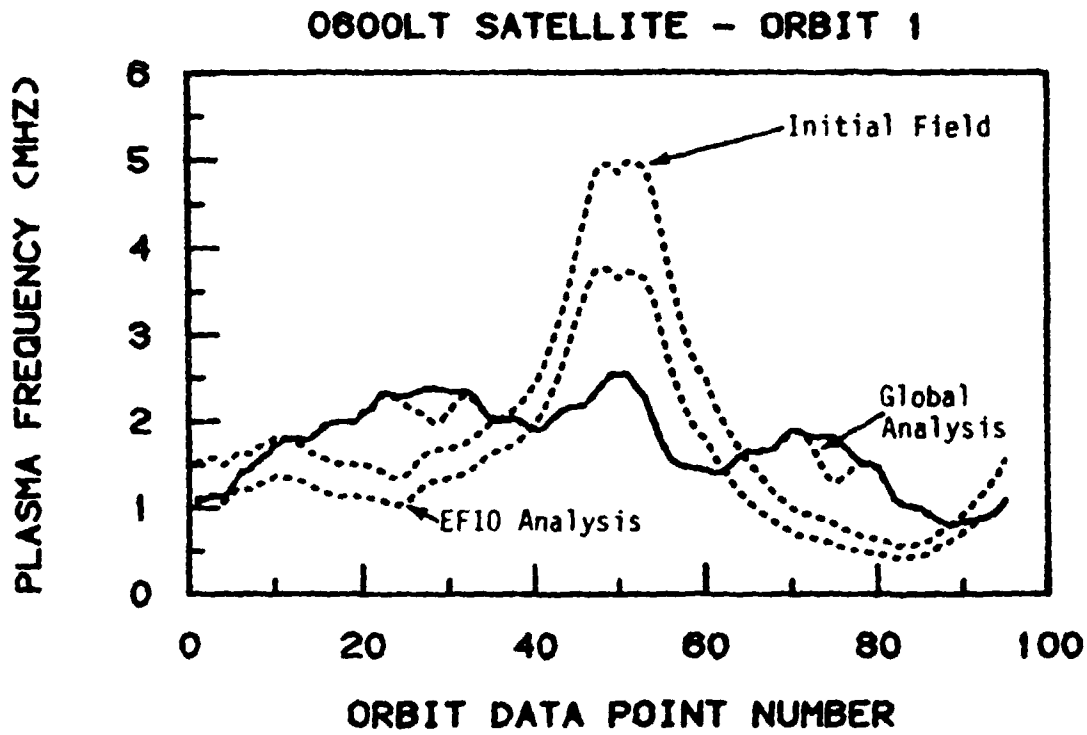


Figure 18. Analysis results for the first full orbit of both DMSP satellites for test case 1f.

Table 7 provides a summary of the RMS $\Delta N_e(840)$ and RMS percent $\Delta N_e(840)$

Table 7. Summary of the results of the $N_e(840)$ grid set comparisons.

Test Case	RMS $N_e(840)$			RMS % $N_e(840)$		
	Initial	EF10	Global	Initial	EF10	Global
1a	0.99	1.18	0.89	58.0	61.1	53.2
1b	0.99	1.29	0.77	58.0	60.8	41.2
1c	2.82	2.08	1.76	68.3	59.1	51.7
1d	2.82	2.14	1.40	68.3	58.6	39.2
1e	5.77	3.63	3.30	78.2	55.4	49.9
1f	5.77	3.59	2.58	78.2	54.7	39.3

$\times 10^4 \text{ e/cm}^3$
Percent

statistics for the $N_e(840)$ grid set comparisons for all six test cases. In each set of three numbers, the first is from comparing the initial field to the Bent field, the second from the EF10 field and the Bent field, and the third from the global analysis field to the Bent field. In general, the following observations can be made from these comparisons:

a. Not surprisingly, the 2-satellite cases (1b, 1d, 1f) provided better overall fits to the Bent grid sets than the corresponding 1-satellite cases (1a, 1c, 1e). The 1-satellite cases tend toward a final RMS percent $\Delta N_e(840)$ of around 50%, while the 2-satellite cases tend toward 40%.

b. In all cases, the final RMS $\Delta N_e(840)$ and RMS percent $\Delta N_e(840)$ are lower than that obtained with the initial analysis field, and the total processing gain as reflected in both figures increases with sunspot number.

c. The effectiveness of the EF10 analysis increases dramatically with sunspot number. There is actually a processing loss for low sunspot numbers, at least in terms of RMS differences, in the EF10 analysis. This is largely due to the fact that the EF10 analysis tries to reduce the average difference to zero, which can, in certain circumstances, increase the RMS difference. The fact that the analysis is done in plasma frequency while the statistics in Table 7 are in electron density can also contribute to this effect.

The observations are, for the most part, supported by the more detailed analysis results shown in Figures 19-30. Two figures are presented for each of the six test cases - the plots of RMS $\Delta N_e(840)$ as a function of latitude and local time (as in Figure 15) first, followed by the 0000UT grid contour plots. The main observation that can be drawn from these figures is that the global analysis field reverts back to the EF10 analysis field within roughly 30° of longitude, or 2^h of local time, of an orbit track. In other words, it is the relative accuracy of the shape of the $N_e(840)$ model used initially to generate the α_{ri}^{lmn} coefficients used in Equation 24 (the DHR model in the current tests) and the absolute accuracy provided by the EF10 analysis which determines the accuracy of the field more than 30° or 2^h away from data points. Conversely, where there is an adequate collection of data the global analysis can reproduce the actual field quite accurately, almost in spite of the field that the global analysis starts with. This can be seen in the dramatic improvement in the RMS $\Delta N_e(840)$ versus local time plots at around 16-20LT.

The objective of Test 2 was to study the effects of varying the convergence control parameter, W_c , on the global analysis algorithm (Equation 32). The SSN=60, 2-satellite data base from test case 1d was used for this test. The results are summarized in Table 8, which lists the RMS $\Delta f_p(840)$ values for each iteration step and the RMS $\Delta N_e(840)$ and RMS percent $\Delta N_e(840)$ values from the $N_e(840)$ grid set comparisons. These results are somewhat surprising in that the relatively arbitrary choice of $\Delta\lambda = 10^\circ$, $\Delta\phi = 15^\circ$, $\Delta t = 1^h$ and $W_c = 1.0$; values which were carry-overs from previous work on the 4D analysis model; provide the best fit in the $N_e(840)$ grid comparisons. A limited check of these results using the SSN-60, 1-satellite data base confirmed the finding that this choice of values for the parameters which go into calculating the value for W in Equation 32 appears to be close to optimal for processing orbital data. (In running the tests described in section 4.2, in which roughly 5000 data points were processed, W_c had to be reduced to roughly 0.6 to obtain convergence.)

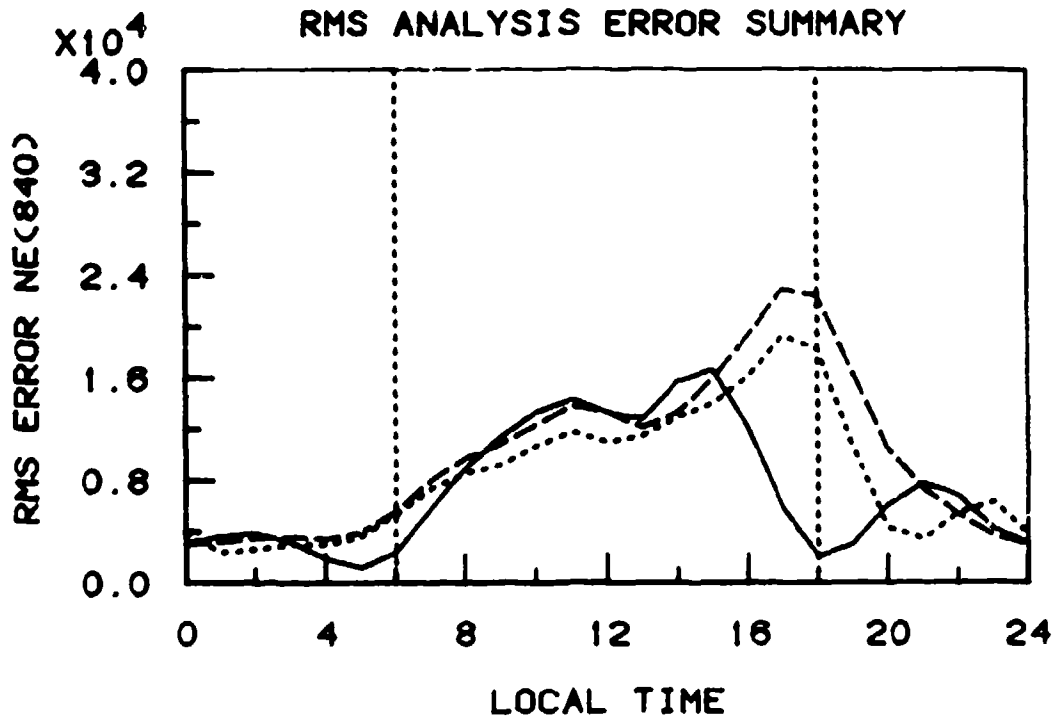
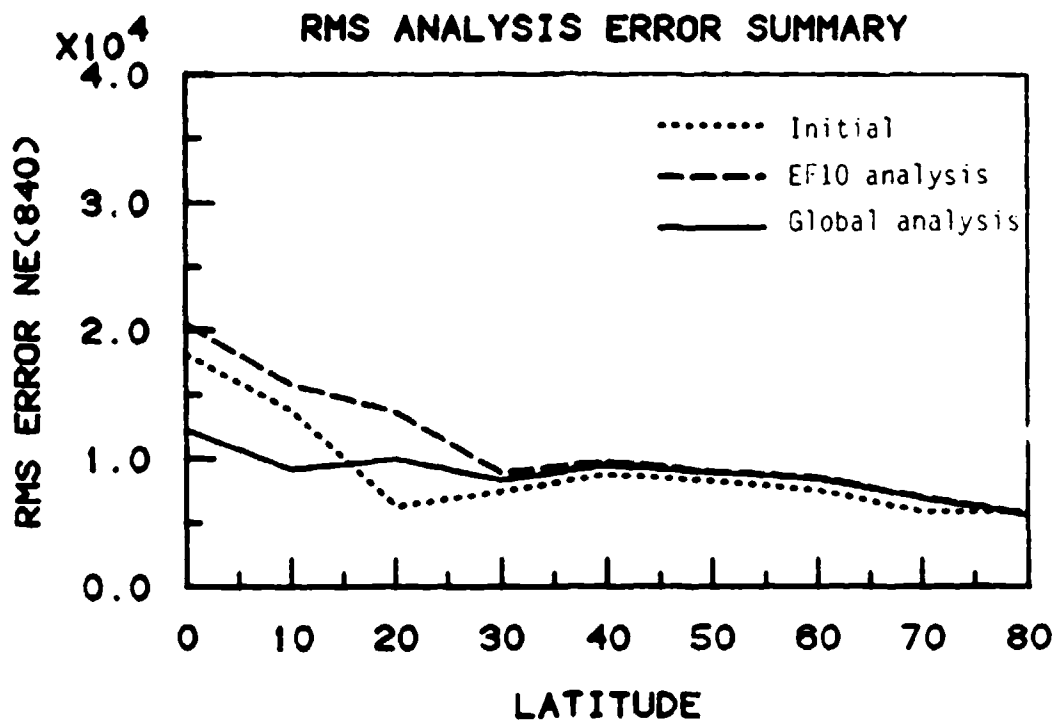


Figure 19. Summary of the $N_e(840)$ grid set comparisons for test case 1a (SSN=10, 1 satellite).

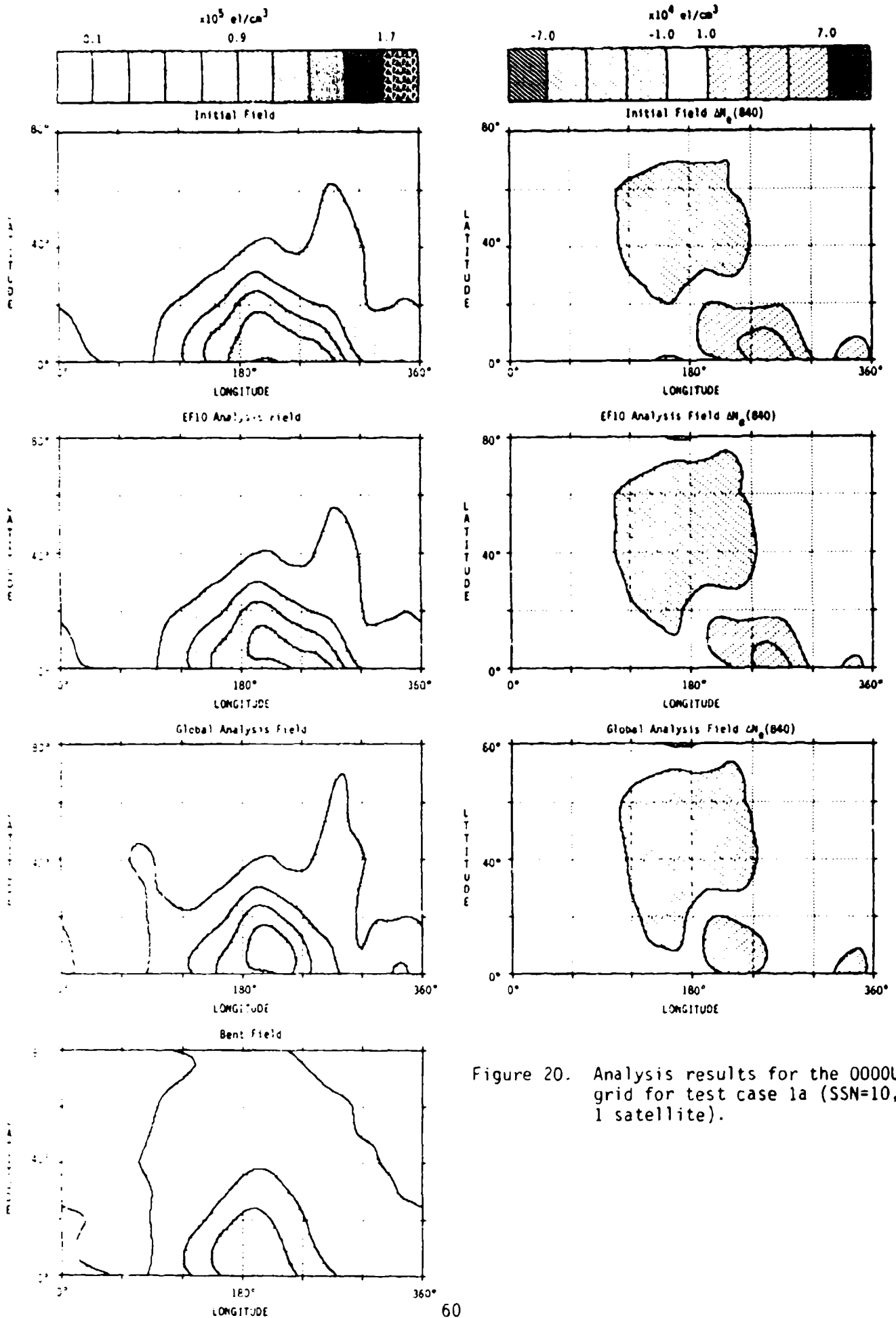


Figure 20. Analysis results for the 0000UT grid for test case 1a (SSN=10, 1 satellite).

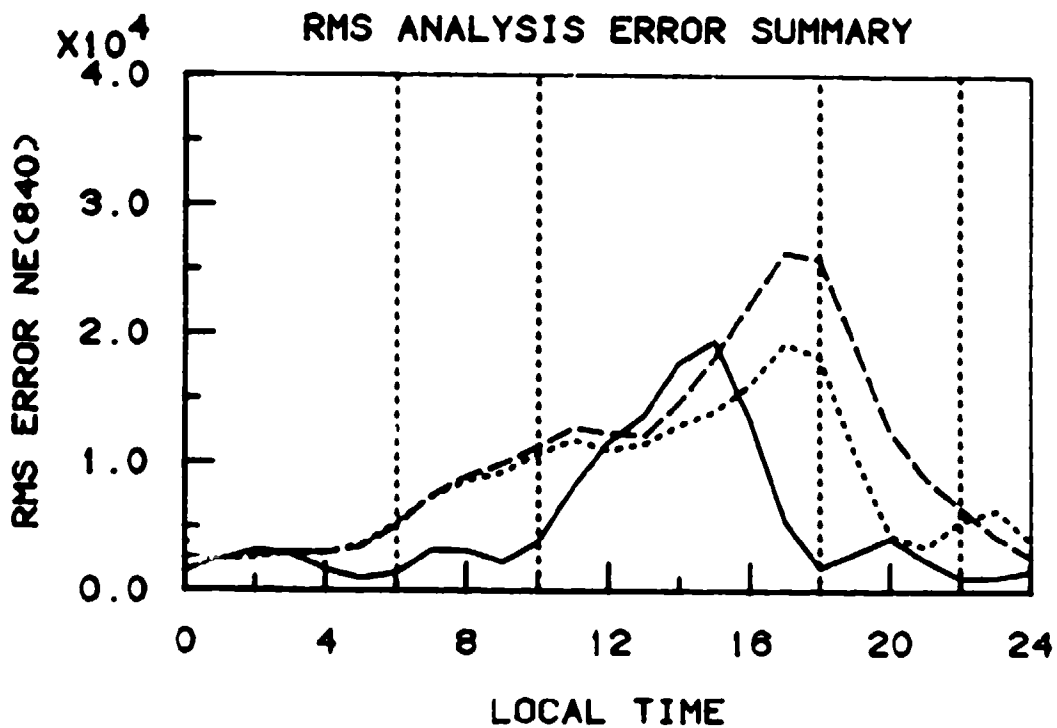
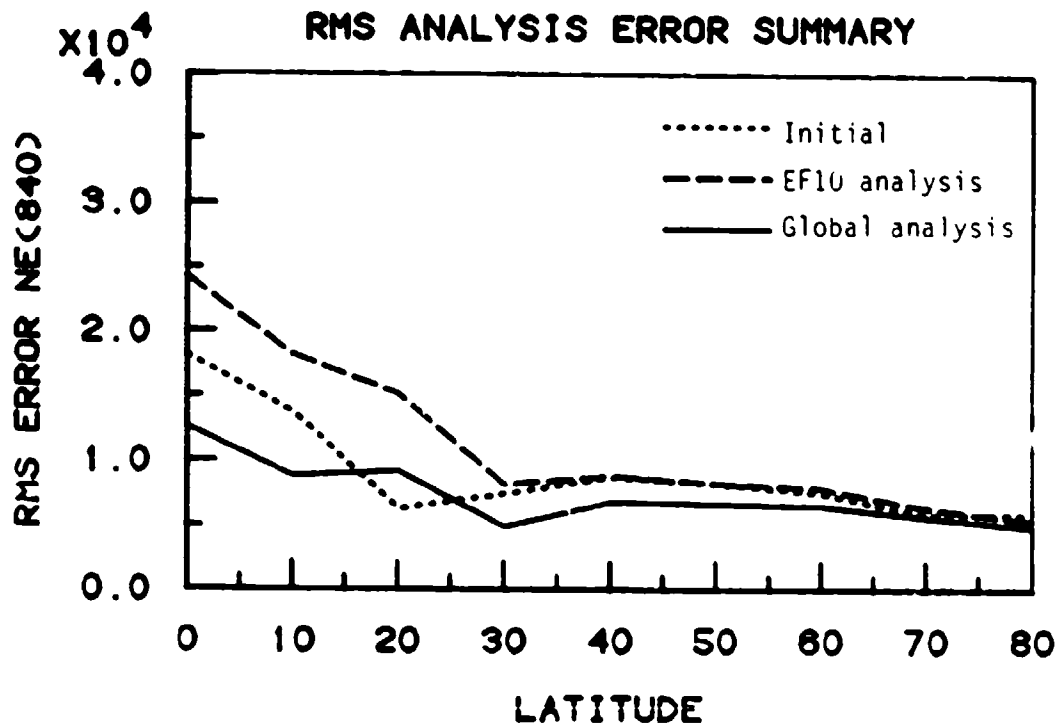


Figure 21. Summary of the $N_e(840)$ grid set comparisons for test case 1b (SSN=10, 2 satellites).

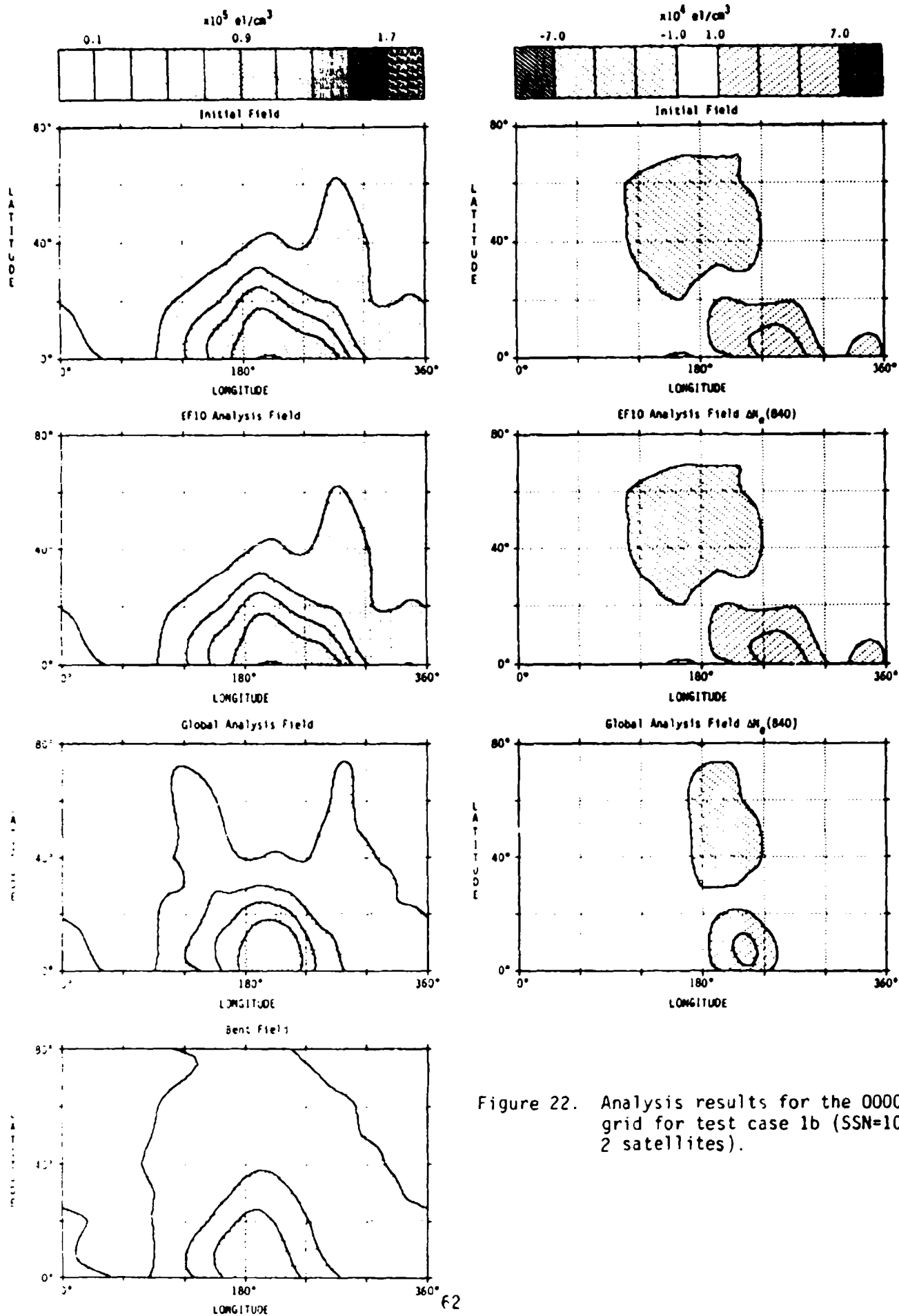


Figure 22. Analysis results for the 0000UT grid for test case 1b (SSN=10, 2 satellites).

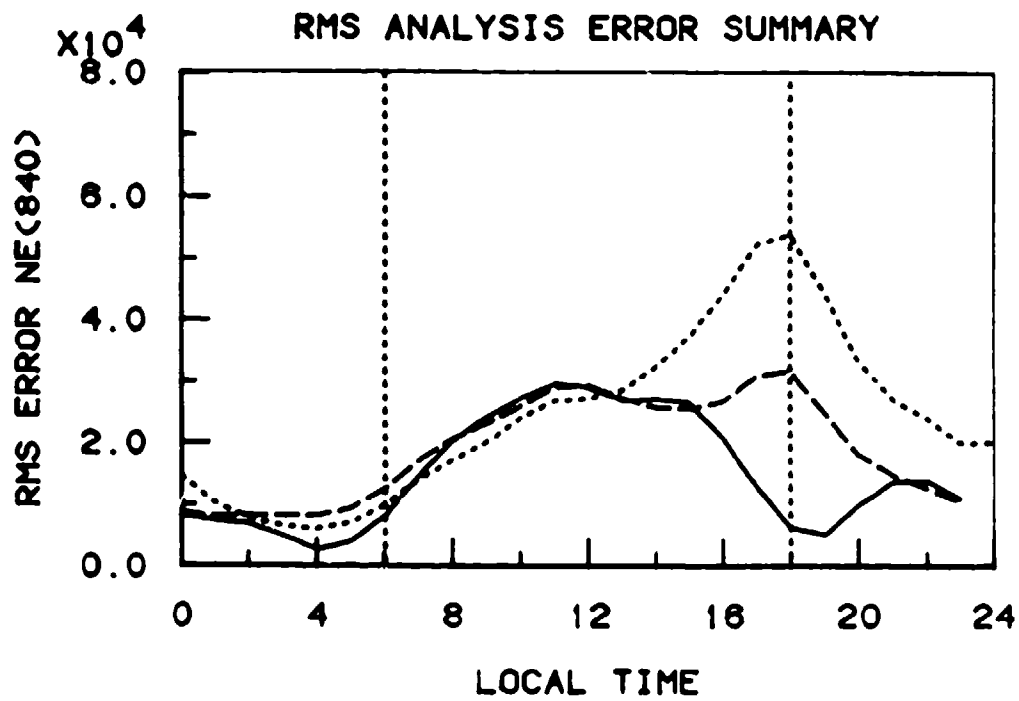
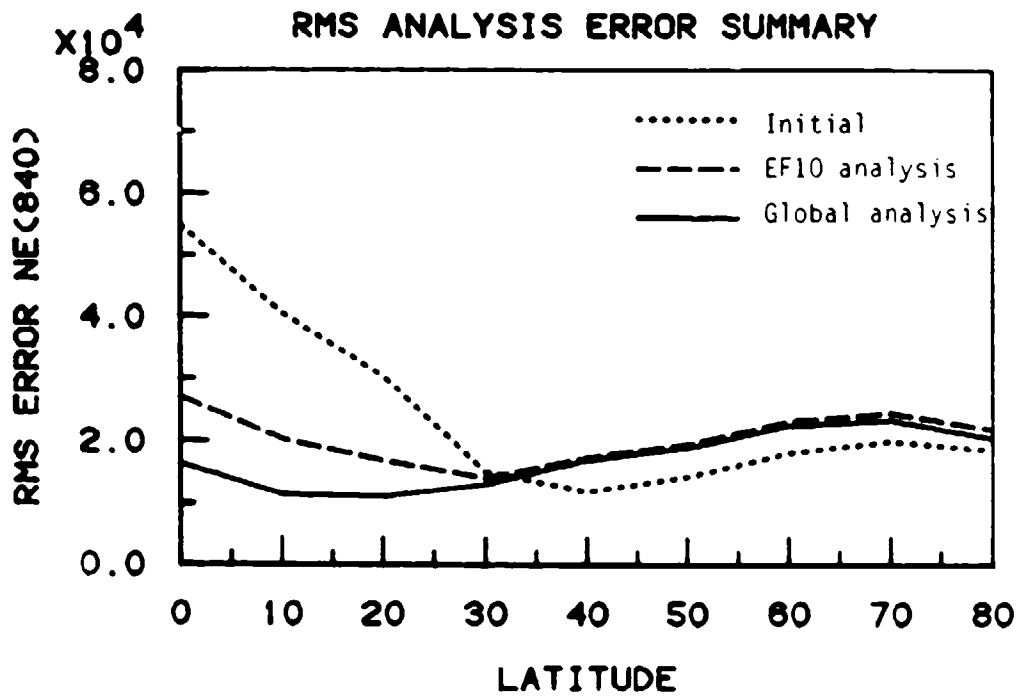


Figure 23. Summary of the $N_e(840)$ grid set comparisons for test case 1c (SSN=60, 1 satellite).

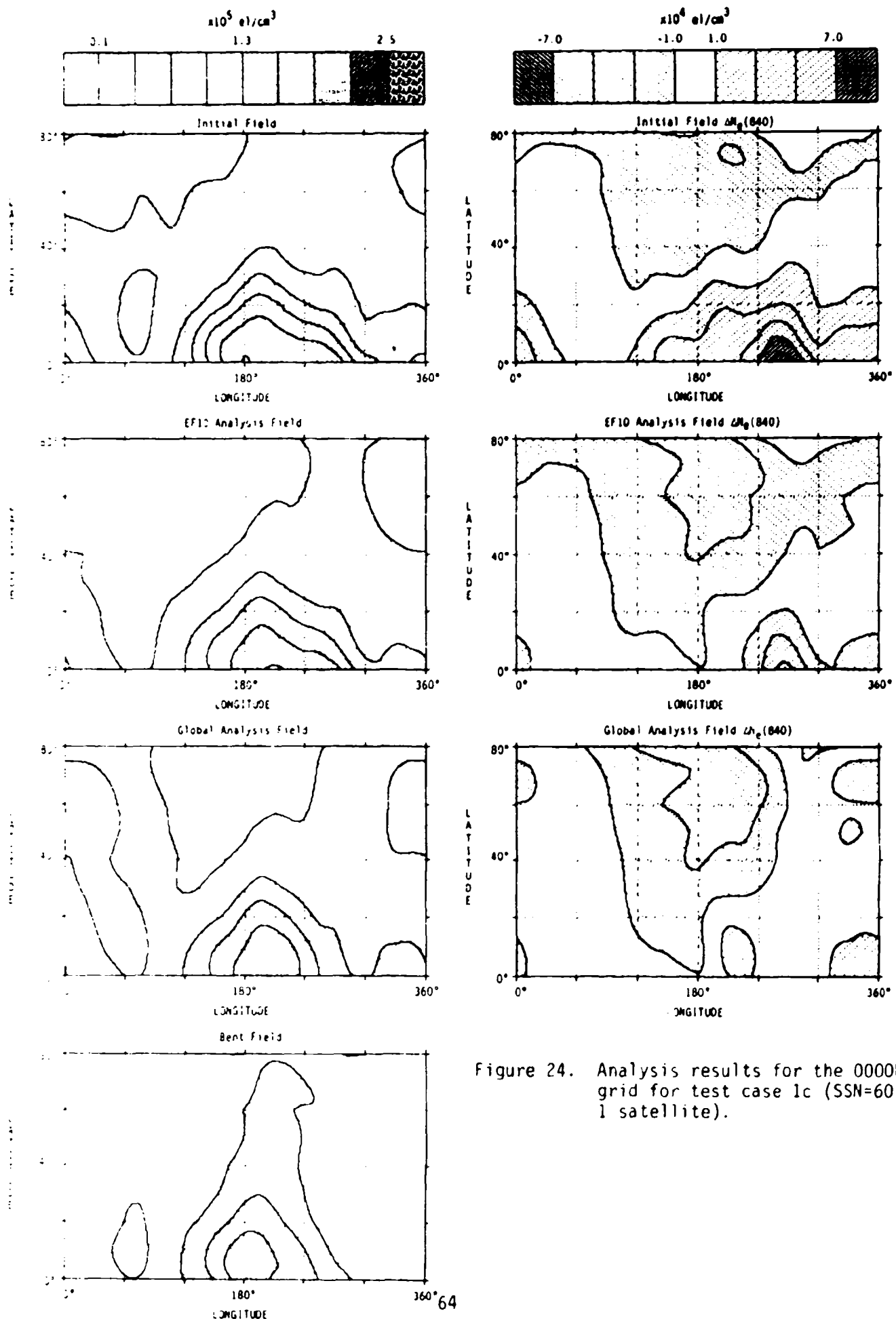


Figure 24. Analysis results for the 0000UT grid for test case 1c (SSN=60, 1 satellite).

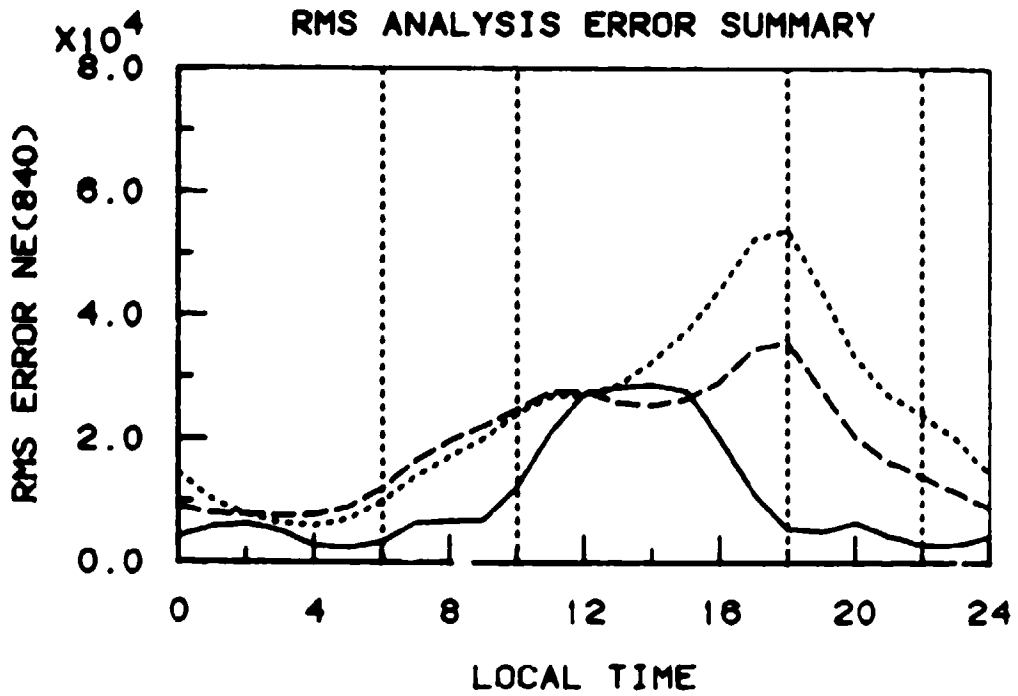
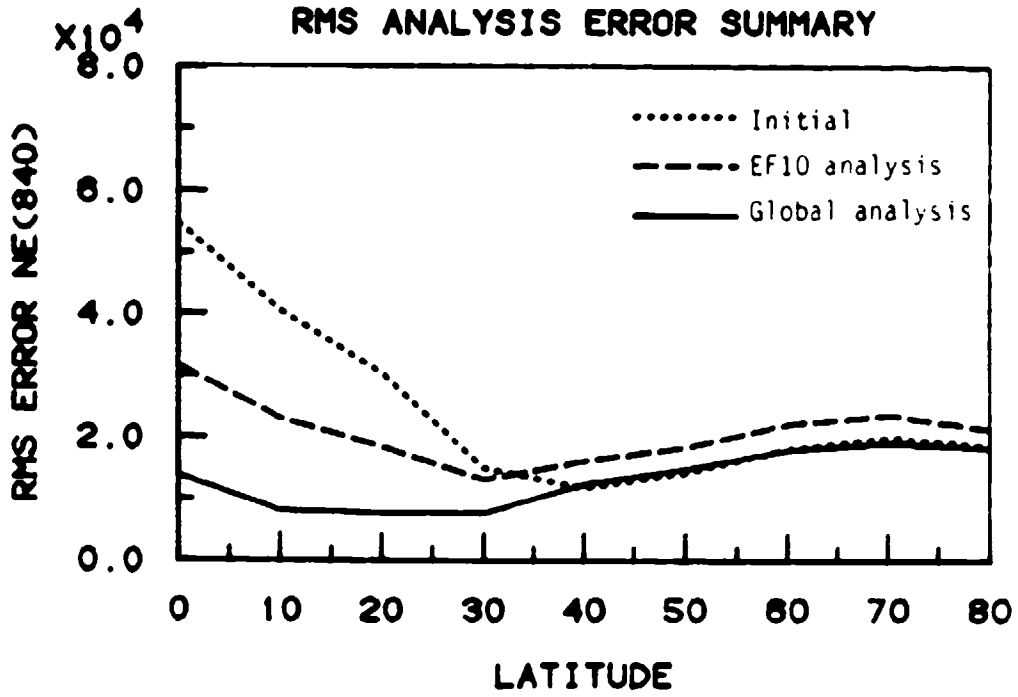


Figure 25. Summary of the $N_e(840)$ grid set comparisons for test case 1d (SSN=60, 2 satellites).

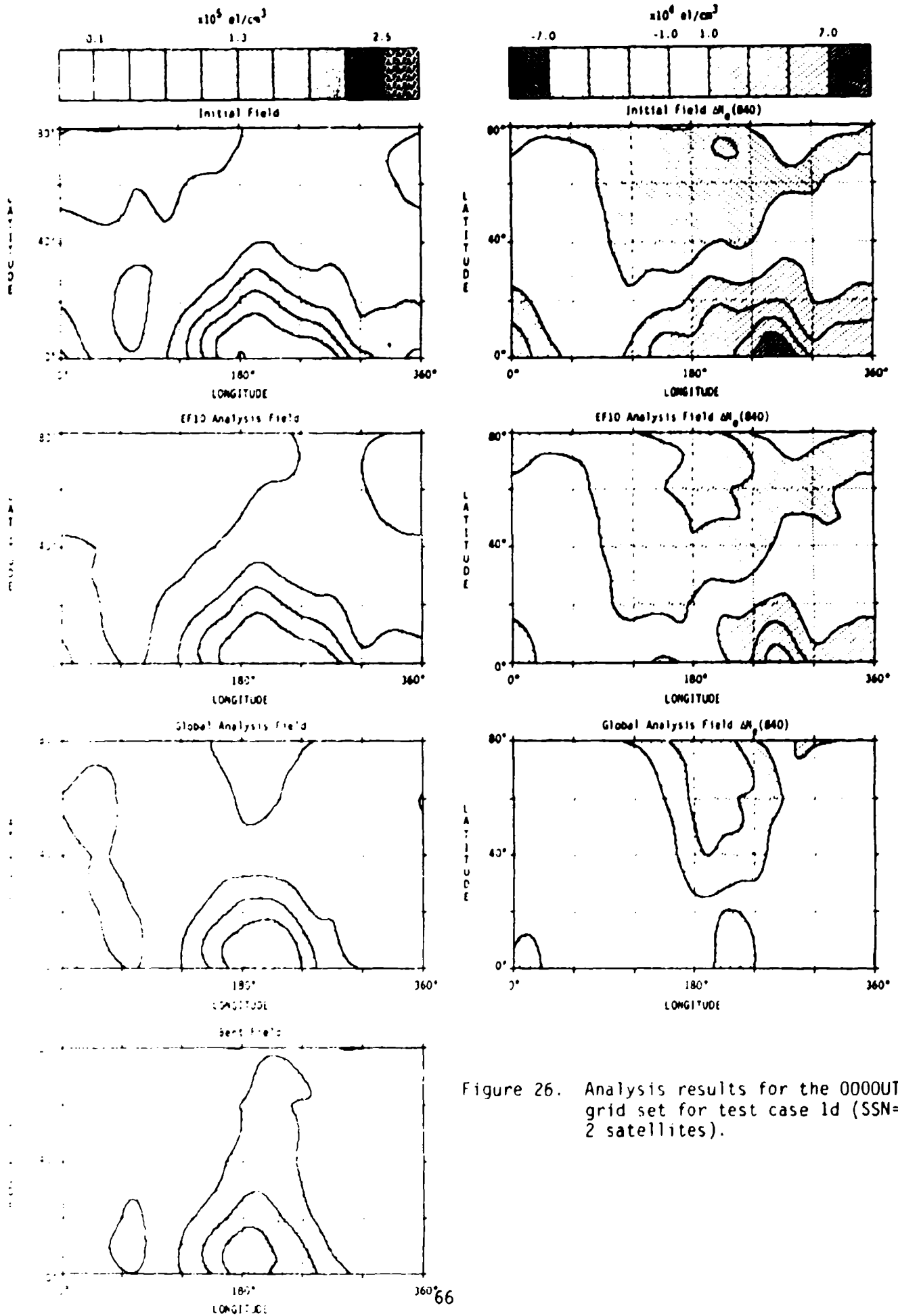


Figure 26. Analysis results for the 0000UT grid set for test case 1d (SSN=60, 2 satellites).

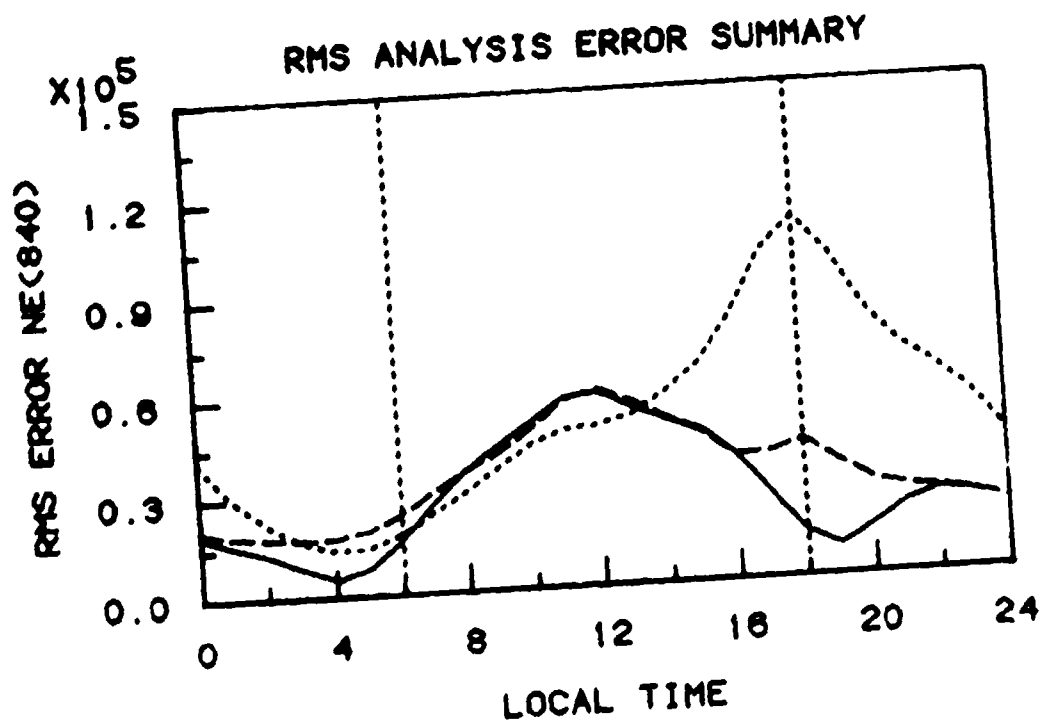
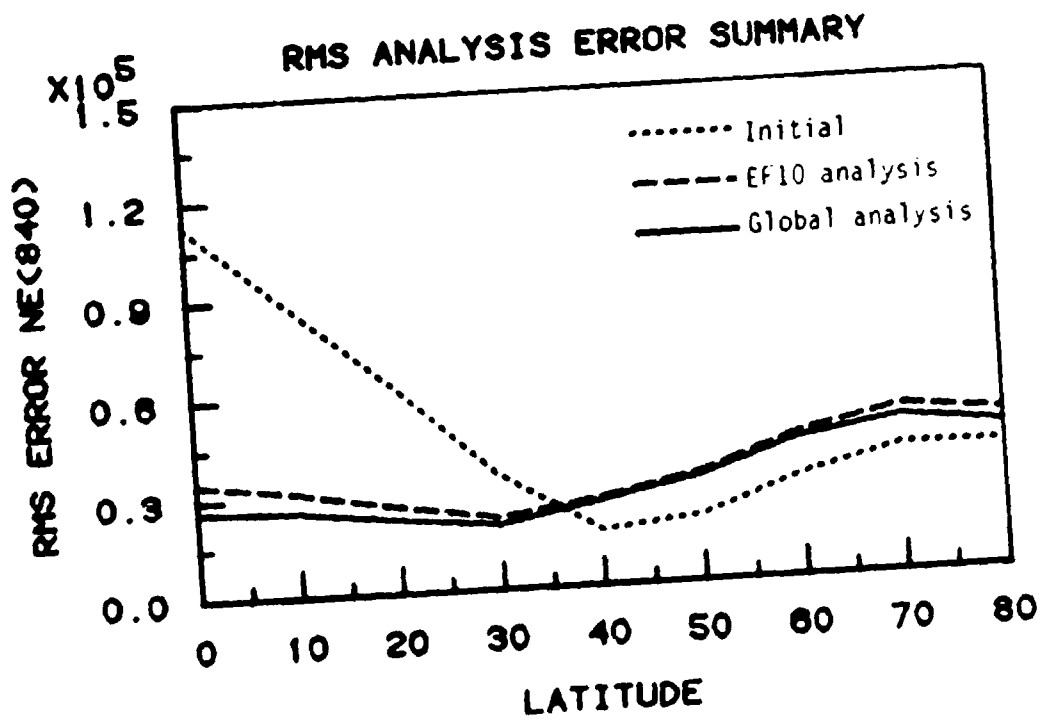


Figure 27. Summary of the $N_e(840)$ grid set comparison for test case 1e (SSN=120, 1 satellite).

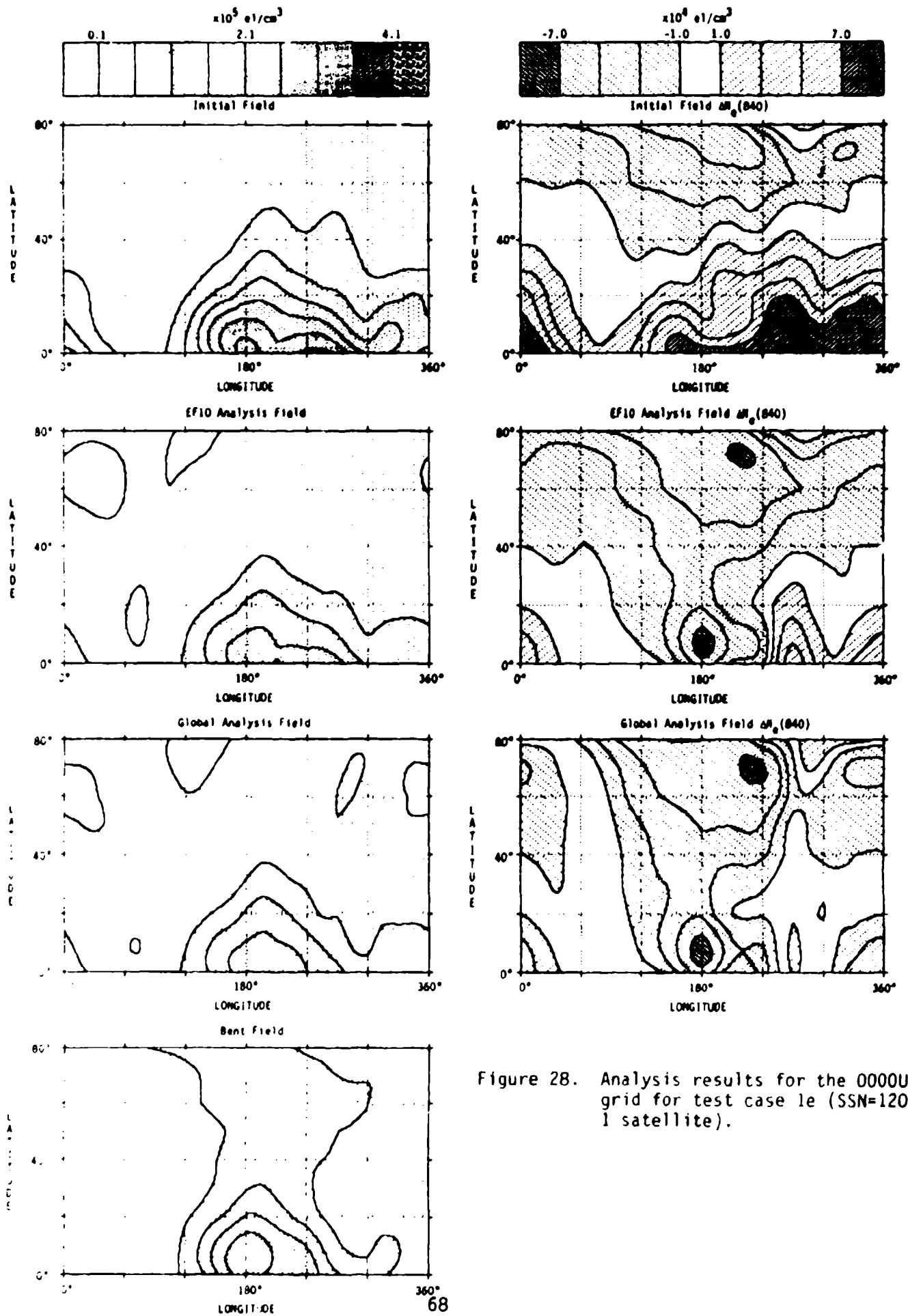


Figure 28. Analysis results for the 0000T grid for test case 1e (SSN=120, 1 satellite).

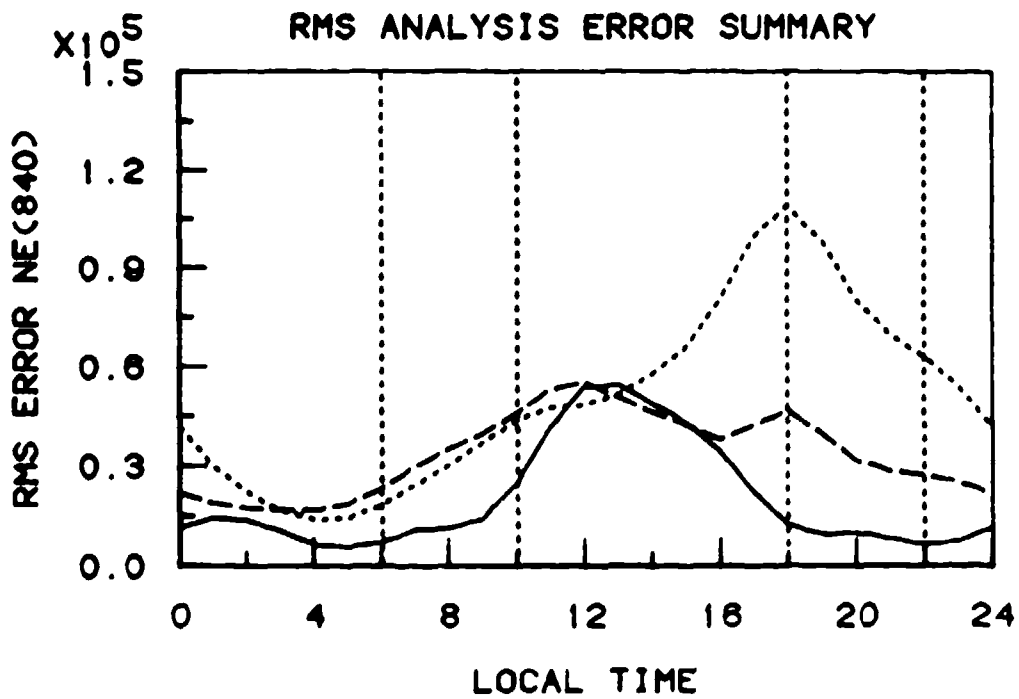
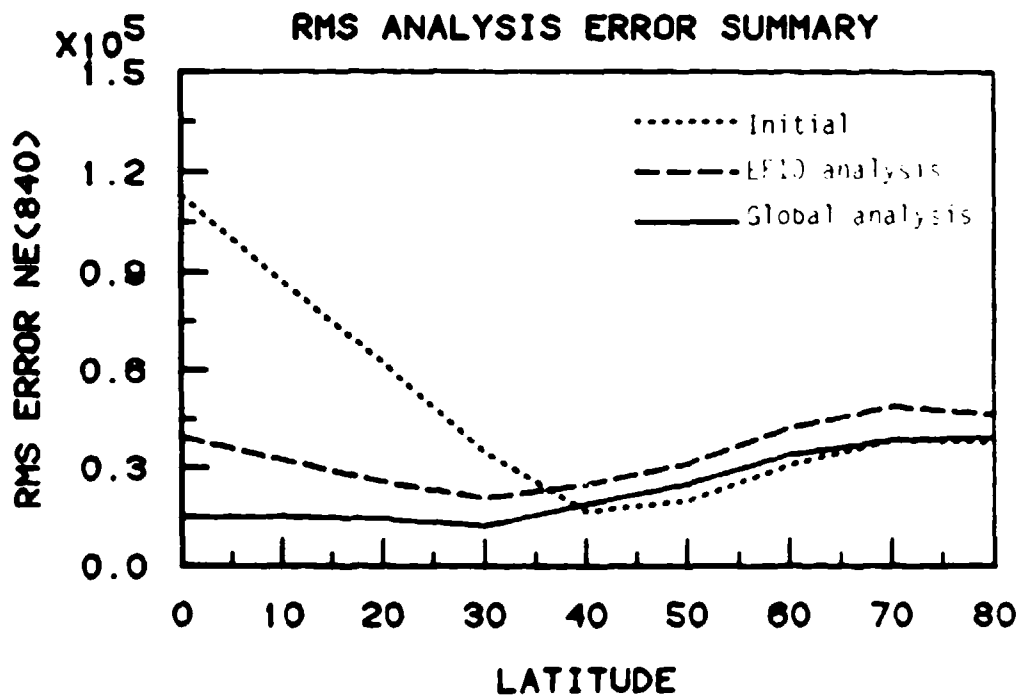


Figure 29. Summary of the $N_e(840)$ grid set comparisons for test case 1f (SSN=120, 2 satellites).

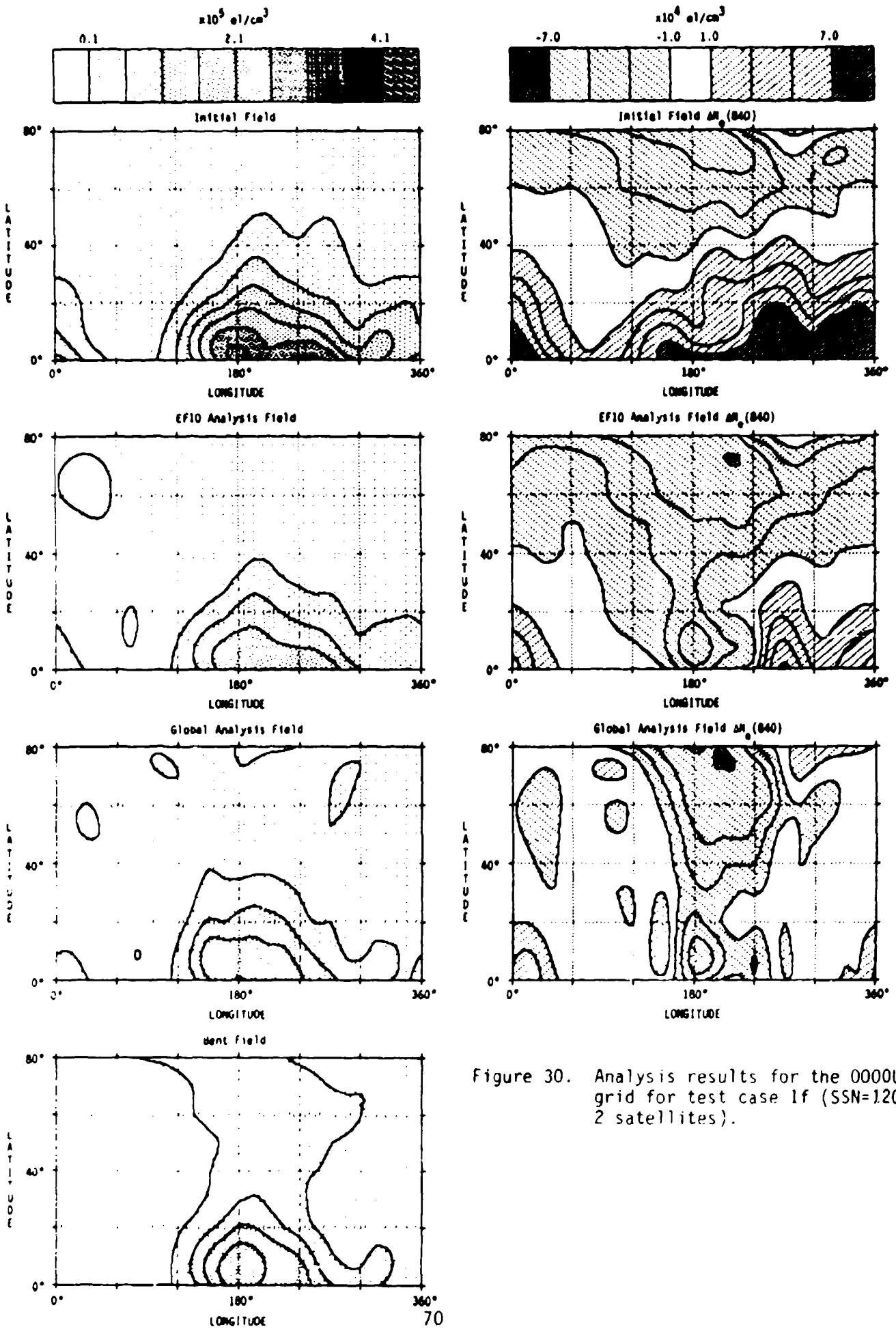


Figure 30. Analysis results for the 0000UT grid for test case 1f (SSN=120, 2 satellites).

Table 8. Test 2 results summary.

	2a	2b	2c	1d	2d	2e	2f	Case
	<u>1.50</u>	<u>1.25</u>	<u>1.10</u>	<u>1.00</u>	<u>0.90</u>	<u>0.80</u>	<u>0.50</u>	n_c
I	0.577	0.577	0.577	0.577	0.577	0.577	0.577	
T	0.352	0.311	0.332	0.339	0.350	0.366	0.431	
E	0.412	0.259	0.219	0.214	0.224	0.243	0.330	
R	-D-	0.269	0.156	0.127	0.128	0.144	0.235	
A		-D-	0.139	0.087	0.079	0.089	0.161	
T			0.137	0.069	0.058	0.066	0.120	MHz
I			0.140	0.058	0.046	0.052	0.095	
O			-D-	0.049	0.038	0.043	0.079	
N				0.043	0.032	0.037	0.067	
10				0.039	0.028	0.032	0.058	
RMS	-	-	-	1.40	1.42	1.43	1.51	$\times 10^4 \text{ el/cm}^3$
RMS%	-	-	-	39.2	39.8	40.1	41.2	%

The objective of Test 3 was to study the effects of varying the initial truncation limits on the longitude (M) and time (L) expansions in Equations 22 and 32. As in Test 2, the SSN=60, 2-satellite data base from test case 1d was used for this test. The results of this test are summarized in Table 9, which lists the RMS $\Delta f_p(840)$ values for each iteration step and the RMS $\Delta N_e(840)$ and RMS percent $\Delta N_e(840)$ values from the $N_e(840)$ grid set comparisons. The gain achieved by starting the analysis with only the lower wave numbers is very obvious in these results. Although the cases using higher truncation limits initially do better at fitting the input data, all cases are roughly equal by iteration step 7, and the lower truncation limit cases produce better fits at iteration step 10. Even more significant is the gain evident in the fits to the overall field reflected in the RMS $\Delta N_e(840)$ and RMS percent $\Delta N_e(840)$ parameters, indicating that the information in the input data is being more effectively spread away from the data point locations by using lower initial truncation values.

Table 9. Test 3 results summary.

	3a	3b	3c	3d	3e	Case	
	<u>13/5</u>	<u>15/7</u>	<u>17/9</u>	<u>19/11</u>	<u>21/13</u>	M/L	
ITERATION	1	0.573	0.577	0.580	0.579	0.578	
	2	0.359	0.350	0.323	0.259	0.224	
	3	0.245	0.223	0.170	0.136	0.136	
	4	0.163	0.127	0.099	0.093	0.096	
	5	0.099	0.079	0.072	0.071	0.073	MHz
	6	0.064	0.058	0.055	0.058	0.058	
	7	0.049	0.046	0.045	0.050	0.049	
	8	0.039	0.038	0.038	0.046	0.042	
	9	0.033	0.032	0.033	0.046	0.038	
	10	0.028	0.028	0.029	0.046	0.036	
RMS	1.35	1.42	1.53	1.61	1.77	$\times 10^4 e_1/cm^3$	
RMS%	38.5	39.9	41.4	44.1	47.3	%	

An additional gain is in processing time. Since there are fewer terms to sum over in both Equation 22 and 32, the lower the initial truncation limits the faster the global analysis will run. The CPU times for the two extreme cases shown in Table 9 were 203 seconds for case 3a and 225 seconds for case 3e, a decrease in resource usage of 10% in order to achieve a better analysis.

4.1.6 Limitations

The major weakness of the preprocessor, as implemented for testing, is in the spectral $N_e(840)$ model which serves as the first-guess field. Both models used, the AWS DHR model and the Bent model, were designed primarily for the calculation of integrated electron content values, even though the Bent model was initially derived from topside ionosonde data. The effects of this are most apparent in the fields generated from the DHR model coefficients which often include odd features, such as the two features at 105°E and 240°E in the upper panel of Figure 13, induced by the local-time varying topside scale height factors used by the DHR model. These factors also produce the intense second diurnal maximum at around 1700LT in the equatorial region. On

the other hand, the $N_e(840)$ values calculated from the Bent coefficients appear to be too low for a given F10 value. This is less of a problem, given the results of the effective F10 tests, but it is not clear that the relative field shape (in latitude and longitude) provided by the Bent model is any better or worse than that provided by the DHR model. Additionally, neither model does well at high latitudes or during geomagnetic storms.

A related limitation, also due to limitations placed on the implementation of the algorithms rather than the algorithms themselves, is the maximum truncation limits used in Equations 22-24 and 32, which limit the inherent resolution of the analysis. These were selected by a trade-off between desired resolution (in latitude, longitude, and time) and program size and run-time, and should be redefined based on actual user requirements and resources in any operational implementation of this preprocessor.

4.2 Task 5: Combined TEC and $N_e(840)$ Preprocessor

Tests were made using the GRIDNE program described in Section 4.1 to investigate the effects of incorporating $N_e(840)$ data inferred from TEC observations into analyses of SSIE $N_e(840)$ data. Three tests were run using data generated using the Bent coefficients with Equations 22-24, and one test was run using TEC data from the AFGWC TEC data preprocessor and SSIE data from the AGDB.

In the first three tests, it is assumed that a processor is available which will produce estimates of $N_e(840)$ from TEC, so that only $N_e(840)$ data is provided to the program. These three tests use the SSN=60, 2-satellite data base from the testing described in Section 4.1.5.2, and add three different TEC-inferred $N_e(840)$ data sets:

1. Data from the 12 AWS polarimeter locations (stations' listed in Table 10 for each of 24 hours (288 additional data points).
2. Data on an F-layer apex grid (Grid 1) from 20°N to 60°N latitude in 10° increments, 0° to 345°E longitude in 15° increments, and 00UT to 2407 in one-hour increments (2880 additional data points).

Table 10. TEC station penetration point locations.

<u>Station</u>	<u>Latitude</u>	<u>Longitude</u>
Athens	34°N	18°E
Goose Bay	49°N	294°E
Osan	35°N	128°E
Patrick AFB	27°N	278°E
Ramey	17°N	291°E
Sagamore Hill	39°N	288°E
Boulder	37°N	254°E
La Posta	30°N	244°E
Taiwan	23°N	122°E
Palehua	20°N	203°E
Shemya	47°N	164°E
Anchorage	54°N	214°E

Table 11. TEC tests results summary.

	<u>EF10</u>	<u>f_p(840)</u>	<u>RMS</u>	<u>RMS%</u>
No TEC	93.95	0.039	1.40	39.2
Stations	96.56	0.038	1.36	37.3
Grid 1	105.93	0.032	1.43	33.6
Grid 2	99.92	0.030	0.81	23.3
Stations (NT)	96.56	0.036	1.31	36.2
Grid 3 (NT)	101.32	0.034	0.78	20.8

3. Data on an F-layer apex grid (Grid 2) from 0° to 70° N latitude in 10° increments with the same longitude and time coverage as in (2) (4608 additional data points).

The last two data sets were assumed to be from some TEC data preprocessor.

The results of these three tests are summarized in Table 11, and the 0000UT $N_e(840)$ and $\Delta N_e(840)$ grids for all three are shown in Figure 31 along with the Bent $N_e(840)$ grid. As Table 3 shows, the quality of the analysis improves with increasing data input, with the exception of the Grid 1 case where the RMS $\Delta N_e(840)$ increased although the RMS percent $\Delta N_e(840)$ decreased. This is due to the higher EF10 value calculated for this case (105.93), as can be seen in Figure 31. Although the mid latitudes are now very close to the Bent field (the results of the global analysis), the low latitudes are much higher than in the other two cases, a direct result of the higher EF10 value. Since the $N_e(840)$ values are higher at low latitudes than mid latitudes, this caused the RMS $\Delta N_e(840)$ value to increase even though the overall fit, as reflected in the RMS percent $N_e(840)$ value, was better. In the Grid 2 case, where almost an entire hemispheric grid was processed, the global analysis has modified the field completely so that it is almost identical to the Bent grid.

As stated in Section 4.1.3, the variable truncation limit scheme was applied only to the longitude and time dimensions. The latitude dimension was not included, as the orbit-track data set provided more than adequate resolution in latitude, relative to the polynomial order used in the latitudinal analysis ($N=20$). In the cases examined here, with isolated (in latitude) data points and longitude-time data strips, it makes sense to extend the scheme to latitude as well. This was implemented by tying the maximum latitudinal polynomial order to the longitudinal wave number in such a way as to preserve the modified triangular truncation scheme⁹ throughout the analysis. (Note:

ANALNE and CALNE subroutines which implement this scheme are included at the end of the GRIDNE program listing in Appendix C.)

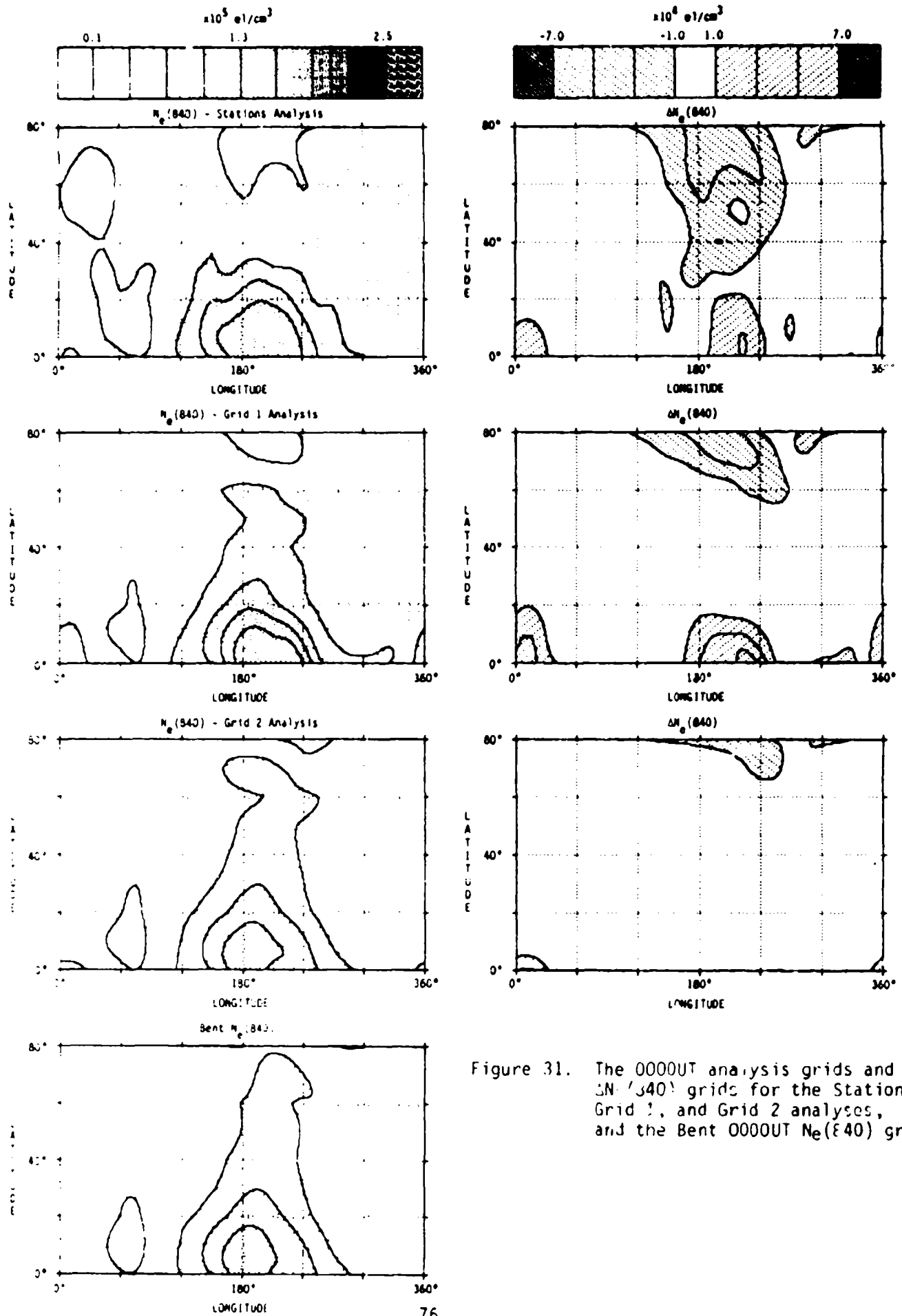


Figure 31. The 0000T analysis grids and $\Delta N_e(840)$ grids for the Stations, Grid 1, and Grid 2 analyses, and the Bent 0000T $N_e(840)$ grid.

Two additional analyses were run using the new station scheme - a repeat of the TEC stations analysis, denoted Stations (NT), and an analysis of a third grid data set, denoted Grid 3 (NT), which consisted of data on an F-layer apex grid from 10°N to 70°N latitude in 20° increments, 0° to 345° E longitude in 15° increments, and 00UT to 24UT in one-hour increments (2880 additional data points). The overall statistics from these analyses are included in Table 11, and the 0000UT $N_e(840)$ and $\Delta N_e(840)$ grids are shown in Figure 32. As can be seen in the statistics, the analysis improves slightly in the stations case and dramatically for the Grid 3 analysis, which provides a better analysis than the Grid 2 case, which included twice as much input data and extended down to the magnetic equator.

A final series of limited tests were carried out at AFGWC using output from the AFGWC TEC preprocessor, program POLY1, and SSIE observations from the Astrogeophysical Data Base (AGDB). Due to known deficiencies in the POLY1 program (Bussey, private communication) and the questionable nature of the SSIE data due to sensor malfunction several months earlier, only the effective F10 analysis was run in order to compare the mean field representing each data set. The POLY1 program generates 24 TEC grids, one per UT, from 5-day mean TEC observations and stores them in file FOURDGRIDS. Software from the Topside Data Interface System¹ was used to convert the TEC grids into grids of $N_e(840)$ using f_oF2 and M3000 from the ITS ionosphere model²⁶ and the DHR profile model. (The sunspot number used in the ITS model was 36.1, F10=91.2, which was obtained from the effective SSN analysis²⁷ run on 5-day mean f_oF2 data for the same period.) The grids of $N_e(840)$ (5165 data points) were then passed to program GRIDNE for the EF10 analysis. The SSIE $N_e(840)$ data were taken directly from the AGDB for the same 5-day period. This provided a total of 4705 good data points from DMSP satellite F7.

The effective F10 values obtained from the two analyses were quite different - 94.71 from the TEC data and 170.61 from the SSIE $N_e(840)$ data. As there was some question as to the absolute accuracy of the SSIE observations due to the sensor malfunction, several additional EF10 analysis were run in which the SSIE $N_e(840)$ data were all divided by some constant factor. The results are given in Table 12, which lists the effective F10 and average

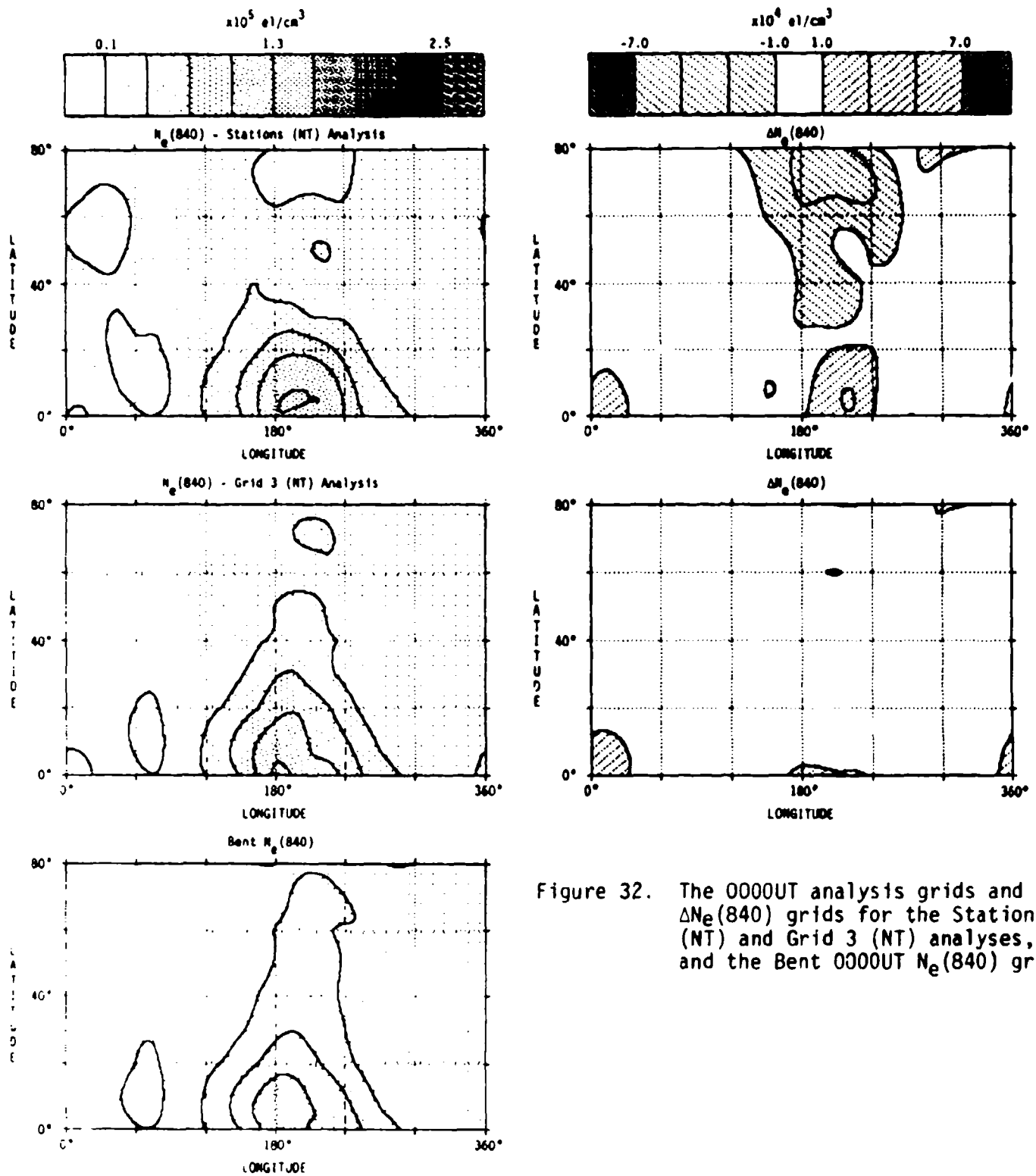


Figure 32. The 0000UT analysis grids and $\Delta N_e(840)$ grids for the Stations (NT) and Grid 3 (NT) analyses, and the Bent 0000UT $N_e(840)$ grid.

$f_p(840)$ for the POLY1 data and the various SSIE tests. It appears from this somewhat limited analysis that the SSIE $N_e(840)$ values are roughly a factor of 3.3-3.5 too high. This finding was discussed with Dr. Fred Rich, AFGL/PHG, who agreed that this was not unreasonable, as the potential bias on the SSIE sensor on F7 and had been increased to its maximum positive value after the March 1984 failure of the ion RPA sensor.

Table 12. Results of the SSIE effective F10 analyses.

<u>Data Set</u>	<u>Adjustment Factor</u>	<u>$f_p(840)$</u>	<u>EF10</u>
POLY1 TEC	-	1.516	94.71
SSIE	1.0	2.910	170.61
SSIE	3.0	1.680	100.02
SSIE	π	1.642	97.78
SSIE	3.3	1.602	95.63
SSIE	3.4	1.578	94.33
SSIE	3.5	1.555	93.08

A limited amount of electron sweep data, which more reliably represent an absolute measure of $N_e(840)$ in the current sensor status, for 8 September were compared against the electron probe data for the same period. A total of 43 good electron sweep observations were found during the period examined. The ratio of the density from the electron probe to that obtained from the electron sweeps ranged from 1.5 to 5.0 with orbit-averaged values of 2.7-3.2. This agrees well with the results of the EF10 analysis.

5. 4D MODEL IMPROVEMENTS STUDY

The two tasks which make up this study, Tasks 1 and 3, were both completed during the first year of this project. The results were presented in detail in Scientific Report No. 1 of this contract⁹ - only a short summary will be presented here.

5.1 Task 1: 4D Model Global Analysis

The objective of this task was to review the AWS 4D model program to determine what modifications were required to configure the 4D model for a two-hemisphere analysis. The required changes were identified and were implemented in the AFGWC 4D mode code and documented as part of a separate contract⁷.

5.2 Task 3: Model-based 4D Height Functions

The objective of this task was to generate a set of height functions for the 4D model using a collection of electron density profiles generated from the IRI79 model. As it was decided not to use IRI79 within the 4D model (see Section 3.1), three sets of height functions were generated using profile sets constructed from the DHR model. All software required to generate the model-based height profiles and the associated documentation was provided to AFGWC.

6. PROJECT SUMMARY

Over the two years of this contract, a series of investigations were conducted of ways to expand and improve the use of *in situ* observations of the ionosphere from the DMSP SSIE sensor by the Air Weather Service (AWS) 4D ionospheric analysis model. The 4D analysis model was modified to allow it to be configured for a true global analysis, and several sets of 4D height functions were generated from a model ionosphere data base. In the two primary investigations, a new parametrization of the topside electron density profile and a technique for generating northern hemisphere grids of electron density from observations along an orbit track were developed.

The topside profile model developed is capable of constructing a topside electron density profile using the full set of data available from the SSIE sensor ($N(O^+)$, $N(H^+)$, T_i , and T_e) in conjunction with ground-based observations of f_oF2 , h_mF2 , and TEC. An empirical model of the height of the transition from O^+ -dominance to H^+ -dominance, i.e., the height at which $N(O^+) = N(H^+)$, was developed for use by the profile model should data from the SSIE sensor be unavailable.

The methods developed for generating electron density grids from orbit data, based on methods used by the 4D analysis model, were implemented in a computer program, GRIDNE, and tested extensively against observations generated from a model ionosphere. The results of the testing showed that the method reproduces the input data very well, but that the accuracy of the field more than 30° away from a data point is almost solely a function of how well the internal model of the electron density at 840km, $N_e(840)$, represents the shape of the diurnal and spatial variations of the ionosphere. The analysis methods developed are totally independent of the $N_e(840)$ model used, so as improved models are developed they can be used to upgrade the internal $N_e(840)$ model. Two internal models of $N_e(840)$ were developed for use by program GRIDNE, one based on the Bent¹² ionosphere model and one based on the AWS Damon-Hartranft-Ramsay (DHR)¹¹ ionosphere model. The two models produce quite different $N_e(840)$ fields for a given sunspot number, but without a systematic comparison of the two to observations it is impossible to select, *a priori*, the best of the two.

The use of this analysis model for generating joint analyses of SSIE and TEC data was also investigated in a limited fashion. In these tests, the TEC data were assumed to have been converted to an equivalent $N_e(840)$, using a profile model, and then these $N_e(840)$ data were included in analyses of simulated DMSP orbit data. The tests showed that this is a feasible method for combining the two data types into a single analysis.

REFERENCES

1. Secan, J.A., DMSP SSIE Topside Data Interface System, System Documentation, Report No. PD-NW-82-275R, Physical Dynamics, Inc., Bellevue, WA 98009, September 1982.
2. Smiddy, M., Sagalyn, R.C., Sullivan, W.P., Wildman, P.J.L., Anderson, P., and Rich, F., The Topside Ionosphere Plasma Monitor (SSIE) for the Block 5D/Flight 2 Satellite, AFGL-TR-78-0071, ADA058503, Air Force Geophysics Laboratory, Hanscom AFB, MA 01731, March 1978.
3. Rich, F., Smiddy, M., Sagalyn, R.C., Burke, W.J., Anderson, P., Bredesen, S., and Sullivan, W.P., In-Flight Characteristics of the Topside Ionospheric Monitor (SSIE) on the DMSP Satellite Flight 2 and Flight 4, AFGL-TR-80-0152, ADA088879, Air Force Geophysics Laboratory, Hanscom AFB, MA 01731, April 1980.
4. Air Force Global Weather Central Data Format Handbook, Air Force Global Weather Central, Offutt AFB, NE 68113, September 1983 (available through Hq Air Weather Service/DNTS, Scott AFB, IL 62225).
5. Siong-Huat, C., DMSP SSIE Uniform Grid Generator (Program SSIELD), System Documentation, Bedford Research Associates, Bedford, MA 01730, June 1983.
6. Secan, J.A. and Tascione, T.F., "The 4D Ionospheric Objective Analysis Model," in Proceedings of the 1984 Symposium on the Effect of the Ionosphere on C3I Systems, 1984.
7. Secan, J.A., 4D Ionospheric Analysis Model, System Documentation, Report No. PD-NW-83-297R-1, Physical Dynamics, Inc., Bellevue, WA 98009, December 1983.
8. Lincoln, J.V. and Conkright, R.O., International Reference Ionosphere-IRI79, Report UAG-82, World Data Center for Solar-Terrestrial Physics, Boulder, CO 80303, November 1981.
9. Secan, J.A., Development of Techniques for the Use of DMSP SSIE Data in the AWS 4D Model, AFGL-TR-84-0167, Air Force Geophysics Laboratory, Hanscom AFB, MA 01731, July 1984.
10. Damon, T.D. and Hartranft, F.R., Ionospheric Electron Density Profile Model, Technical Memorandum 70-3, Aerospace Environmental Support Center, Ent AFB, CO, July 1970 (available from the USAF Air Weather Service Technical Library, Scott AFB, IL 62225).

11. Flattery, T.W. and Ramsay, A.C., "Derivation of Total Electron Content for Real Time Applications," Effect of the Ionosphere on Space Systems and Communications, Naval Research Laboratory, Washington, DC, pp. 336-344, 1975.
12. Llewellyn, S.K. and Bent, R., Documentation and Description of BENT Ionospheric Model, AFCRL-TR-73-0657, AD772733, Air Force Geophysics Laboratory, Hanscom AFB, MA, 1973.
13. Titheridge, J.E., "Ion Transition Heights from Topside Electron Density Profiles," Planet. Space Sci., 24, pp. 229-245, 1976.
14. Bauer, S.J., Physics of Planetary Ionospheres, Springer-Verlag Publishing Co., New York, NY, 1973.
15. Bilitza, D., "The Atmospheric Explorer C Ionospheric Temperatures: Dependences and Representation," Report UAG-90, World Data Center for Solar-Terrestrial Physics, Boulder, CO, pp. II4-122, May 1984.
16. Lockwood, M., and J.E. Titheridge, "Departures from Diffusive Equilibrium in the Topside F-layer from Satellite Soundings," J. Atmos. Terr. Phys., 44, pp. 425-440, 1982.
17. Kutiev, I., Heelis, R.A., and Sanatani, S., "The Behavior of the $O^+ - H^+$ Transition Level at Solar Maximum," J. Geophys. Res., 85, pp. 2366-2372, May 1980.
18. Kutiev, I., K. Serafimov, M. Karadimov, and R.A. Heelis, "A Proposed Improvement of IRI-79 using the $O^+ - H^+$ Transition Level," Report UAG-90, World Data Center for Solar-Terrestrial Physics, Boulder, CO, pp. 150-154, May 1984.
19. Titheridge, J.E., "Plasmapause Effects in the Top Side Ionosphere," J. Geophys. Res., 81, pp. 3227-3233, July 1976.
20. Moffett, R.J. and S. Quegan, "The Mid-Latitude Trough in the Electron Concentration of the Ionospheric F-Layer: A Review of Observations and Modeling," J. Atmos. Terr. Phys., 45, pp. 315-343, May 1983.
21. Tascione, T.F., Flattery, T.W., Patterson, V.G., Secan, J.A., and Taylor, J.W., "Ionospheric Modeling at Air Force Global Weather Central," Solar-Terrestrial Predictions Proceedings, Volume I, Space Environment Laboratory, Boulder, CO, pp. 367-377, August 1979.
22. Thompson, R.L. and Secan, J.A., "Geophysical Forecasting at AFGWC," Solar-Terrestrial Predictions Proceedings, Volume I, Space Environment Laboratory, Boulder, CO, pp. 350-366, August 1979.
23. Automated Data Systems (ADS) Documentation, Department of Defense Standard 7935, February 1983.

24. AFGWC Software Standards, Air Force Global Weather Central, Offutt AFB, NE, March 1983 (available through Hq Air Weather Service/DNTS, Scott AFB, IL 62225).
25. Jones, W.B., Graham, R.P., and Leftin, M., Advances in Ionospheric Mapping by Numerical Methods, ESSA Technical Report ERL 107 - ITS 75, Institute for Telecommunication Sciences, Boulder, CO, May 1969.
26. Jones, W.B. and Obitts, D.L., Global Representation of Annual and Solar Cycle Variation of foF2 Monthly Median 1954-1958, OT/ITS Research Report 3, Institute for Telecommunication Sciences, Boulder, CO, October 1970.
27. von Flotow, C.S., "Ionospheric Forecasting at Air Force Global Weather Central," Effect of the Ionosphere on Space and Terrestrial Systems, Naval Research Laboratory, Washington, DC, pp. 385-392, 1978.
28. Flattery, T.W., "Spectral Models for Global Analysis and Forecasting," Automated Weather Support, AWS-TR-242, Air Weather Service, Scott AFB, IL, pp. 42-54, April 1971 (available from the USAF Air Weather Service Technical Library, Scott AFB, IL 62225).

Appendix A. Topside EDP Parametrizations

A.1 Modified DHR Model

a. Description. This model uses a Chapman layer with a height-varying scale height to describe $N_e(h)$ between $h_m F2$ and h_T , an exponential layer with an exponentially varying scale height above h_T , and a spline fit between the two layers from $h_T - 50$ km to $h_T + 50$ km.

b. Functional Form.

$$1) \quad h_m F2 < h \leq h_T - 50$$

$$N_e(h) = N_{e1}(h) = N_m F2 \exp [1 - z - e^{-z}]$$

$$z = \frac{h - h_m F2}{H_1(h)}$$

$$H_1(h) = H_0(\phi_m, LT) \ln \left| \frac{h}{85.4} \right|$$

$H_0(\phi_m, LT)$: empirical DHR scale height factor¹¹

ϕ_m : magnetic latitude

LT : local solar time.

$$2) \quad h_T - 50 < h < h_T + 50$$

$$N_e(h) = a_0 + a_1 \Delta h + a_2 \Delta h^2 + a_3 \Delta h^3$$

$$\Delta h = h - h_T$$

$$a_0 = \bar{N} - 25\bar{N}'$$

$$a_1 = 0.03 (N_+ - \bar{N}) - 0.5 (N_T' - \bar{N}')$$

$$a_2 = 0.01 \bar{N}'$$

$$a_3 = 0.0002 [(N'_+ - \bar{N}') - 0.02 (N_+ - \bar{N})]$$

$$\bar{N} = 0.5 (N_- + N_+)$$

$$\bar{N}' = 0.5 \left[\frac{\partial N_-}{\partial h} + \frac{\partial N_+}{\partial h} \right]$$

$$N_- = N_{e1} (h_T - 50)$$

$$N_+ = N_{e2} (h_T + 50) .$$

3) $h_T + 50 < h \leq 2000$

$$N_e(h) = N_{e2}(h) = N_T e^{-z}$$

$$N_T = N_{e1}(h_T)$$

$$z = \frac{h - h_T}{H_2(h)}$$

$$H_2(h) = H_T \exp\left(\frac{h - h_T}{\beta}\right)$$

$$H_T = H_1(h_T)$$

β : Adjustable free parameter.

A.2 Modified Bent Model

a. Description. In this modification of the Bent model¹², three exponential layers are used to model $N_e(h)$ from a height h_1 , $h_1 > h_m F2$, and a parabolic layer is used to model $N_e(h)$ from $h_m F2$ to h_1 . The parabolic layer and the parabolic semi-thickness, y_t , are identical to the Bent model, and the scale heights used in the exponential layers are calculated from the Bent k-parameters.

b. Functional form.

1) $h_m F_2 \leq h \leq h_1$

$$N_e(h) = N_p(h) = N_m F_2 \left[1 - \left(\frac{h - h_m F_2}{y_t} \right)^2 \right]$$

y_t : Bent model semi-thickness

$$h_1 = h_m F_2 + \frac{1}{k_1} \left| \sqrt{1 + y_t^2 k_1^2} - 1 \right|$$

k_1 : Bent decay factor for bottom exponential layer.

2) $h_1 < h \leq h_T$

$$N_e(h) = N_1 e^{-\left[\frac{h - h_1}{H_1(h)} \right]}$$

$$N_1 = N_m F_2 \left[1 - \left(\frac{h_1 - h_m F_2}{y_t} \right)^2 \right]$$

$$H_1(h) = H_0 + a \ln \left| \frac{h}{h_1} \right|$$

$$H_0 = \frac{1}{K_1}$$

$$a = \frac{H_T - H_0}{\ln \left| \frac{h_T}{h_1} \right|}$$

$$H_T = \frac{h_T - h_1}{N_1 \ln \frac{h_T}{h_1}}$$

N_T : Density at h_T from Bent model.

$$3) \quad h_T < h < 2000$$

$$N_e(h) = N_T \cdot e^{-\left| \frac{h-h_T}{H_2} \right|}$$

$$H_2 = \frac{1}{k_5}$$

k_5 : Bent decay factor for the top exponential layer.

A.3 Titheridge H(h) Model

a. Description. Titheridge¹³ developed a parametrized model for the variation of the plasma scale height with height based on a diffusive equilibrium model of the topside ionosphere. This is used to define the variation of $N_e(h)$ above a height $h_1 > h_m F2$. The Bent model parabolic layer is used to model $N_e(h)$ from $h_m F2$ to h_1 .

b. Functional form.

$$1) \quad h_m F2 < h < h_1$$

$$N_e(h) = N_m F2 \left[1 - \left(\frac{h-h_m F2}{y_t} \right)^2 \right]$$

y_t : Bent model semi-thickness

$$h_1 = \frac{1}{2} y_t .$$

$$2) \quad h_1 < h < 2000$$

$$N_e(h) = N_1 \exp \left[-\int_{h_0}^h \frac{dh}{H(h)} \right]^*$$

$$N_1 = N_m F2 \left[1 - \left(\frac{h_1-h_m F2}{y_t} \right)^2 \right]$$

*This integration is carried out numerically using a 10-point Gaussian quadrature algorithm.

$$H(h) = H_A \exp \left(\frac{VD}{\sqrt{V + D^2}} \right)$$

$$D = \frac{h - h_A}{H_A}$$

$$U = \ln \left| \frac{H_1}{H_A} \right| \left(\frac{\sqrt{V + D_1^2}}{D_1} \right)$$

$$H_1 = \frac{1}{Z} \left[\frac{y_t^2 - (h_1 - h_m F_2)^2}{h_1 - h_m F_2^2} \right]$$

$$D_1 = \frac{h_1 - h_A}{H_A}$$

H_A, h_A, V : Model parameters from a table¹³ based on h_T and the temperature profile from 400 km to h_T .